Advances in Baffled and Railed Tube Ram Accelerator Operation and Modeling

Brian J. Leege

A dissertation

submitted in partial fulfillment of the

requirements for the degree of

Doctor of Philosophy

University of Washington

2022

Reading Committee:

Carl Knowlen, Chair

Adam Bruckner

Owen Williams

Program Authorized to Offer Degree:

Aeronautics and Astronautics

University of Washington

Abstract

Advances in Baffled and Railed Tube Ram Accelerator Operation and Modeling

Brian J. Leege

Chair of the Supervisory Committee:

Carl Knowlen

Department of Aeronautics and Astronautics

The ram accelerator is a novel chemical propulsion device capable of accelerating projectiles up to orbital velocities. It utilizes a ramjet-like propulsive cycle, where a projectile travels through a stationary tube filled with a gaseous propellant, experiencing high levels of thrust throughout the tube. The projectile carries no onboard propellant and has no moving parts. This makes the ram accelerator a relatively simple, more efficient, and high-performance alternative to guns and rockets for a first stage launch system. While originally developed to utilize finned-projectiles in a smooth bored tube, additional ram accelerator configurations have been developed to accommodate axisymmetric projectiles in baffled and railed tubes (the BTRA and RTRA). These newer configurations allow for a more practical implementation of ram accelerator technology in numerous applications and have been found to expand the capabilities of ram accelerator systems. This dissertation includes a comprehensive experimental study of the BTRA, RTRA, and two newly invented ram accelerator configurations, as well as the development of a new computational model for BTRA and RTRA operation.

The experimental effort focused on the testing of newly developed BTRA and RTRA hardware, a survey of viable BTRA propellants, and the development of two new ram accelerator configurations: the RTRA with sweeper baffles and the baffled start stage (BSS). The BTRA testing discovered that

smaller diameter baffle chambers are capable of producing higher thrust with higher efficiency, while larger diameter baffle chambers allow for operation at lower Mach numbers. The BTRA has now been demonstrated to operate at as low as Mach 1.85. The RTRA was found to achieve significantly higher thrust and efficiency than the BTRA, while requiring higher Mach numbers for operation. The new RTRA with sweeper baffles concept was shown to be a viable ram configuration for improving the performance and expanding the operational envelope of an RTRA. The newly developed BSS was shown to be a good technology for producing ram starts without the typical use of an obturator.

The new computational model, called the ram accelerator plug flow reactor (PFR) model, proved to be a significant advancement in the modeling of ram accelerator operation. The ram PFR model is a quasi-1D model that resolves the entire ram flowpath. It includes a model for the effects of baffles on the ram flowfield, accommodates real projectile geometries as used in experiments, and includes corrections for the non-inertial projectile reference frame. The new ram PFR model is able to predict the operational envelopes of the BTRA with remarkable accuracy and will now serve as a valuable tool in the development of future ram accelerator configurations.

Acknowledgments

First, I would like to thank Dr. Carl Knowlen, for introducing me to the ram accelerator and allowing me to lead the research efforts in his lab for so many years. He was an excellent mentor and his extensive knowledge on 'all things ram' was constantly helpful. I will always appreciate his many stories recounting the ram days of old, no matter how many times he tells them.

I would also like to thank all my colleagues who have worked with me in the ram lab (or adjacent labs) over the years: Chase Smith, Ty Mundt, Navid Daneshvaran, John Correy, James Koch, and Finn van Donkelaar. The countless hours spent in the lab and moral support you all provided made many of the harder days much easier. Your contributions to this work are greatly appreciated!

Thank you to all of the undergraduate students who helped run the experiments over the years. You are far too many to name here, but your contributions were significant and your great attitudes and work ethic were very much appreciated.

I would also like to thank HyperSciences, Inc. for funding and supporting this work. I also declare a competing financial interest in HyperSciences, Inc., which has licensed the described technology from the University of Washington in concert with EnergeticX, LLC.

Finally, I would like to thank my family and friends for supporting me throughout this journey. It certainly wasn't easy, and perhaps took longer than it should, but I would not have made it to the finish line without your support.

Contents

List of Figures

List of Tables

Nomenclature

Variables

Δq	heat of reaction, J/kg
Δz	control volume length, m
$\dot{m}$	mass flow rate, kg/s
$\dot{Q}$	heat power, W
$\dot{W}$	Work power, W
$\dot{W}_I$	inertial power, W
$\dot{W}_w$	power input from baffle wall, W
$\dot{W}_{BL}$	projectile base power loss, W
$\overline{n}$	unit normal vector
$\overline{v}$	velocity vector, m/s
A	area, m^2
a	sound speed, m/s
A^*_{CV}	effective area of control volume, m^2

A_b bore area, m^2

a_p projectile acceleration, m/s^2

A_w baffle wall area, m^2

A_{cyl} area of cylindrical control volume, m^2

A_{eff} effective smooth bore area of BTRA, m^2

c_d baffle drag coefficient

C_I inertial force coefficient

c_p specific heat at constant pressure, J/kg-K

D baffle drag force, N

d diameter, m

d_{eff} effective smooth bore diameter of BTRA, m

e specific internal energy, J/kg

F ram accelerator thrust, N

F_I inertial force on control volume, N

F_p force of projectile on control volume, N

F_w force of baffle on control volume, N

h enthalpy, J/kg

h_f enthalpy of formation, J/kg

I non-dimensional thrust

L length, m

M Mach number

MW molecular weight, kg/kmol

N number of species in chemical kinetics model

p pressure, Pa

Q non-dimensional heat release

R specific gas constant, J/kg-K

R_u universal gas constant, J/mol-K

T temperature, K

t time, s

u velocity, m/s

u_p projectile velocity, m/s

V volume, m^3

V_f volume of fluid, m^3

V_{rail} volume of rails, m^3

W_{BL} projectile base energy loss, J

Y mass fraction

z axial coordinate location, m

β volume void ratio

$\dot{\omega}$ species mass production rate, kg/m^3-s

γ ratio of specific heats

ϕ equivalence ratio

ρ density, kg/m^3

Subscripts

1, 2 state indices

a aftward facing baffle wall

avg average

b baffle

BTRA baffled tube ram accelerator

c chamber

CJ Chapman-Jouguet detonation condition

CS control surface

CV control volume

f forward facing baffle wall

i index

lab lab (stationary) frame of reference

mix gas mixture

RTRA railed tube ram accelerator

TC thermally choked

TCP thermally choked plane

TCRA thermally choked ram accelerator

Abbreviations

1D one-dimensional

BE ballistic efficiency

BKW Becker-Kistiakowsky-Wilson (equation of state)

BSS baffled start stage

BTRA baffled tube ram accelerator

CAD computer aided design

CFD computational fluid dynamics

CJ Chapman-Jouguet

CRN chemical reactor network

CV control volume

EM electromagnetic

EOS equation of state

ODE ordinary differential equation

PFR plug flow reactor

RTRA railed tube ram accelerator

SBRA smooth bore ram accelerator

TCP thermally choked plane

TCRA thermally choked ram accelerator

Chapter 1

Introduction and Background

The ram accelerator was first introduced by University of Washington researchers in the 1980s as a novel chemical propulsion device for accelerating projectiles to very high velocities [1, 2]. Utilizing a ramjet-like propulsive cycle, the ram accelerator is capable of accelerating projectiles more efficiently than a gun, with a more uniform and controllable acceleration profile. Unlike rockets, however, ram projectiles carry no onboard propellant. Thus, the ram accelerator is a compelling alternative to both guns and rockets for hypervelocity applications. While originally designed for space launch applications [3–5], the ram accelerator has also been considered for aeroballistic testing [6, 7], and more recently for drilling and boring applications [8].

1.1 Ram Accelerator Concept

At its heart, the ram accelerator is a very simple chemical propulsion engine. This engine consists of a stationary tube that is filled with a gaseous propellant mixture and a projectile that travels within. When the projectile travels through the gaseous propellant at supersonic speeds, a ramjet-like flowfield is established, providing near constant thrust throughout the tube. For reference, a schematic of the ramjet engine flowfield is shown in Fig. 1.1. In the ramjet analogy, the ram projectile acts as the ramjet engine centerbody and the tube as the engine cowling. In this configuration, the ram projectile does not carry any onboard

propellant and aside from the projectile itself, the ram accelerator has no moving parts. This offers a significant advantage over traditional gun technologies without the staggering complexity of modern rocket engines.

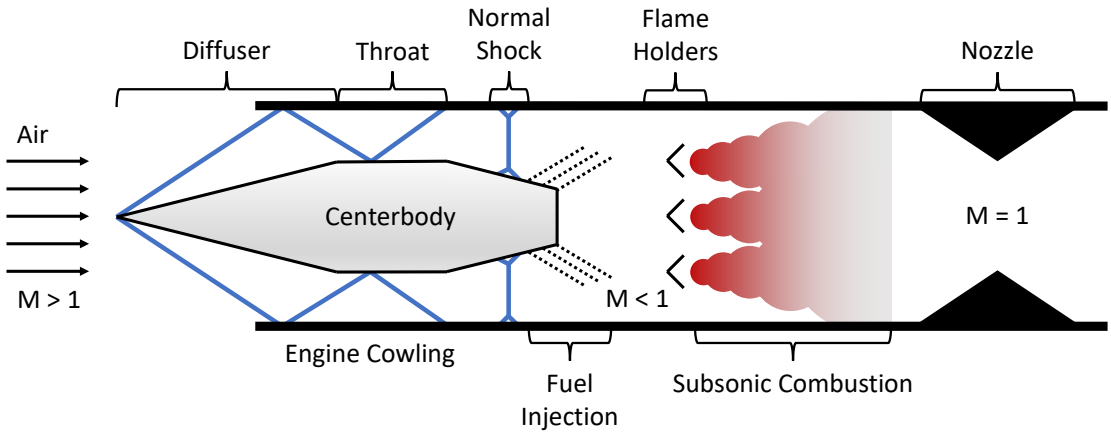

Fig. 1.1 Flowfield schematic of the ramjet engine.

The ram accelerator has two primary operating modes. At projectile velocities below the Chapman-Jouguet (CJ) detonation speed of the propellant, the ram accelerator utilizes subsonic combustion similar to the ramjet engine. At projectile velocities greater than the CJ detonation speed of the propellant, the ram accelerator utilizes supersonic combustion similar to a scramjet engine. These are typically referred to as the subdetonative and superdetonative ram accelerator modes, respectively, and are detailed in the following sections.

The net result of any ram accelerator operating mode is the establishment and stabilization of a high pressure combustion region on the projectile body, providing high thrust throughout the tube. Additionally, the thrust is directly proportional to the propellant fill pressure. This means that for a given projectile design, the ram accelerator propellants and fill pressures can be tailored to provide the exact acceleration profile desired for the projectile. This could include high-g applications (10,000+ g) for g-resistant payloads, mid-g applications (~1000 g) for g-hardened electromechanical payloads, or low-g applications (1–10 g) for sensitive electronics or biological (i.e., human) payloads. In principle, the higher the acceleration, the shorter the tube length required for a given muzzle velocity. This pressure scaling capability makes the ram accelerator extremely versatile and operable at nearly any size scale.

1.2 Ram Accelerator Operating Modes

1.2.1 Subdetonative Ram Accelerator

The subdetonative ram accelerator operates with subsonic combustion at projectile velocities lower than the CJ detonation speed [1]. In this ram mode, the gaseous propellant is compressed in the supersonic diffuser where it interacts with the bow shock of the projectile. The compressed propellant continues to travel supersonically through the constant area throat section where it is further processed by the bow shock reflections between the tube wall and the projectile. The flow then accelerates through the area expansion of the tail cone until it is affected by a shock-train system that is functionally equivalent to a normal shock. This further compresses the propellant and reduces it to subsonic speeds. It is in this high pressure and temperature region that combustion is initiated.

In order to stabilize the normal shock on the projectile and keep the high pressure combustion region communicating with the projectile, choking must occur within the combustion region. In theory, this choking could be done either mechanically (with a second projectile throat) or thermally. In practice, thermal choking is far simpler to achieve and is the primary operating mode of the subdetonative ram accelerator. In this mode, heat is continually added by combustion until thermal choking occurs, according to the principles of Rayleigh flow [9]. Any phenomena downstream of the thermal choking point is un-

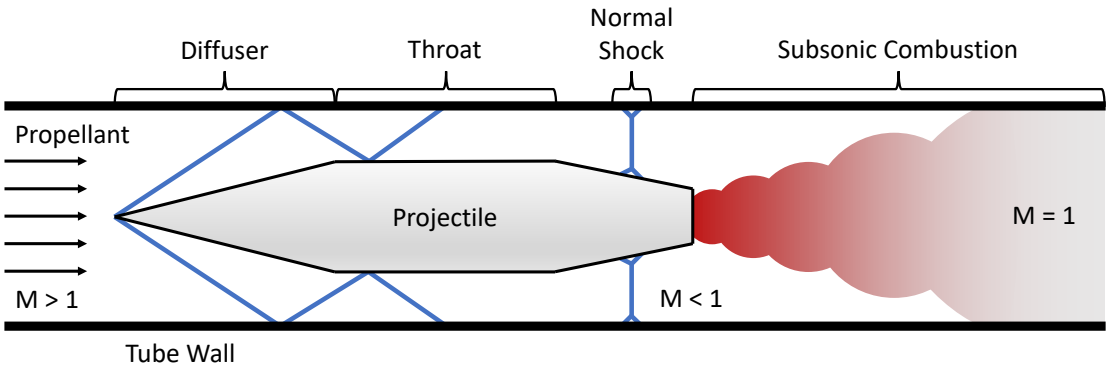

Fig. 1.2 Flowfield schematic of the TCRA.

able to communicate with the projectile. In effect, this stabilizes the combustion region on the projectile body, allowing it to continue accelerating down the tube while being isolated from downstream effects. This operating mode is called the thermally choked ram accelerator (TCRA) and is depicted in Fig. 1.2.

The TCRA is perhaps the most well-studied and understood ram accelerator operating mode. However, due to its CJ detonation speed limit, the maximum TCRA velocities achievable (using hydrogen based propellants) are in the range of 2700–3000 m/s [1]. To operate at higher velocities, or reach these velocities with other propellants, the ram accelerator must transition to its superdetonative operating mode.

1.2.2 Superdetonative Ram Accelerator

The superdetonative ram accelerator operates with supersonic combustion at projectile velocities greater than the CJ detonation speed [1]. Shown in Fig. 1.3, the superdetonative ram accelerator features purely supersonic flow and combustion, similar to a scramjet. In this mode, the propellant is compressed in the inlet diffuser, just as in the TCRA. However, due to the relatively high Mach number, the compression of the bow shock reflection off the projectile shoulder raises the temperature and pressure of the flow high enough to ignite the propellant. The combustion process completes within the constant area throat section of the projectile and the products are then accelerated through the area expansion on the tail cone.

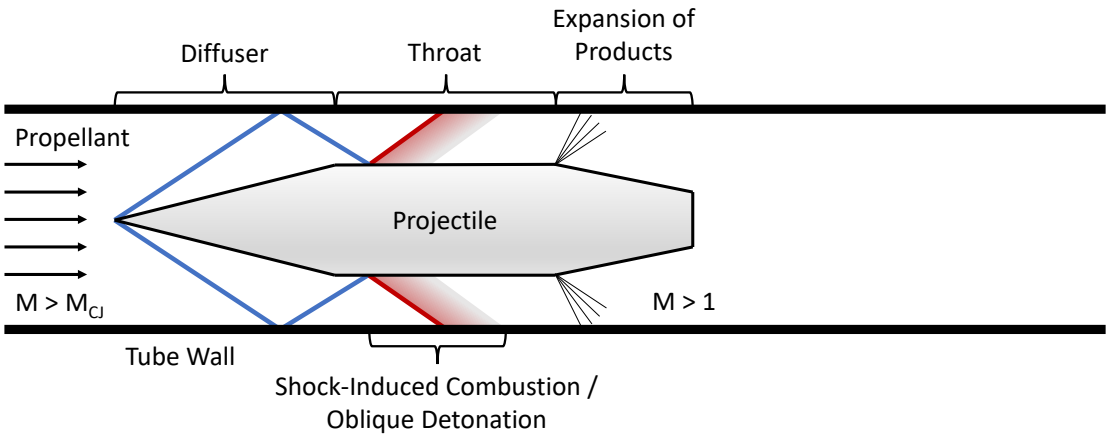

Fig. 1.3 Flowfield schematic of the superdetonative ram accelerator.

This results in a propulsive mode that is more capable of producing thrust at higher velocities than the TCRA.

The exact combustion mechanism in the superdetonative ram accelerator mode is not entirely clear. The combustion may occur in an oblique detonation wave or via shock-induced combustion that is decoupled from the initial shock wave. Oblique detonations feature a relatively rapid, short combustion region, having the advantage of shorter projectile length requirements and less viscous losses. However, that is countered by the fact that a series of weaker oblique shocks can produce ignition conditions with lower losses than a single, stronger shock. This second scenario is closer to the shock-induced combustion mechanism in which combustion occurs decoupled from the initial reflected shock wave on the projectile. In this mode, combustion occurs much further down the projectile and the combustion zone is generally longer. Currently, it is unclear which combustion mode is preferred, but it may not even be possible to control which mode occurs. Superdetonative ram combustion may even include both of these mechanisms. These combustion mechanisms are discussed in further detail by Higgins [10].

1.2.3 Transdetonative Ram Accelerator

Through experimentation with the subdetonative and superdetonative ram accelerators, a smooth transition between each operating mode was discovered and dubbed the transdetonative ram mode [2]. In these experiments, it was found that within a ram stage that is filled with a single propellant mixture, a projectile could transition from the TCRA mode to the superdetonative mode with continuous operation. Shortly before it reaches the CJ speed, the projectile would experience a rapid increase in acceleration and achieve velocities well above the CJ speed, taking advantage of the superdetonative mode. It is assumed that in this transdetonative mode, the Mach number is sufficient that the reflected bow shock wave can partially ignite the propellant well ahead of the normal shock, achieving a mixed combustion mode combining the superdetonative combustion mechanisms with the subdetonative (i.e., subsonic) combustion mechanism. This allows the projectile to go beyond the limits of TCRA operation and eventually transition to the pure superdetonative mode.

The existence of the transdetonative mode is convenient in that it reduces the required complexity of achieving high velocity ram accelerator operation by eliminating the staging requirements. However, for some applications it may be desirable to avoid the transdetonative mode entirely, due to its lower thrust compared to both the TCRA and superdetonative modes.

1.3 Ram Accelerator Theoretical Models

1.3.1 General Ram Accelerator Model

Ram accelerator performance can be theoretically derived using a 'black box' control volume method that is valid for all propulsive modes. This general ram accelerator model was discussed in detail by Knowlen and Bruckner [11] and remains the accepted ram accelerator theoretical model. In this approach, the projectile is considered to be quasi-steady and in a projectile-centered reference frame. In this frame, the projectile is stationary, with both the oncoming flow and tube walls moving aftward at the current projectile velocity. The flow is also considered to be inviscid. This sets up a channel flow in which a control volume can be imposed around the projectile as shown in Fig. 1.4. In this model, the projectile imposes a force on the control volume, denoted as F. While this is defined as the ram accelerator thrust, in truth, it is the net force on the projectile, including both thrust and drag components. The combustion in the

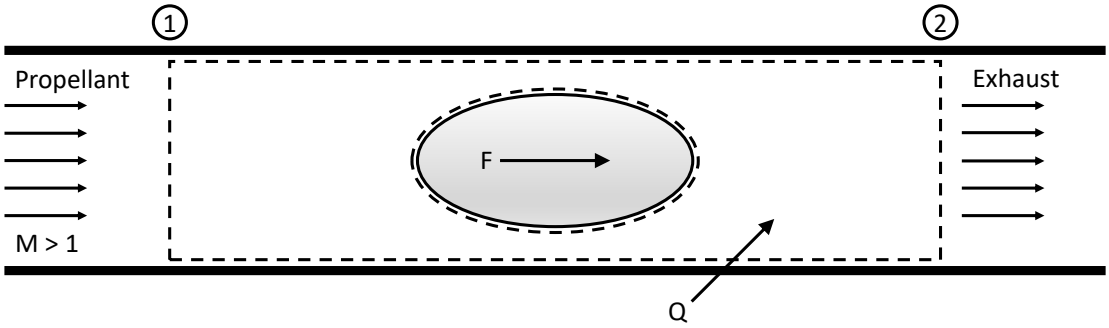

Fig. 1.4 Control volume for the general ram accelerator model.

flow is replaced by external heat addition, Δq. By only considering the flow states at the entrance and exit of the control volume, ram accelerator performance can be derived without considering the detail of the inner flowfield. This allows the model to be applied to all ram accelerator operating modes.

First, the conservation equations of mass, momentum, and energy are applied to the control volume in Fig. 1.4, yielding the following relations:

$$\rho_1 u_1 = \rho_2 u_2 \,, \tag{1.1}$$

$$\rho_1 u_1^2 + p_1 + \frac{F}{A} = \rho_2 u_2^2 + p_2 \,, \tag{1.2}$$

and

$$h_1 + \frac{u_1^2}{2} + \Delta q = h_2 + \frac{u_2^2}{2} \,. \tag{1.3}$$

It should be noted that the enthalpy (h) terms in Eq. (1.3) are sensible enthalpies while the enthalpies of formation are grouped in the Δq term ($\Delta q = h_{f1} - h_{f2}$). Applying the ideal-gas equation of state ($p = \rho R T$) and using the definitions of Mach number ($M = u/a$) and sound speed ($a = \sqrt{\gamma R T}$), Eqs. (1.1)-(1.3) can be re-written non-dimensionally as

$$\frac{p_2}{p_1} = \frac{M_1}{M_2}\sqrt{\frac{\gamma_1 R_2 T_2}{\gamma_2 R_1 T_1}} \,, \tag{1.4}$$

$$I \equiv \frac{F}{p_1 A} = \frac{p_2}{p_1}(1 + \gamma_2 M_2^2) - (1 + \gamma_1 M_1^2) \,, \tag{1.5}$$

and

$$\frac{h_1}{c_{p1} T_1} + \frac{\gamma_1 - 1}{2} M_1^2 + Q = \left(\frac{h_2}{c_{p2} T_2} + \frac{\gamma_2 - 1}{2} M_2^2\right)\left(\frac{c_{p2} T_2}{c_{p1} T_1}\right) . \tag{1.6}$$

Here, the non-dimensional thrust, I, is defined as the ram accelerator thrust normalized by the product of the tube fill pressure and cross-sectional area: $I \equiv F/(p_1 A)$. Additionally, the non-dimensional heat release parameter, Q, is defined by the heat of reaction normalized by the specific heat at constant pressure and the temperature of the unburned propellant: $Q \equiv \Delta q/(c_{p1} T_1)$. Finally, Eqs. (1.4)-(1.6) can be

combined to provide a single expression for the non-dimensional thrust for any ram accelerator system

$$I = \frac{\gamma_1 M_1}{\gamma_2 M_2}(1+\gamma_2 M_2^2)\sqrt{\left(\frac{\gamma_2-1}{\gamma_1-1}\right)\left(\frac{\frac{h_1}{c_{p1}T_1}+\frac{\gamma_1-1}{2}M_1^2+Q}{\frac{h_2}{c_{p2}T_2}+\frac{\gamma_2-1}{2}M_2^2}\right)}-(1+\gamma_1 M_1^2)\,. \tag{1.7}$$

The non-dimensional thrust equation for the ram accelerator, Eq. (1.7), can solve for thrust, given the flight Mach number, propellant heat release, and the gas properties at the inlet and exit planes. Typically, this equation is solved using an iterative method to converge on state "2" properties in conjunction with a chemical kinetics model and code. This method can provide accurate state "2" properties as well as calculate the actual heat release for a given propellant, leading to more accurate thrust calculations.

An important observation of this model is that projectile geometry does not show up at all. In fact, the only geometric consideration is the tube bore area used to convert the non-dimensional thrust into a dimensional quantity. This leads to the conclusion that the projectile geometry can be completely arbitrary, as long as it is one that allows the ram flowfield to be established. Therefore, this model does work for both thermally choked and superdetonative operation, and can even even handle more complicated cases such as the transdetonative mode or mechanical choking on the projectile.

1.3.2 Thermally Choked Ram Accelerator Model

The TCRA model is a simplification of the general ram accelerator model. In this case, M_2 in Eq. (1.7) is unity since state "2" is now the thermally choked plane, where flow is sonic with respect to the projectile. Therefore, the non-dimensional thrust of the TCRA is

$$I_{TCRA} = \frac{\gamma_1 M_1}{\gamma_2}(1+\gamma_2)\sqrt{\left(\frac{\gamma_2-1}{\gamma_1-1}\right)\left(\frac{\frac{h_1}{c_{p1}T_1}+\frac{\gamma_1-1}{2}M_1^2+Q}{\frac{h_2}{c_{p2}T_2}+\frac{\gamma_2-1}{2}}\right)}-(1+\gamma_1 M_1^2)\,. \tag{1.8}$$

This expression can be solved iteratively in conjunction with a chemical kinetics model, as discussed above. Figure 1.5 shows the non-dimensional thrust and heat release versus Mach number for two different ram propellants. In these calculations, the GRI-Mech 3.0 combustion mechanism was used in conjunction

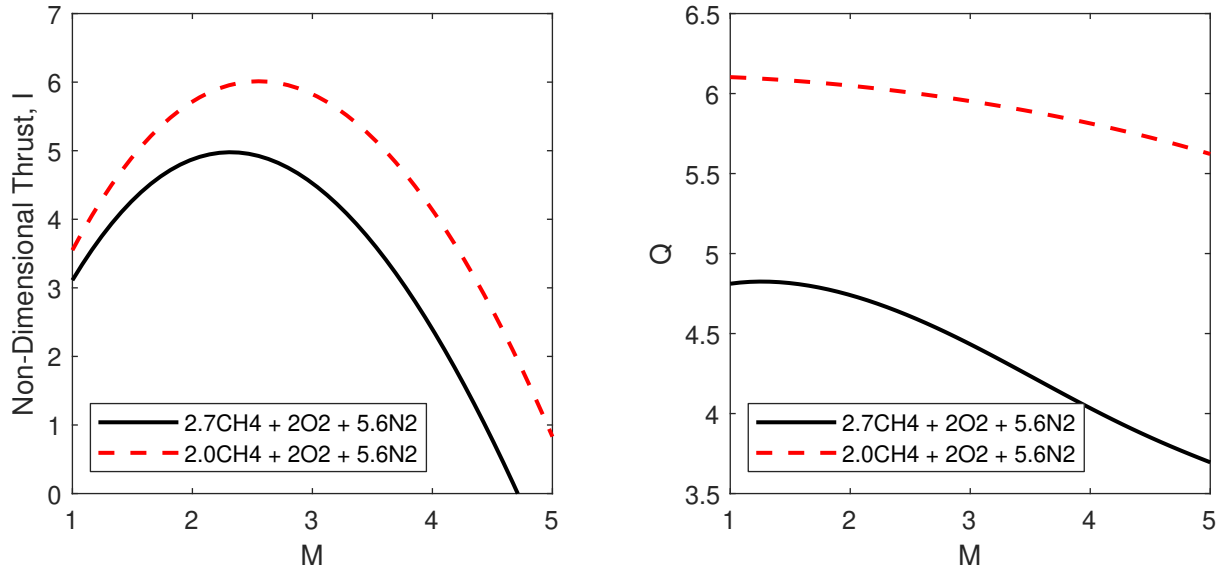

(a) **(b)**

Fig. 1.5 Non-dimensional thrust (a) and non-dimensional heat release (b) versus Mach number for two $CH_4/O_2/N_2$ propellants.

with Cantera to solve the equilibrium state at the thermally choked plane [12, 13]. The propellant with 2.7CH_4 is a typical propellant for TCRA operation and is representative of typical ram performance. A more energetic propellant, with 2.0CH_4, is shown for comparison. As can be seen, thrust increases with Mach number to a maximum, after which it decreases with increasing Mach number, ultimately reaching zero thrust. Of note, the zero thrust case is equivalent to the Chapman-Jouguet detonation model, as if the projectile were not present, and the corresponding Mach number is the CJ Mach number (M_{CJ}). For the 2.7CH_4 propellant shown in Fig. 1.5a, M_{CJ} is about 4.7. This represents the theoretical limit to TCRA operation, but not necessarily ram operation. As discussed above, the superdetonative and transdetonative operating modes will naturally take over when the projectile approaches M_{CJ}.

Another important insight from this model is that more energetic propellants (higher heat release) are capable of higher thrust and higher Mach number operation. This is highlighted by the 2.0CH_4 propellant, which is moderately more energetic than the 2.7CH_4 propellant. At all Mach numbers, the thrust is higher for the more energetic mixture. This result should be fairly intuitive in that a more energetic propellant has more energy to transmit to the projectile. It is also important to point out that the heat

release of a given propellant decreases as Mach number increases, shown in Fig. 1.5b. This is largely due to the dissociation losses that occur at the higher temperatures in the high Mach number flow.

This performance model has very good agreement with experiments. Figure 1.6 shows the velocity versus position comparison plots for TCRA theory and two experiments. These cases utilize similar propellants but feature different fill pressures and stage lengths. Even where the experiment outperforms theory towards the end of the six meter case, the velocity deviation from theory remains below 3%.

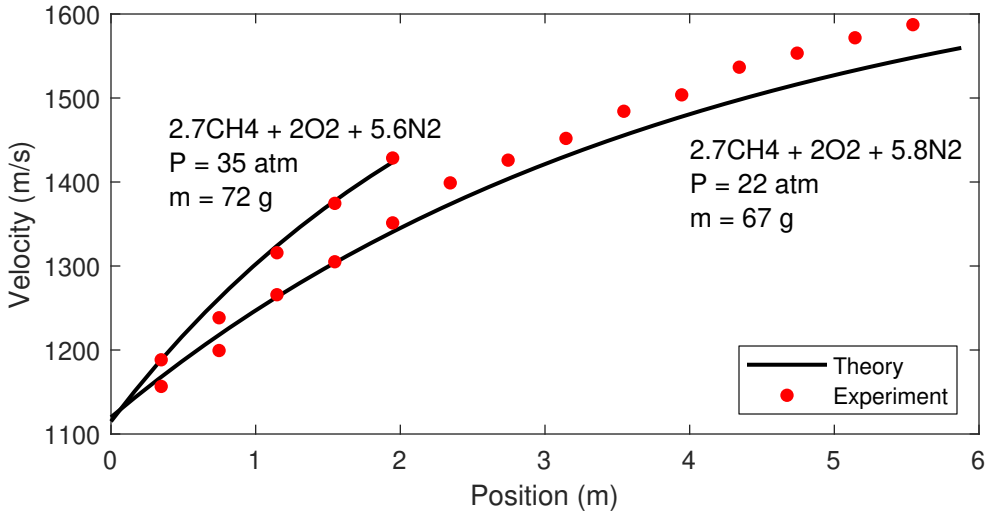

Fig. 1.6 Velocity versus position plots of TCRA theory and experiments for two cases with similar propellants but differing fill pressures and stage lengths [2].

1.3.3 Ram Accelerator Operational Limits

The TCRA and general ram models are able to accurately predict ram performance in most cases. However, since the model uses a 'black box' control volume approach, it is unable to elucidate the operational limits of the ram accelerator. To find these operational limits, a different approach is required and experimental validation is essential. These operating limits are discussed in detail in a pair of papers by Higgins et al. [14, 15], where the limits are first identified then characterized.

There are three fundamental limits, or boundaries, to ram operation and they are defined as a function of Mach number and heat release. These three limits create the operational envelope of the ram accelerator

and are shown graphically in Fig. 1.7. The first limit is a minimum operational Mach number that is required to prevent flow choking on the projectile nose cone. This is analogous to the unstarts that can occur in a ramjet engine or in a supersonic wind tunnel. There are typically two different limits to consider for this type of unstart: the Kantrowitz limit which defines the Mach number required to swallow the shock wave to first *start* the engine, and the isentropic limit which defines the Mach number at which the already swallowed normal shock reaches the throat, beyond which the engine *unstarts* [16, 17]. Ram accelerators are unique in that projectiles are accelerated to operating speeds before entering the ram accelerator, typically within a vacuum, so that they can enter already *started*. That is, they do not need to accommodate an accelerating flow and allow the shock to be swallowed, as in a ramjet engine or supersonic wind tunnel. Thus, the isentropic limit is the true theoretical minimum operating Mach number for the ram accelerator. This limit is labeled as "sonic at throat" in Fig. 1.7. That said, it is worth noting that ram accelerator starting is a very complex *transient* process [18], so the true minimum starting Mach number may, in reality, fall somewhere between the isentropic and Kantrowitz limits.

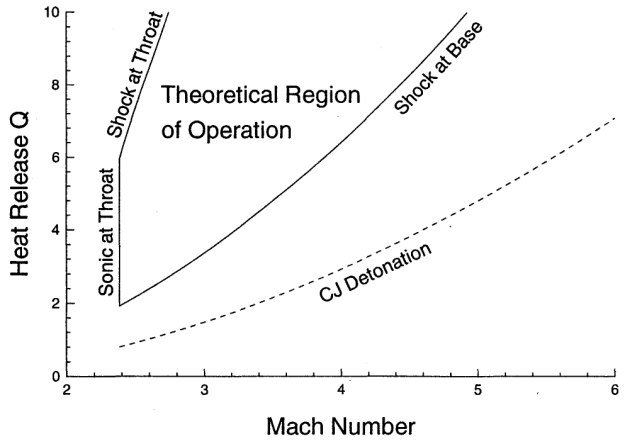

Fig. 1.7 Theoretical operational envelope of the ram accelerator [14].

The final two operational limits of the ram accelerator are a function of both propellant heat release and Mach number. First, there is a limit on the maximum heat release, at a given Mach number, at which the normal shock is disgorged from the projectile throat, driven by the highly energetic combustion process around the projectile. This leads to an immediate unstart, where the projectile rapidly decelerates. Second, there is a limit on the minimum heat release, at a given Mach number, at which the normal shock

and the combustion zone 'fall off' the projectile, leading to complete loss of thrust. In this scenario, the combustion is not energetic enough to keep up with the projectile and is typically referred to as wave falloff. Again, refer to Higgins et al. [14] for further details on how these theoretical limits are determined and calculated. Given these limits, it is clear that there will be a range of propellant heat releases that are operable for a given Mach number range. These limits are labeled in Fig. 1.7 as "shock at throat" and "shock at base," respectively.

It should be noted that while the above three operational limits are discussed and graphically depicted as a function of Mach number and heat release, they are also a function of the specific propellant gas properties and the tube and projectile geometries. While the shape of the operational envelope remains similar, the exact values and boundaries can shift with changes in geometric dimensions and gas properties.

While the above theoretical operational limits are useful conceptually, they have been remarkably poor predictors of the true ram accelerator operational envelope found in experiments [15]. This comparison is shown in Fig. 1.8. Boundary "a" is the heat release limit that results in an immediate unstart upon entrance to a ram stage. Boundary "b" represents a heat release limit that results in an unstart after at least 1 m of distance traveled. Boundary "c" represents unstarts that occur after at least 10 m of distance travelled and experienced transdetonative operation. Finally, boundary "d" represents the minimum

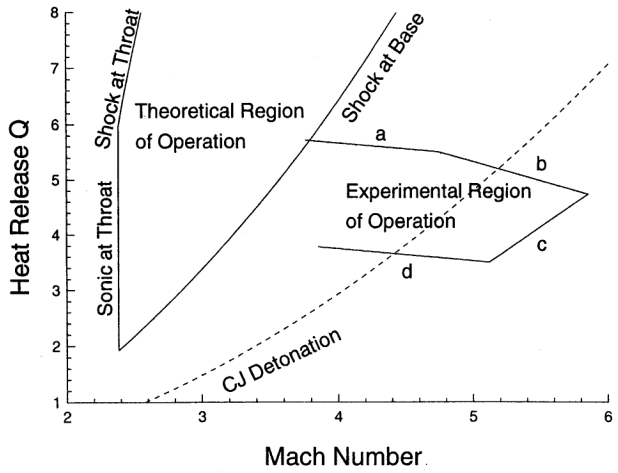

Fig. 1.8 Comparison of the theoretical and experimental operational envelopes of the ram accelerator [15].

heat release required for ram operation. Boundary "a" is most similar in concept to the "shock at throat," maximum heat release theoretical limit, in that it is a hard limit beyond which no ram operation is possible due to immediate unstarts. However, boundary "b" is a bit trickier. It shows that using propellants near the heat release limit can result in unstarts after a short period of acceleration. This indicates an opposite trend compared to the theory which predicts that allowable heat release should increase with Mach number (positive slope), where the experiments show that higher Mach numbers require lower heat releases (negative slope). This is likely a shortcoming of the many simplifying assumptions made in the theoretical model and highlights the complexity of the real ram accelerator flow field. The "c" boundary shows that by further decreasing the heat release of a mixture, ram acceleration can be sustained longer. That said, it is posited by Higgins et al. that the unstarts in these longer travel distance cases are most likely due to structural failure of the projectiles rather than a true limit to ram accelerator operation [15]. Boundary "d" also shows a similar downward trend as boundaries "a" and "b." This shows that a low heat release propellant can become operable simply by raising the Mach number. This is in opposition to the theoretical model, in a similar manner as boundaries "a" and "b" discussed above.

While the disconnect between the theoretical and experimental operating envelopes may be worrying, the main failure mechanisms that govern the operational boundaries hold true. That is, a minimum Mach number must be achieved to prevent an unstart due to inert gas dynamic effects, a minimum propellant heat release must be exceeded to sustain ram acceleration, and the propellant heat release must remain below a maximum at which unstarts will occur. It is likely that in order to accurately predict the operational envelope of a ram accelerator, high-fidelity computational fluid dynamics (CFD) simulations would be required.

1.4 Ram Accelerator Configurations

There are three primary hardware configurations for the ram accelerator. These include the original smooth bore ram accelerator (SBRA), the baffled tube ram accelerator (BTRA), and the railed tube

ram accelerator (RTRA). These ram accelerator hardware configurations are discussed in the following subsections.

1.4.1 Smooth Bore Ram Accelerator

The original ram accelerator concept was developed utilizing smooth bore tubes. In fact, all of the discussion above, as well as the data presented in Figs. 1.6 and 1.8, was for the SBRA. The SBRA has a few unique features that are required for operation. First, in order to stabilize the projectile in the tube center, fins were added to all ram projectiles in the SBRA. To allow reasonably low Mach number operation, governed by the isentropic and Kantrowitz limits discussed in section 1.3.3, the diameter of the projectile at the throat of the flow was set much smaller than the bore diameter. The fins added stability largely by maintaining close contact with the tube walls, minimizing projectile canting and balloting due to the sub-caliber size of its centerbody. A typical SBRA projectile is shown in Fig. 1.9.

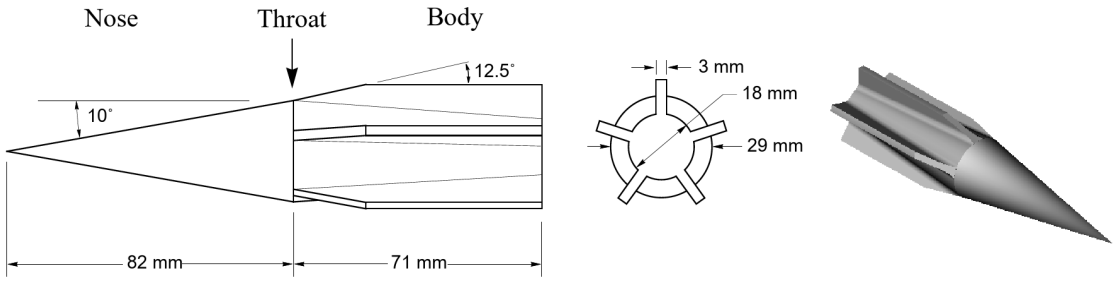

Fig. 1.9 Typical SBRA projectile [19].

Another important feature of the SBRA is the obturator. An obturator is a piston-like device that serves a dual-purpose in the ram accelerator. First, the obturator acts as a sabot for the sub-caliber projectile in the launch tube, helping to occlude the tube and preventing gas blow-by that could hinder or inhibit ram operation. Second, the obturator is a critical part in the ram accelerator starting process. The obturator acts as a piston, generating a high pressure and temperature region behind the projectile to facilitate combustion and exchange momentum with the gases so that the combusting gases may 'keep up' with the projectile, allowing the combustion zone to stabilize on the projectile once established. For the SBRA,

two types of obturators can be used: perforated or solid. These obturators are shown in Fig. 1.10. The perforated obturator is used with a backplate to occlude the launch tube while allowing some gas to flow through it in the ram stage. This still provides the piston-like effect needed for starting, while allowing for a wider range of starting conditions. The solid obturator is a simpler design with a single piece that still facilitates ram starts, though with a smaller range of operable conditions [18, 19].

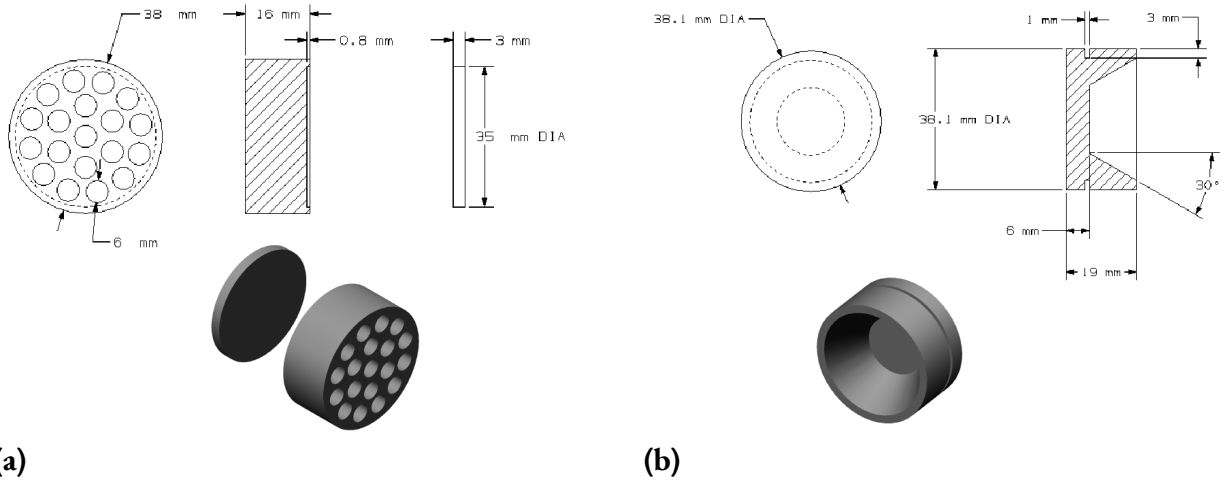

(a) **(b)**

Fig. 1.10 Typical perforated (a) and solid (b) polycarbonate obturators for the SBRA [19].

To date, the SBRA has been thoroughly explored experimentally. The subdetonative mode has been studied in the velocity range of 680–2600 m/s, the superdetonative mode has been demonstrated from 2000–2500 m/s (Mach 8.4), and the transdetonative mode has been shown to smoothly facilitate the transition from the subdetonative to superdetonative modes [2]. The ram accelerator starting envelope has been explored theoretically and experimentally, where experimental results have defined a stricter envelope [20]. Also of note, high-pressure testing up to 200 atm has been conducted to demonstrate high acceleration performance in excess of 46,000 g [21]. Additional discussions on SBRA experiments and theory can be found in the collection entitled, "Ram Accelerators" [22], or in the paper by Higgins [10].

1.4.2 Baffled Tube Ram Accelerator

Observation of the TCRA model results in Fig. 1.5 leads to the conclusion that more energetic propellants, with higher heat releases, produce higher ram accelerator thrust. It was also shown by Hertzberg et al. [1] that ballistic efficiency increases proportionally with non-dimensional thrust. Here, ballistic efficiency is defined as the ratio of the rate of change of the projectile kinetic energy to the rate of heat release of the propellant. Thus, both thrust and efficiency increase with the heat release of the propellant. However, there is a limit to the maximum heat release that can be used in a given ram accelerator configuration due to the unstarts that can occur, as discussed in section 1.3.3. For the SBRA, it was found that Q must be less than 6 [14, 15]. Ram propellants that satisfy this Q requirement are typically very fuel rich, with equivalence ratios well above two, or have significant amounts of diluent gases, often both. Therefore, there is significant practical interest, as well as engineering interest, in enabling the use of more energetic propellants in the ram accelerator.

The BTRA is a more recent ram accelerator configuration that allows significantly more energetic propellants to be used and was first introduced by Higgins et al. [23] and further discussed in Higgins' seminal paper [10]. In short, the baffles act as a one-way valve system that allows incoming gas to be compressed by the inlet diffuser, while preventing the combustion on the rear of the projectile from moving forward. This allows much more energetic propellants to be used. The BTRA consists of a tube made up of sequential baffle chambers linked together by a continuous rail system on which an

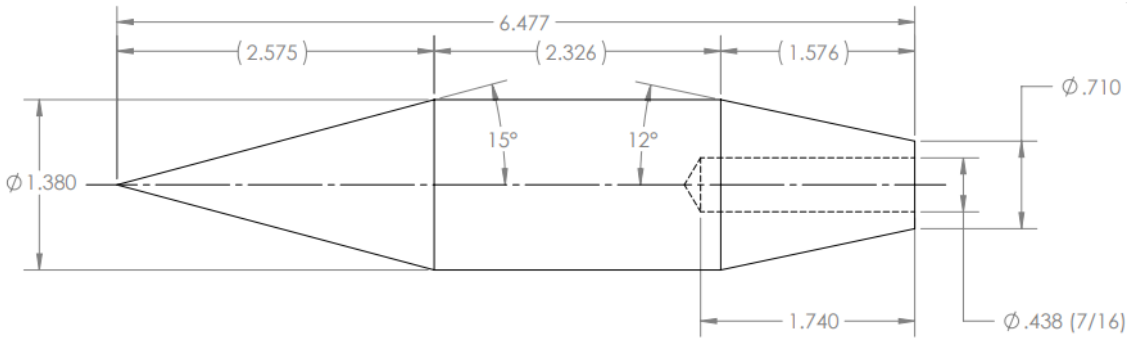

Fig. 1.11 The P300 projectile (dimensions in inches).

axisymmetric projectile travels. This allows the baffle chambers to have an arbitrarily large diameter, while the projectile is confined to the center of the bore. Additionally, the use of axisymmetric projectiles over finned-projectiles offers major advantages in terms of design complexity and manufacturability. One such projectile, dubbed the P300, is shown in Fig. 1.11. A schematic of the BTRA flowfield is shown in Fig. 1.12. For clarity, the rails are not shown in this schematic. The top image in Fig. 1.12 shows the wave structure of a started ram accelerator as it initially enters the baffles. The middle image shows the unstarted wave structure as the projectile shoulder reaches a new baffle wall. In this case, the small gap between the projectile shoulder and the baffle wall causes a shock wave to be pushed forward onto the nose cone, like the disgorging of a shock discussed in section 1.3.3, causing a localized unstart. This image also shows how the baffles are able to prevent the combustion from overtaking the projectile by closing off the flow path around the projectile shoulder. The lower image in Fig. 1.12 shows the re-started wave structure as the projectile progresses into the subsequent baffle chamber. In this case, the unstart wave has expanded to the full baffle chamber volume, allowing it to fall back onto the projectile shoulder, causing a re-start. This

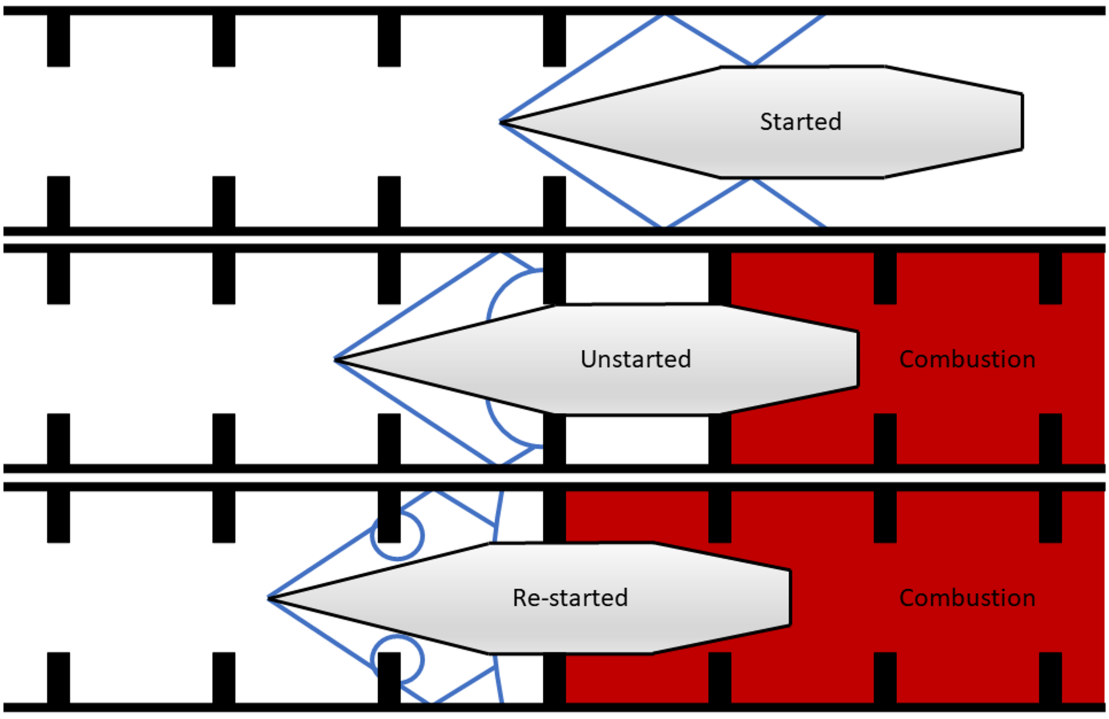

Fig. 1.12 BTRA flowfield as projectile travels through baffle chambers.

image also shows the combustion region progressing into the next baffle chamber as the flow path opens up between the baffle wall and the projectile tail cone. However, the combustion zone is held back by the next baffle wall that blocks the flow path beyond the projectile shoulder. It is this function that prevents the combustion from driving the shock system too far forward on the projectile and causing a permanent unstart, thus allowing the cycle of unstarts and re-starts to continue. This works as long as the projectile shoulder is at least the length of a single baffle chamber.

Initial BTRA experiments were carried out using *normal* baffles (where the baffles are perpendicular to the direction of projectile travel) [24], shown in Fig. 1.13a. In these experiments, it was shown that the BTRA could accommodate heat releases more than double the limit of the SBRA, reaching values of Q greater than 12. In these cases, the BTRA doubled the performance of the SBRA on a thrust per fill pressure basis. That said, the BTRA thrusts were still 15–50% lower than theory predicted. This discrepancy with theory indicated that either the theory needed to be refined or that the baffles needed to be better designed to reduce losses. It was also found that the BTRA could accommodate significantly lower velocity and Mach number operation than the SBRA. In these experiments, entrance velocities as low as 620 m/s (Mach 2.1) were demonstrated. Additional experiments were carried out using *inclined* baffles as CFD

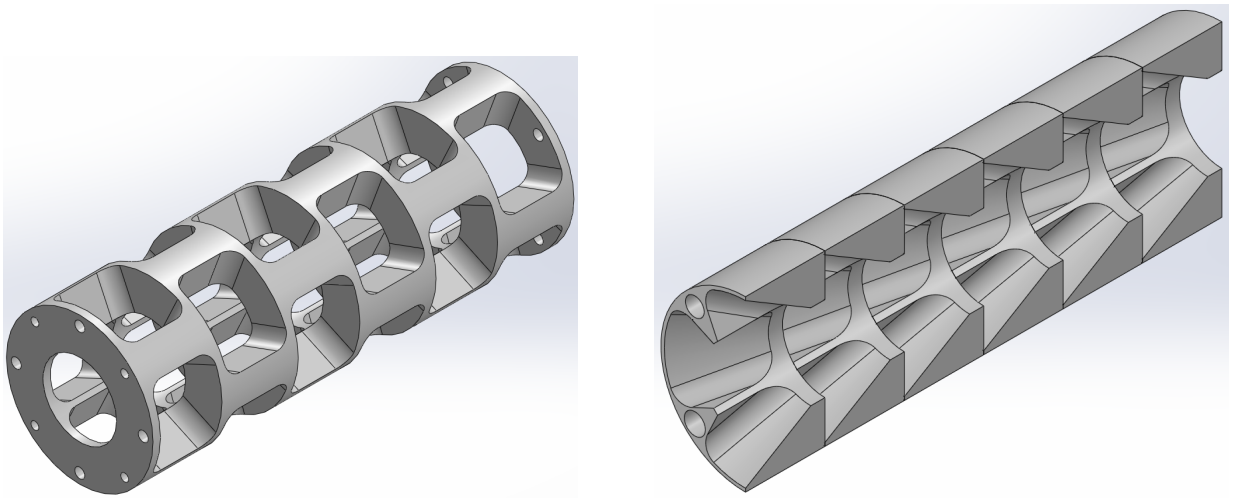

(a) **(b)**

Fig. 1.13 BTRA 100 normal baffle (a) and BTRA 200, 31° slanted baffle (b) CAD models.

simulations had predicted that they could improve thrust over the normal baffle configuration [25]. The inclined baffles are shown in Fig. 1.13b. These experiments found that the inclined baffles required slightly lower heat release propellants than the normal baffle configuration, while not producing significantly better performance. CFD simulations were carried out for both of these baffle configurations [26, 27]. More recently, the focus has returned to normal baffles with different geometries, propellants, and projectile designs being considered to more fully explore the capabilities of the BTRA and optimize performance.

Baffled Tube Ram Accelerator Model

The BTRA can be modeled in a similar manner as the general ram accelerator, with the addition of baffle drag terms. It should be noted that nearly all prior papers have presented this model with various errors present so all of the equations will be presented here for completeness. The control volume for the BTRA model is shown in Fig. 1.14. The main difference between the BTRA model and the general ram model is the addition of the moving baffle walls. In the projectile frame of reference, the baffle walls move in the rearward direction at the current projectile velocity (the incoming fluid velocity in this frame of reference). The baffle wall velocity is uniform throughout the domain. The effects of the baffles are aggregated into a single net force on the control volume, D. Since the baffles move in the rearward direction, this force acts on the control volume in the same direction. This is the same direction in which the force of projectile

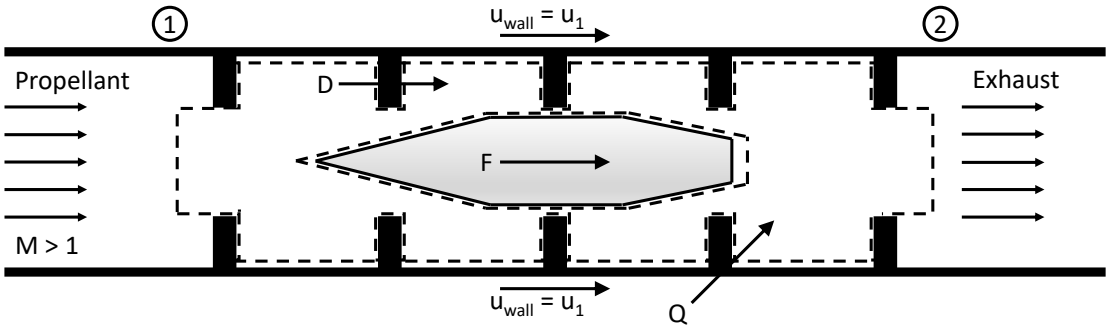

Fig. 1.14 Control volume for the BTRA.

acts on the control volume. This results in the scenario where the thrust and drag forces act in the same direction. This somewhat confusing circumstance is perhaps best resolved when considering a stationary reference frame. In the stationary frame, a high pressure region of gas travels with the projectile, propelling it forward. However, the gas also interacts with the stationary baffle blockages and pushes on them as well. This interaction is referred to as baffle *drag*. Thus, the momentum transfer from the gas is split between the projectile and the baffle walls and the force on each acts in the same direction (the direction of projectile travel).

To enable the BTRA model to be directly comparable to the SBRA model, the inlet and outlet areas are set to the inner bore area. Since the baffle effects are already captured within the D parameter, only the baffle volumes need to be accounted for to maintain direct parity with the SBRA model. This is done by equating the total fluid volume within a baffle section to an *effective* smooth bore section. The cross-sectional area of the equivalent smooth bore section is referred to as the effective area and is shown in Fig. 1.15. Finally, the ratio of the effective area to the actual bore area of the BTRA is defined as β, the volume void ratio. This β parameter, unique for a given BTRA geometry, is used to directly scale the non-dimensional thrust to be comparable to the SBRA. The effective area and volume void ratio are defined in Eqs. (1.9) and (1.10).

$$A_{eff} \equiv \frac{V_{f,BTRA}}{L_{BTRA}} = \frac{V_b + V_c - V_{rail}}{L_b + L_c} \tag{1.9}$$

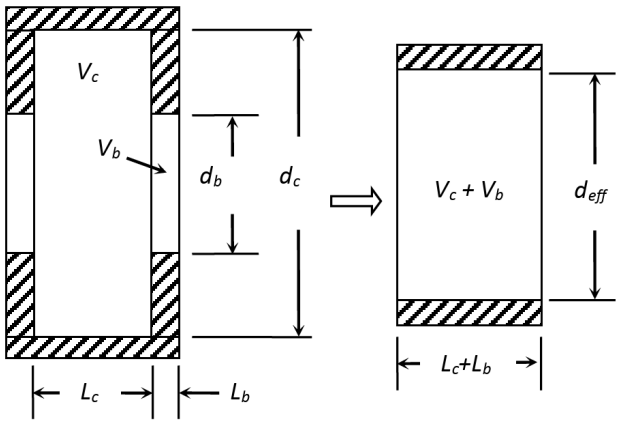

Fig. 1.15 Effective area for a BTRA section [24].

$$\beta \equiv \frac{A_{eff}}{A_b} \tag{1.10}$$

In Eq. (1.9), V_{rail} represents the volume occluded by any rails present, including any fillet features. However, in practice, the first ratio in Eq. (1.9) is typically used for a given BTRA design as $V_{f,BTRA}$ can be calculated directly in computer aided design (CAD) software.

The conservation equations are now applied to the control volume in Fig. 1.14, yielding the following relations for the BTRA:

$$\rho_1 u_1 = \rho_2 u_2 \,, \tag{1.11}$$

$$\rho_1 u_1^2 + p_1 + \frac{F+D}{A_b} = \rho_2 u_2^2 + p_2 \,, \tag{1.12}$$

and

$$h_1 + \frac{u_1^2}{2} + \Delta q + \frac{D}{\rho_1 A_b} = h_2 + \frac{u_2^2}{2} \,. \tag{1.13}$$

Equation (1.11) is identical to Eq. (1.1) in the general ram accelerator model. Equations (1.12) and (1.13) are identical to their respective counterparts, Eqs. (1.2) and (1.3), except for the addition of the drag terms. Note that the sign on the drag term in Eq. (1.12) matches the thrust term, as discussed above. Additionally, the baffle drag adds energy to the system, in the projectile reference frame, since the baffles do work on the control volume. This baffle drag work is represented by the fourth term on the left hand side of Eq. 1.13. These equations can be non-dimensionalized and solved, as in the general ram accelerator model, to produce the BTRA non-dimensional thrust equation

$$I_{BTRA} = \frac{1}{\beta}\left(\frac{\gamma_1 M_1}{\gamma_2 M_2}(1+\gamma_2 M_2^2)\sqrt{\left(\frac{\gamma_2-1}{\gamma_1-1}\right)\left(\frac{\frac{h_1}{c_{p1}T_1}+\frac{\gamma_1-1}{2}M_1^2+Q+\frac{D}{p_1 A_b}\left(\frac{\gamma_1-1}{\gamma_1}\right)}{\frac{h_2}{c_{p2}T_2}+\frac{\gamma_2-1}{2}M_2^2}\right)}-(1+\gamma_1 M_1^2)-\frac{D}{p_1 A_b}\right). \tag{1.14}$$

Assuming thermally choked operation, Eq. (1.14) can be simplified to

$$I_{BTRA,TC} = \frac{1}{\beta}\left(\frac{\gamma_1 M_1}{\gamma_2}(1+\gamma_2)\sqrt{\left(\frac{\gamma_2-1}{\gamma_1-1}\right)\left(\frac{\frac{h_1}{c_{p1}T_1}+\frac{\gamma_1-1}{2}M_1^2+Q+\frac{D}{p_1 A_b}\left(\frac{\gamma_1-1}{\gamma_1}\right)}{\frac{h_2}{c_{p2}T_2}+\frac{\gamma_2-1}{2}}\right)}-(1+\gamma_1 M_1^2)-\frac{D}{p_1 A_b}\right). \tag{1.15}$$

Equation (1.15) is the non-dimensional thrust for the thermally choked BTRA. Here, and in Eq. (1.14), the volume void ratio, β, shows up to correct for the extra volume in the baffle chambers and produce a non-dimensional thrust for comparison with the SBRA.

Various models of the baffle drag force, D, have been proposed. First, it was assumed that the thermally choked plane, acting similar to a detonation wave, would experience form drag, shock wave total pressure loss, and viscous drag as it travels through the baffles [24]. This is supported by a series of experiments that show that low pressure detonation waves travel slower through baffled tubes than through smooth bore tubes [28]. To account for these effects, while maintaining the simplicity of the current ram performance models, a baffle drag coefficient is considered. Combining the baffle drag coefficient with the thermally choked plane fluid density and its velocity in the stationary reference frame ($u_{2,lab} = u_1 - u_2$), the baffle drag force can be written as

$$D = \frac{1}{2} c_d \rho_2 u_{2,lab}^2 A_{eff} = \frac{1}{2} c_d \rho_2 (u_1 - u_2)^2 A_b \beta \,, \tag{1.16}$$

using the effective area as the reference area. This formulation allows the baffle drag coefficient to be determined empirically. As shown in Fig. 1.16, where this model is referred to as "Model 1", the drag causes a reduction in non-dimensional thrust at all Mach numbers except at the peak thrust Mach number. This is because the flow at the thermally choked plane is stationary in the tube at the peak thrust Mach number. Since the drag in this model is based on the drag of the thermally choked plane, there is no drag when the thermally choked plane is stationary. Of course, this does not match the physical reality in which drag losses to the baffles will occur when there is fluid motion in any part of the control volume. That said, to incorporate a more physical representation of the drag, a much more detailed model will be required.

A second drag model was proposed that introduced a few refinements to the initial model [25]. First, the reference density was changed to the free stream density, instead of the density at the thermally choked plane. Additionally, the projected area of the baffle was used as the area reference as it better represents the area of baffle interaction with the flow. Most significantly, however, the flow direction at the thermally choked plane was added into the model. This was, as the authors argued, to account for the potential

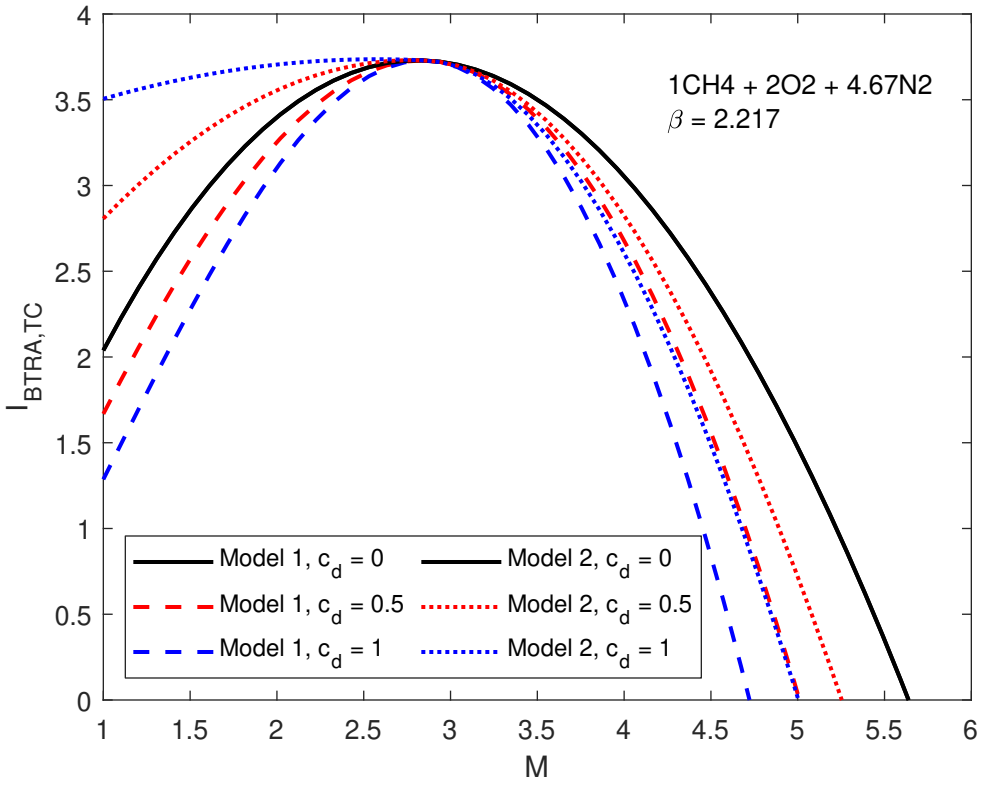

Fig. 1.16 Non-dimensional thrust versus Mach number for two BTRA drag models.

increase in thrust due to the rearward flow of gases interacting with the baffles, causing higher pressures to be generated on the projectile base. In effect, this causes the drag term to *add* to projectile thrust at all Mach numbers below the peak thrust Mach number. This baffle drag formulation is given by

$$D = \frac{1}{2} c_d \rho_1 |u_1 - u_2| (u_1 - u_2)(A_c - A_b) \tag{1.17}$$

and plotted as "Model 2" in Fig. 1.16. This model should be considered with caution. In this model, it is assumed that the change in flow direction (in the stationary frame) causes an increase in pressure at the projectile base. This assumption ignores similar effects on the rest of the projectile, where the baffles could also affect the local pressures around the projectile. Thus, in order to accurately capture the net effects of the baffles, a detailed flow model that captures the flow phenomena around the entire projectile and local baffles would be required. Since that is beyond the scope of this type of model, this effect should be considered with caution.

It should be noted that the non-dimensional thrust curves shown in Fig. 1.16 differ slightly from their counterparts in their source papers. This is because in each of those papers, the authors plotted results for constant heat release and specific heats across the control volume, while no such simplification was made here. Additionally, the non-dimensional thrusts presented in Fig. 1.16 are much lower than those presented in their respective source papers since those presented here were adjusted by the volume void ratio for a typical BTRA ($\beta = 2.217$), while the original papers did no such adjustment.

It is clear from the shortcomings of these two baffle drag models that a more refined model is required to better understand and capture the real physics of the BTRA. The existing drag model framework, while reasonable for the fidelity it attempts to capture, requires some further refinement. However, a more detailed model that considers the entire flowfield surrounding the projectile will likely be required to accurately capture the full effects of baffles on ram accelerator performance.

1.4.3 Railed Tube Ram Accelerator

The BTRA introduced a feature that is desirable for all ram accelerators: axisymmetric projectiles. The removal of the fins from traditional ram accelerator projectiles significantly simplifies the projectile design and manufacture process. This also opens up the ram accelerator to be more innately compatible with similar guns or gun-like systems. However, past BTRA experiments have only demonstrated operation at or below Mach 4 and about 1200 m/s. While there are plans to continue testing the BTRA at higher Mach numbers and velocities, there is some desirability to make an SBRA-like system that is compatible with the BTRA and its axisymmetric projectiles. In this setup, a ram accelerator can take advantage of the low Mach number and velocity capabilities of the BTRA while still being able to rely on the already demonstrated high velocity performance of the SBRA, capable of achieving velocities in excess of 2500 m/s. Thus, the previously developed railed tube ram accelerator was a natural choice.

The RTRA consists of a smooth bore tube with a series of rails rigidly attached to the inner bore. These rails take up the function of the projectile fins by keeping the axisymmetric projectile centered in the tube bore. An example of an RTRA section is pictured in Fig. 1.17. The first RTRA experiments were

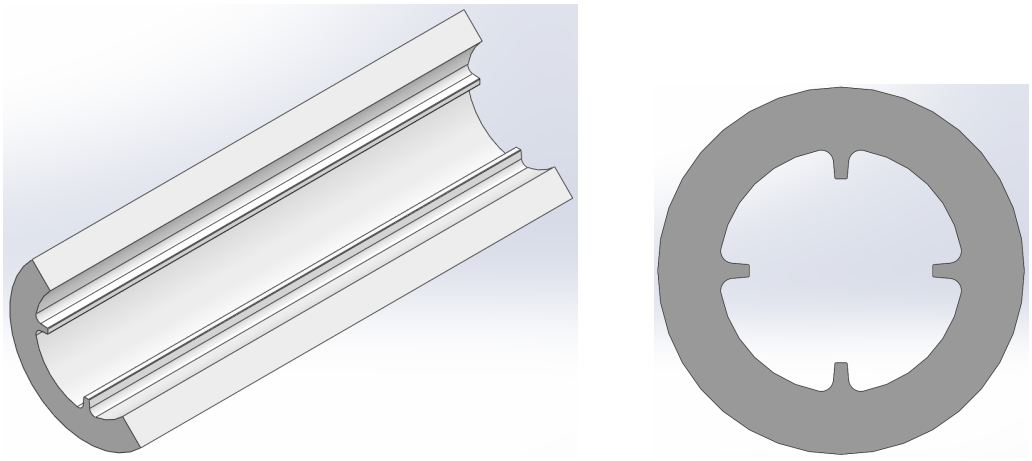

(a) (b)

Fig. 1.17 RTRA 200 side cut view (a) and cross-sectional view (b).

carried out at the French-German Research Institute of Saint-Louis, France [29]. In those experiments, superdetonative operation was demonstrated and it was found that the RTRA could operate with heat releases much closer to the theoretical limit. This was an intriguing result, as it showed that it may be more advantageous to operate in the superdetonative mode in the RTRA, whereas in the SBRA it had been typically more efficient to remain in the subdetonative mode as long as possible. This finding sets up the RTRA as a compelling option as a post-BTRA ram stage for efficient, high-velocity operation. Further testing is still required to more fully explore RTRA operation and its limits, especially for its use in conjunction with a BTRA.

Railed Tube Ram Accelerator Model

The RTRA can be modeled in the same manner as the SBRA, using the volume void ratio from the BTRA model. This allows the volume taken up by the rails to be accounted for. Here, the effective area is defined as

$$A_{eff} \equiv \frac{V_{f,RTRA}}{L_{RTRA}} \tag{1.18}$$

and the volume void ratio is still defined by Eq. (1.10). Since the RTRA typically has a constant cross-section, the effective area is equivalent to the fluid cross-sectional area. Using the volume void ratio, the

non-dimensional thrust of the RTRA can be written as

$$I_{RTRA} = \frac{1}{\beta}\left(\frac{\gamma_1 M_1}{\gamma_2 M_2}(1+\gamma_2 M_2^2)\sqrt{\left(\frac{\gamma_2-1}{\gamma_1-1}\right)\left(\frac{\frac{h_1}{c_{p1}T_1}+\frac{\gamma_1-1}{2}M_1^2+Q}{\frac{h_2}{c_{p2}T_2}+\frac{\gamma_2-1}{2}M_2^2}\right)}-(1+\gamma_1 M_1^2)\right), \tag{1.19}$$

while the thermally choked RTRA non-dimensional thrust is written as

$$I_{RTRA,TC} = \frac{1}{\beta}\left(\frac{\gamma_1 M_1}{\gamma_2}(1+\gamma_2)\sqrt{\left(\frac{\gamma_2-1}{\gamma_1-1}\right)\left(\frac{\frac{h_1}{c_{p1}T_1}+\frac{\gamma_1-1}{2}M_1^2+Q}{\frac{h_2}{c_{p2}T_2}+\frac{\gamma_2-1}{2}}\right)}-(1+\gamma_1 M_1^2)\right). \tag{1.20}$$

These equations are identical to the SBRA equations, Eqs. (1.7) and (1.8), aside from the scaling factor β. This highlights the fact that the RTRA and SBRA are theoretically identical in terms of operation, where the scaling factor is applied only to account for the volume differences due to the rails.

1.5 Additional Ram Accelerator Models

Various refinements and alternatives have been proposed for the ram accelerator models discussed above. The influence of unsteady effects on ram accelerator performance was first discussed and formulated by Bruckner et al. [30] and found to be negligible for typical ram accelerator operating conditions (~15,000 g). It was predicted that unsteady effects would remain negligible up to 30,000–40,000 g. Later, Bundy et al. [21] showed experimentally that unsteady effects became significant at projectile accelerations above 30,000 g. These experiments were carried out at high pressures (15–20 MPa) and the unsteady model indicated that the significant unsteady effects arise when the propellant mass in the control volume is of the same order of magnitude as the projectile mass. It was also found that combining the unsteady model with a real gas equation of state (EOS), the Boltzman EOS in this case, led to the best agreement with experiment.

The standard ram accelerator model has been improved by implementing various real gas equations of state. The real gas effects on ram accelerator performance prediction was first presented by Bauer et al [31].

It was found that by utilizing the the Boltzman EOS with the typical steady ram accelerator model led to significantly more accurate performance predictions throughout the thermally choked operating regime. This was, of course, further validated by Bundy et al. [21] in the high pressure testing discussed above. More recently, the EOS effects on unsteady ram models was compared against experiments at different bore sizes [32]. In this study, both the Boltzman EOS and the Becker-Kistiakowsky-Wilson (BKW) EOS were compared to experiments with tube bores ranging from 25 to 120 mm. These models showed good agreement with experiments but it was also found that a different EOS model may agree better with experiments depending on the bore size and fill pressures. In general, the BKW EOS predicted higher performance than the Boltzman EOS.

Numerous CFD studies have been carried out on the ram accelerator. There are far to many to detail here, but many of the SBRA CFD studies are summarized by Bruckner [33]. While many of these CFD studies have been able to capture the major flow features of the ram accelerator, none have yet been able to achieve enough accuracy to be able to predict performance and influence future ram accelerator designs and developments. CFD efforts are still ongoing with more recent work focusing on modeling the BTRA [26, 27]. There is still a lot of work needed to bring ram accelerator CFD modeling up to the fidelity required to make it a viable prediction and design tool.

Chapter 2

Experiments

The experimental goals of this work include the development and testing of new BTRA and RTRA hardware, a survey of propellant viability for the BTRA, the development and validation of an RTRA with 'sweeper baffles,' and the development and testing of a new technology for obturator-less ram starting. The data generated in this experimental effort are also used for comparison and validation with the new computational model discussed in Chapter 3. In this chapter, the UW Ram Accelerator Lab is detailed, including descriptions of all ram accelerator tubes and projectiles, followed by a description and presentation of results for each experimental effort listed above. This chapter concludes with a summary discussion of the experimental results and outstanding questions.

2.1 Experimental Facility

All experiments discussed herein were conducted at the UW Ram Accelerator Lab. This unique facility is specially equipped to carry out high-velocity ram accelerator experiments. A schematic of the ram accelerator system is shown in Fig. 2.1. The light gas gun utilizes compressed helium to accelerate the projectile through the evacuated launch tubes, reaching the desired velocity upon entrance to the ram accelerator section. An evacuated dump tank is connected to a perforated section of the launch tube to relieve residual gun gas pressure behind the projectile, minimizing its interference with the ram starting process. The

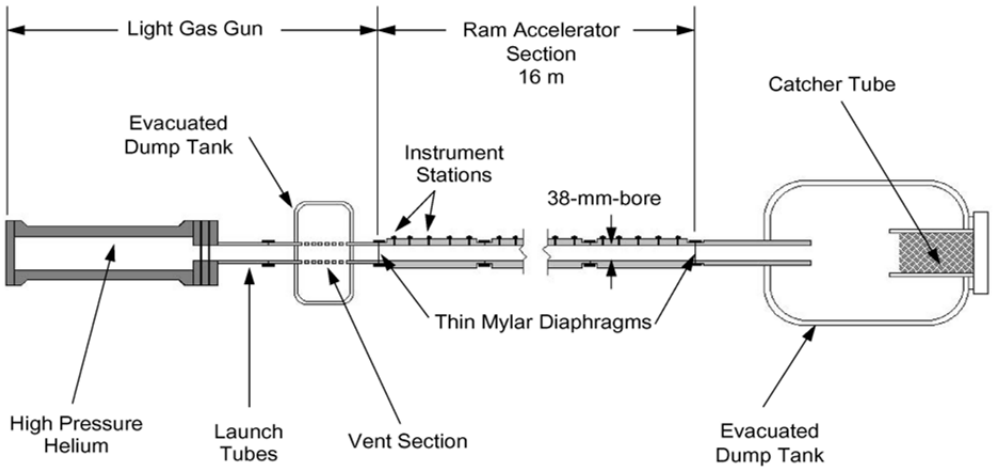

Fig. 2.1 Schematic of the UW ram accelerator system.

16-m-long ram accelerator test section consists of eight, 2-m-long tubes that can be individually replaced with compatible ram tube sections. Each tube can be optionally sealed off from adjacent tubes via Mylar diaphragms. For the experiments discussed herein, a number of these sections were replaced with 2-m-long shell tubes, containing either baffle or rail inserts. Additionally, each tube has regularly spaced instrument port holes to allow various measurements to be made throughout the test section. These tubes are further detailed in Section 2.1.1. All tubes in the system have a nominal bore diameter of 38 mm. A second dump tank is located downstream of the ram accelerator test section. The downstream dump tank significantly increases the total system volume, ensuring that the post-shot gas pressure remains low for safer and easier system recycling.

Instrumentation for the system primarily consists of two sensor types: piezoelectric pressure transducers and electromagnetic (EM) sensors. One of each is positioned at each instrumentation station throughout the test section. The pressure transducers are PCB Piezotronics 119 series sensors that are capable of measuring the high speed pressure waves present throughout each experiment. The pressure profile measured at each station can be analyzed to determine combustion pressures, classify ram operability, and calculate wave speeds. The EM sensors are in-house designed and manufactured probes that, in conjunction with a projectile mounted magnet, can generate a signal upon projectile passage [34]. This signal is analyzed to generate time-of-passage data for the projectile, allowing projectile location and velocity to be

tracked throughout the tube. To work in the BTRA, the EM probe design is modified so that the probe tip extends into the baffle chamber, instead of flush with the exterior surface, so that signal strength is sufficient for detection and measurement. Data from all sensors is collected and recorded by a National Instruments PXIe-1071 chassis with two PXIe-6358 modules. This system allows up to 32 analogue input channels to be simultaneously sampled at up to 1.25 MHz.

Uncertainties

As discussed above, all projectile velocities and accelerations are calculated using the time of passage measurements from the EM sensors. Non-dimensional thrusts and ballistic efficiencies are ultimately calculated using these measurements as well. An in-depth analysis and derivation of the uncertainties in these measurements at the UW ram lab was conducted by Knowlen [35] and the results are summarized here. The relative uncertainty in each velocity calculation is generally less than 2%. The relative uncertainties in the calculated accelerations are generally less 7%, for the experimental velocities discussed herein. The uncertainties in propellant mixture compositions are minimized through regular calibrations so that mixture composition uncertainties do not result in any meaningful difference in propellant sound speeds. Thus, Mach number calculations also have a relative uncertainty of less than 2%.

2.1.1 Ram Accelerator Tubes

The ram tube sections of the UW Ram Accelerator Lab utilize a series of shell tubes and inserts. Each 2-m-long shell tube can accommodate inserts, baffle or rail, in any combination. The shell tubes feature five equally spaced instrumentation stations along the length of the tube, having a pair of ports positioned 180° from each other at each station. These ports are typically filled with pressure transducers and EM probes for simultaneous pressure measurement and projectile detection at each station. Additionally, a third port is located at the tube center to accommodate the gas fill line. The experiments discussed herein utilized three primary insert designs: the BTRA 100, the BTRA 500, and the RTRA 200.

BTRA 100

The BTRA 100, shown in Fig. 2.2a, is a normal baffle (90° to the flow) with a 76.2 mm chamber diameter. Each baffle insert has a total length is 35.7 mm, including a 3.8 mm long baffle wall. The BTRA 100 has no outer walls and instead uses the shell tube inner surface as the outer baffle chamber wall. This particular design features clocked baffles, where each subsequent baffle insert is rotated 45°, with respect to the prior, so that the baffle walls are reinforced at the center of their spans by the rails. This was intended to help strengthen the baffles against the axial forces they experience during operation. However, it was found to have the opposite effect. In practice, the axial force applied to each baffle wall was instead transmitted through the rail to the subsequent baffle wall, stacking throughout the region around the passing projectile. The larger than expected loads were then transmitted to a baffle wall at its weakest point (center of the span), causing warping and failure at lower than expected experiment pressures.

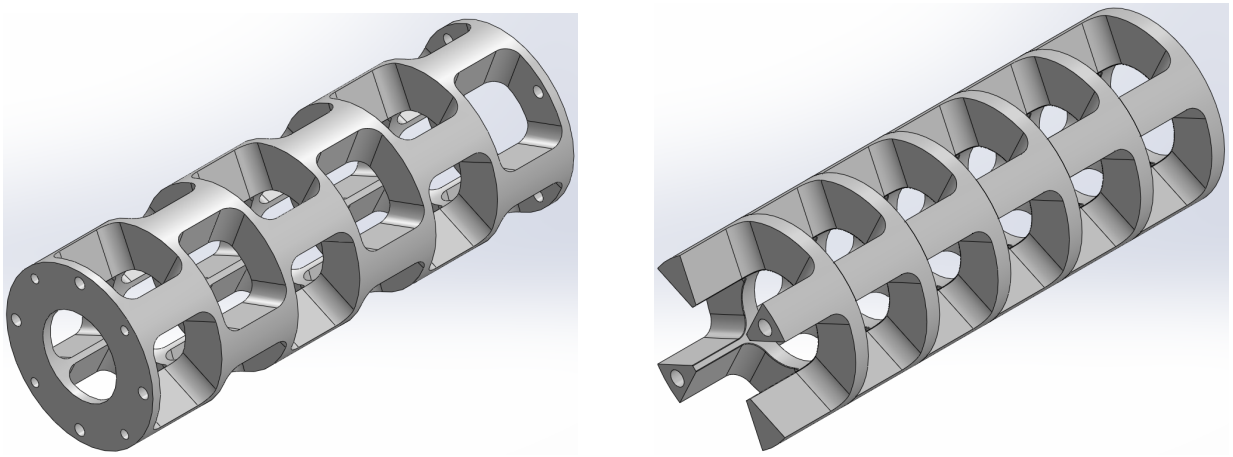

(a) **(b)**

Fig. 2.2 BTRA 100 normal baffle (a) and BTRA 110 normal baffle (b) CAD models.

The newly developed BTRA 110, shown in Fig 2.2b, is a redesign of the BTRA 100. This design removes the clocked baffles and separates each individual baffle into individual inserts. The baffle wall length was also increased to 6.4 mm to increase its strength. The BTRA 110 was shown to have identical performance to the BTRA 100, while being able to withstand significantly higher experiment pressures. Consequently, the BTRA 110 ended up completely replacing the BTRA 100. For simplicity, both the

BTRA 100 and 110 will be referred to as the BTRA 100 for the remainder of this paper, unless the distinction is otherwise relevant.

BTRA 500

The newly developed BTRA 500, shown in Fig 2.3, is a normal baffle with a 63.5 mm chamber diameter. The total insert length is 35.7 mm (equal to the BTRA 100/110) with a 6.4 mm long baffle wall (equal to the BTRA 110). The BTRA 500 was designed with two goals in mind: achieve higher strength than the BTRA 100 design and have a chamber diameter smaller than the BTRA 100 to allow the study of the effect of chamber diameter on BTRA performance. The fully enclosed baffle chamber design achieved both of these goals and the BTRA 500 became the new baseline baffle design. This design also featured fillets on the bases of the rails and the baffle walls to further improve its strength.

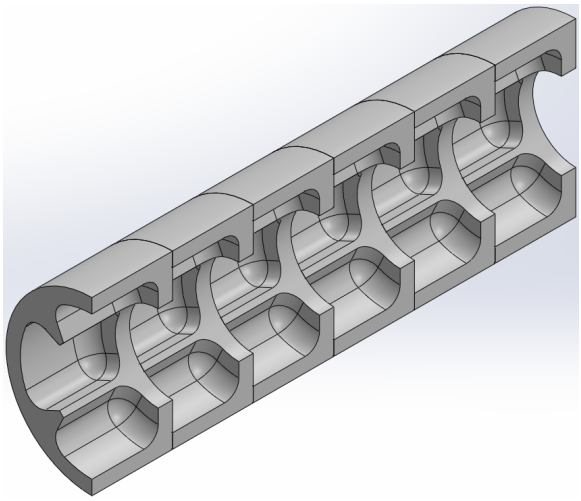

Fig. 2.3 BTRA 500 normal baffle CAD model.

RTRA 200

The newly developed RTRA 200, shown in Fig 2.4 is the second iteration of a railed tube implemented at UW. The design features a fully enclosed shell that reduces the effective tube diameter to 50.8 mm. This diameter was chosen to match the area ratios used in typical smooth bore configurations. The design also features four continuous rails, designed to match the fins used on prior smooth bore projectiles. Since

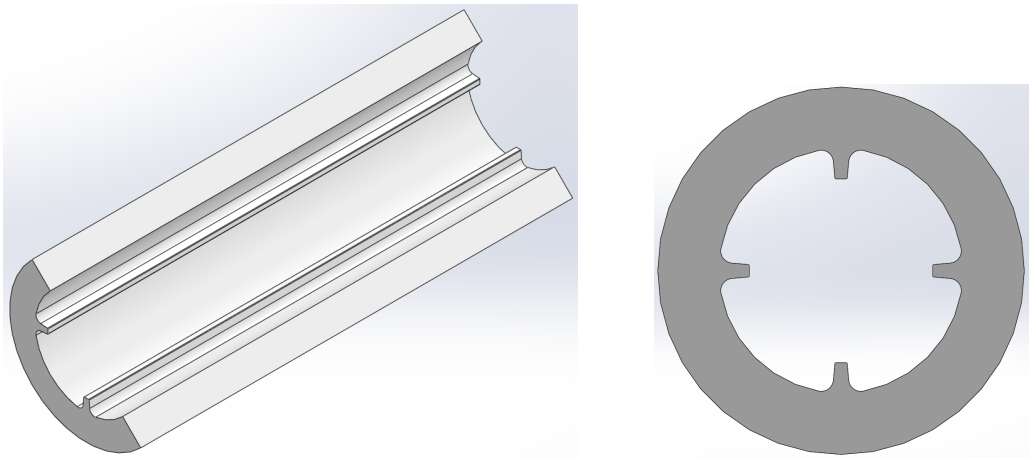

(a) (b)

Fig. 2.4 RTRA 200 side cut view (a) and cross-sectional view (b).

the rail bore diameter is consistent with all other tubes and inserts, the RTRA 200 is compatible with all other baffle designs and can be implemented in hybrid, baffle-rail configurations.

2.1.2 Ram Accelerator Projectiles

All experiments were carried out using one of two primary projectiles: the P300 and the P496-2BL. Both axisymmetric projectiles were made of polycarbonate. Drawings of each projectile can be found in Fig. 2.5. The P300 projectile featured a 35.1 mm shoulder diameter, while the P496-2BL projectile featured a 38.0 mm shoulder diameter. The larger diameter P496-2BL projectile was sized to fully occlude the inner bore of the ram tubes by maintaining a tight fit between the projectile shoulder and the tube walls (or rails). The P496-2BL also features a two-baffle-length long shoulder for increased baffle chamber occulsion. Both projectiles had identical nose cone and tail cone half-angles at 15° and 12°, respectively. Additionally, they both featured a truncated base with an 18.0 mm diameter.

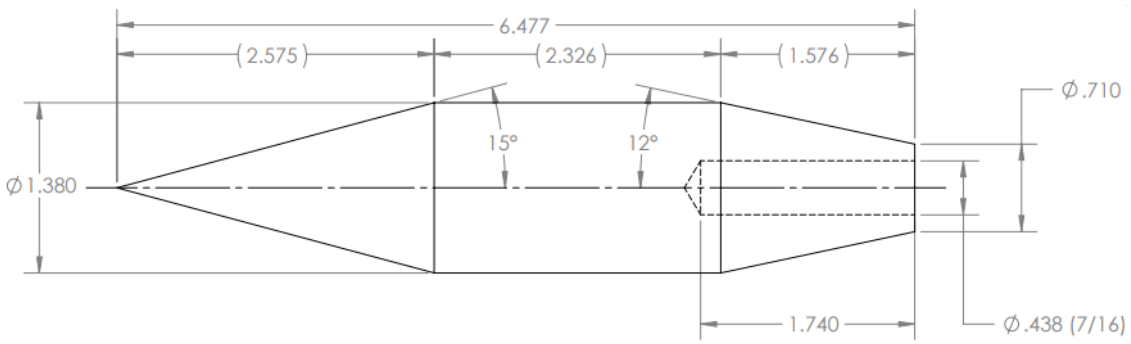

(a)

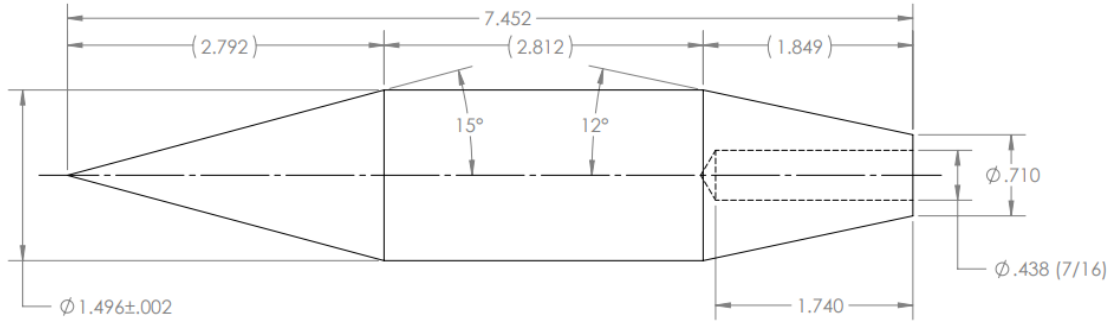

(b)

Fig. 2.5 P300 (a) and P496-2BL (b) projectile drawings (dimensions in inches).

Obturators

All experiments, except where otherwise noted, utilized the O101 obturator, shown in Fig. 2.6. This obturator was used in conjunction with a projectile to facilitate the launch and ram starting processes for each experiment. The nominal obturator diameter was 37.9 mm, making it a tight fit between the obturator and tube wall when pressurized with light gas gun propellant (helium). More discussion on the role of the obturator can be found in Section 1.4.1 and the following references [18, 19].

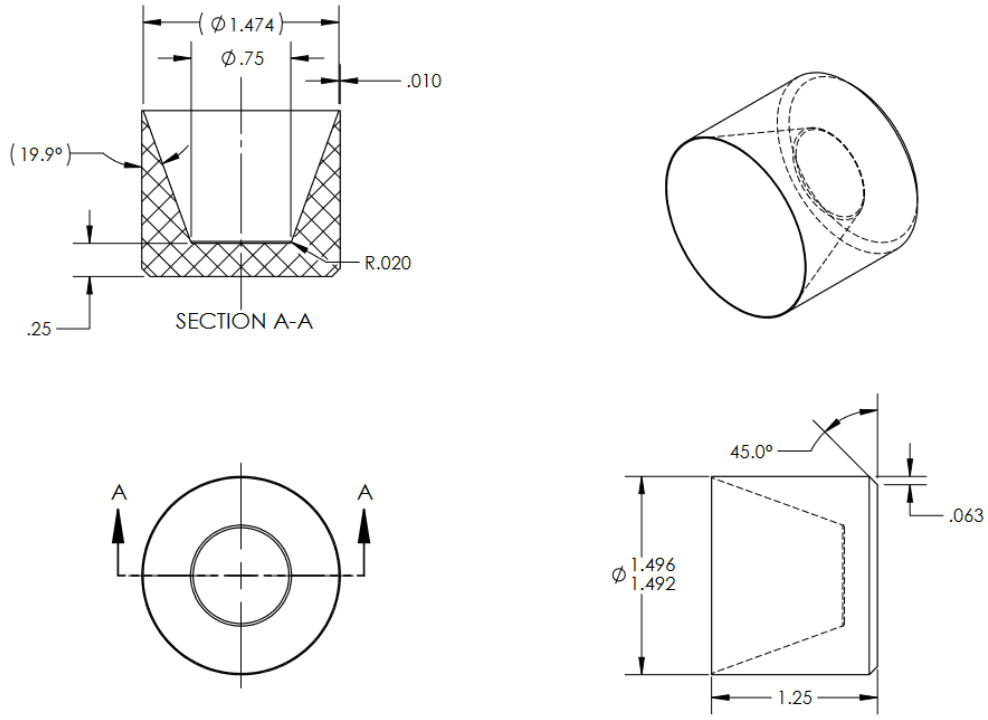

Fig. 2.6 O101 obturator drawing (dimensions in inches).

2.2 BTRA 500 Experiments

The BTRA 500, detailed in Section 2.1.1, was a newly developed baffled tube configuration featuring a smaller, 63.5 mm baffle chamber diameter. This baffled tube was designed to study the effects of baffle chamber diameter on ram accelerator operation. A series of experiments was carried out to compare the thrust performance, efficiency, and operational envelope of the BTRA 500 to the BTRA 100. A portion of this test series was originally presented in a paper by Leege, et al. [36], but the full results are presented here with additional discussion.

Figure 2.7 shows the non-dimensional thrust and ballistic efficiency versus average Mach number for both the BTRA 500 and BTRA 100. The ballistic efficiency is defined here as the total change in kinetic energy of the projectile divided by the available chemical energy of the propellant, using the lower heating value of the reacting fuel to calculate the chemical energy. In each of these experiments, a P300 projectile was shot through a 2-meter-long ram stage that was filled with methane and enriched-air propellant (1CH_4

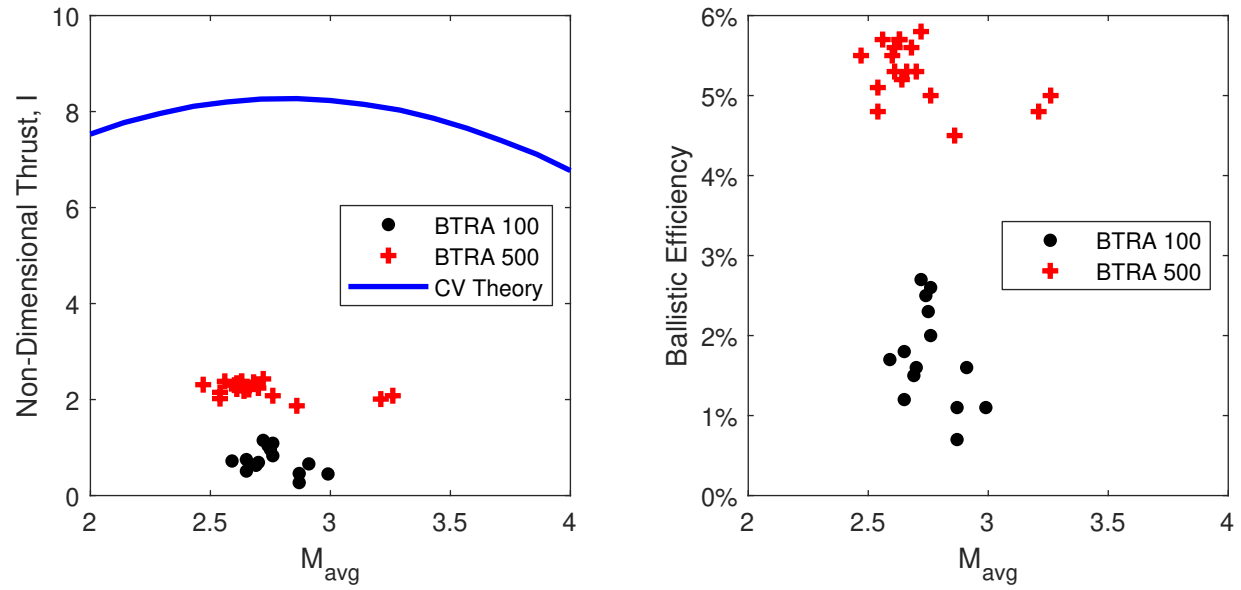

(a) **(b)**

Fig. 2.7 Non-dimensional thrust (a) and ballistic efficiency (b) versus average Mach number in BTRA 500 and BTRA 100 experiments with 1CH4 + 2O2 + 4.67N2 propellant, including the theoretical non-dimensional thrust curve (drag excluded).

+ 2O2 + 4.67N2) at fill pressures ranging from 11.2 to 31.6 atm. As shown in Fig. 2.7a, on average, the non-dimensional thrust in the BTRA 500 triples that achieved in the BTRA 100, where the average non-dimensional thrusts are 2.22 and 0.73, respectively. However, the thrusts in both baffled tubes are significantly lower than theory predictions (as discussed in Sections 1.3 and 1.4.2). Similarly, the ballistic efficiencies in the BTRA 500 are about three times higher than in the BTRA 100, as shown in Fig. 2.7b. The average ballistic efficiency was 5.3% in the BTRA 500 and 1.7% in the BTRA 100.

Although the performance was significantly higher in the BTRA 500 than the BTRA 100, the operational envelope was found to be smaller. Figure 2.8 shows the non-dimensional heat release versus entrance Mach number for a series of experiments with P300 projectiles in the BTRA 500 and BTRA 100, indicating which cases started and unstarted. All of these experiments used the same propellant class (1CH4 + 2O2 + xN2) with only minor variations in heat release due to small changes in composition and Mach number. The minimum required Mach number to operate in the BTRA 500 was about 2.15, while the minimum Mach number in the BTRA 100 was about 1.85. Upper Mach number limits have not yet

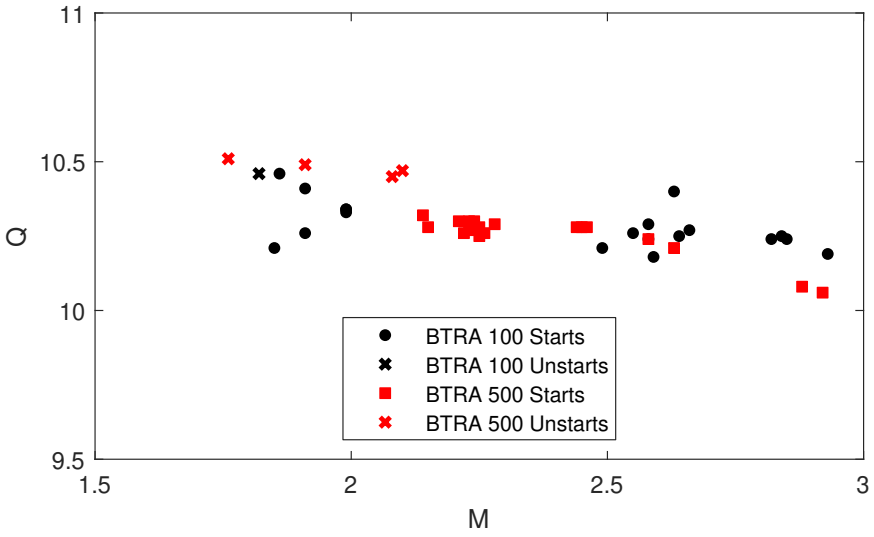

Fig. 2.8 Non-dimensional heat release versus entrance Mach number for BTRA 500 and BTRA 100 experiments with 1CH4 + 2O2 + xN2 propellant, highlighting starts versus unstarts.

been experimentally found for any BTRA configuration, though the peak Mach number achieved thus far was Mach 4.0.

2.3 RTRA 200 Experiments

The RTRA 200, detailed in Section 2.1.1, was a second generation railed tube system designed to achieve the high performance of the SBRA, while accommodating the use of axisymmetric projectiles. A test series was executed to determine its performance and operating window, namely the Mach number and propellant heat release limits. These experiments utilized the P300 projectiles and methane-air propellants (ϕCH4 + 2O2 + 7.52N2) at fill pressures ranging from 11.9 to 31.6 atm. Initial results were first presented by Leege et al [36]. That initial test series established the range of operable propellant mixtures to be 1.6 < ϕ < 2.0 at fill pressures below 14.6 atm.

Testing continued at pressures ranging from 21.4 to 31.6 atm, where it was quickly found that an equivalence ratio of 2.2 was required for stable operation in the RTRA 200 at these pressures. Figure 2.9 shows the non-dimensional thrust and ballistic efficiency versus average Mach number for the RTRA 200 at ϕ = 2.2, plotted next to the BTRA cases from Fig. 2.7. The experimental thrusts for the RTRA match

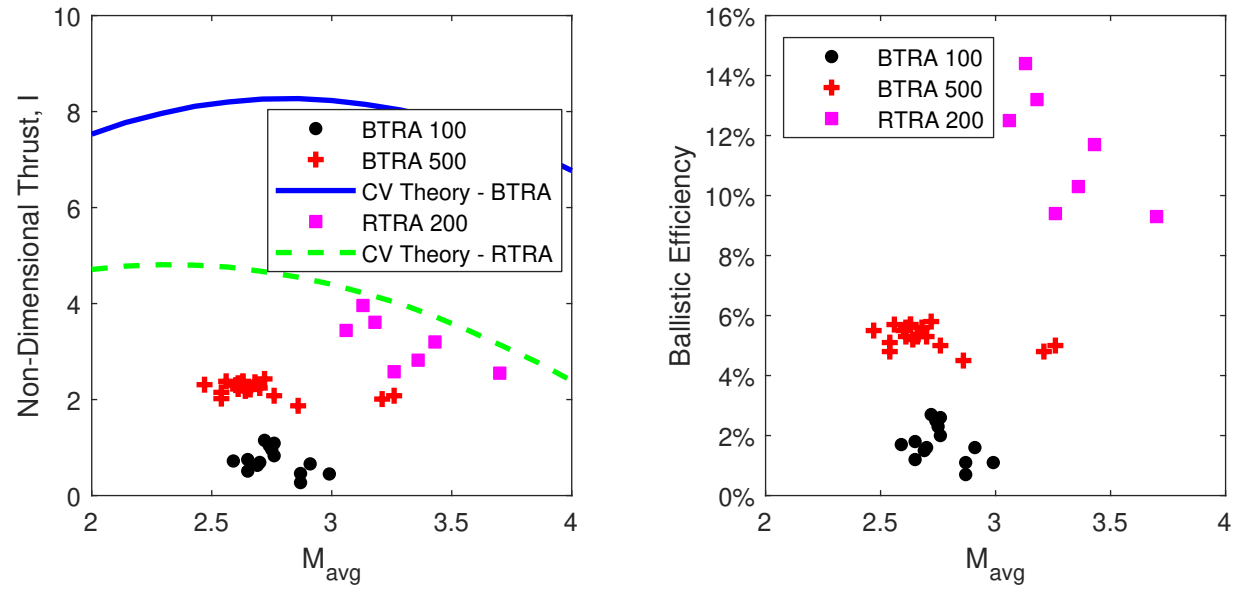

(a) (b)

Fig. 2.9 Non-dimensional thrust (a) and ballistic efficiency (b) versus average Mach number in RTRA 200 experiments with 2.2CH4 + 2O2 + 7.52N2 propellant, including theoretical non-dimensional thrust curves. BTRA 500 and BTRA 100 data included for comparison.

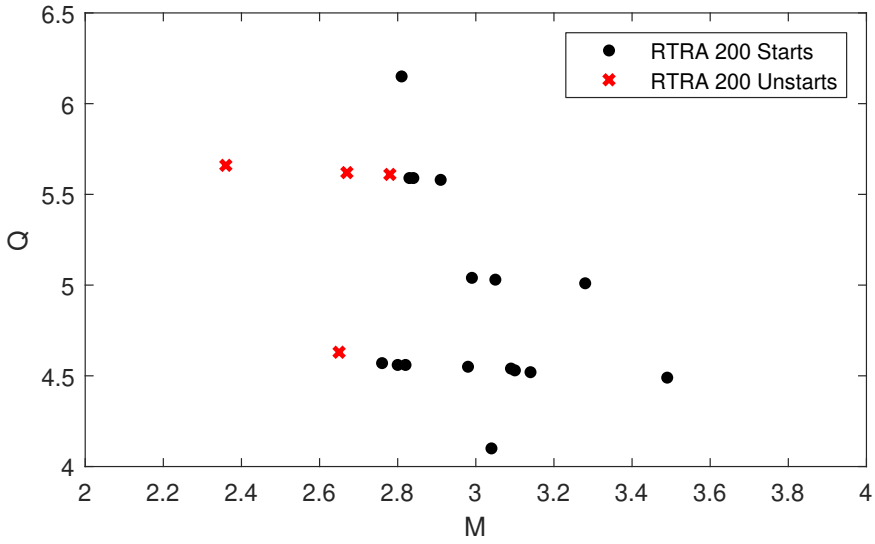

Fig. 2.10 Non-dimensional heat release versus entrance Mach number for RTRA 200 experiments with ϕCH4 + 2O2 + 7.52N2 propellant, highlighting starts versus unstarts.

the theory predictions fairly well, only slightly underperforming. The average non-dimensional thrust in the RTRA 200 was 3.17, 1.4 times higher than the BTRA 500 and 4.3 times higher than the BTRA 100.

The average ballistic efficiency was 11.5%, 2.2 times higher than the BTRA 500 and 6.6 times higher than the BTRA 100.

Currently, only the minimum entrance Mach number has been identified for the RTRA 200 and no upper Mach number limit has been found. Figure 2.10 shows the non-dimensional heat release versus entrance Mach number for this test series in the RTRA 200. The minimum entrance Mach number was found to be about 2.8.

2.4 BTRA Propellant Study

A BTRA propellant study was conducted to identify and characterize various propellants for use in the BTRA, covering a wide range of propellant sound speeds. The results of this study were first presented by Leege et al. [37], but are presented here with some modifications. Namely, the theoretical non-dimensional BTRA thrust will exclude the β parameter in Eq. (1.15). This is done because the theoretical model already normalizes thrust with the flow area as shown in Eq. (1.5). Including the volume void ratio erroneously accounts for the flow area an additional time, artificially reducing the theoretical non-dimensional thrust. The volume void ratio should only be used as a parameter defined for physical baffles, accounting for the actual machined dimensions. Thus, β should only be used in calculating the reference area for the non-dimensional thrust in experimental BTRA results or in obtaining dimensional results from the dimensionless thrust.

This test campaign was carried out using both the BTRA 500 and BTRA 100. Most experiments utilized a hybrid baffle configuration that included a short 0.25-meter-long BTRA 100 section followed by a 1.75-meter-long BTRA 500 section. This was done to lower the entrance Mach requirements while not significantly impacting the thrust performance. P300 projectiles were used in all tests.

The first propellant tested was methane and enriched-air, with results tabulated in Table 2.1. The propellant mixture used in this test series was $1CH_4 + 2O_2 + 4.67N_2$ with a sound speed of 350 m/s. The first set of tests swept a series of entrance Mach numbers, with a constant 21 atm fill pressure. These tests identified the minimum entrance Mach number for the hybrid BTRA 100/500 configuration around

Table 2.1 Methane and enriched-air propellant (1CH4 + 2O2 + 4.67N2) tests in the hybrid BTRA 100/500

Stage Configuration	Q	Pressure, atm	M_{in}	M_{avg}	I_{BTRA}	$I_{BTRA,theory}$	% Diff$_{I_{BTRA}}$
2m BTRA 100/500	10.46	21	1.86	1.81	-0.22	7.14	-
2m BTRA 100/500	10.41	21	1.91	2.07	0.94	7.66	-88%
2m BTRA 100/500	10.35	21	2.00	2.34	2.19	8.02	-73%
2m BTRA 100/500	10.31	21	2.20	2.50	2.12	8.16	-74%
2m BTRA 100/500	10.11	21	2.93	3.15	1.94	8.14	-76%
2m BTRA 100/500	10.34	25	1.99	2.40	2.37	8.08	-71%
2m BTRA 100/500	10.34	27	1.98	2.39	2.24	8.07	-72%
2m BTRA 100/500	10.33	28	1.99	2.43	2.24	8.11	-72%
4m BTRA 100/500	10.22	21	2.21	2.83	2.33	8.27	-72%
4m BTRA 100/500	10.17	28	2.22	2.98	2.12	8.24	-74%
4m BTRA 100/500	10.01	21	2.93	3.38	2.12	7.92	-73%
4m BTRA 100/500	10.00	28	2.93	3.42	1.64	7.87	-79%

Mach 2.0. It also showed that when a projectile transitions from one baffle design to another (even mid-stage), it must make that transition above the minimum required Mach number for both baffles, or a delayed unstart will be induced. This is apparently due to an instability that is introduced at the transition point that does not currently appear to be recoverable. A pressure scaling study was also conducted, showing the expected proportional thrust scaling with pressure from 21 to 28 atm. The final test series with the methane and enriched-air propellant was in a 4-m-long stage, demonstrating continuous BTRA operation for 4 m. The highest non-dimensional thrust achieved with this propellant was 2.37, about 71% lower than BTRA theory predicts.

The next propellant tested was methane and nitrous oxide due to its lower sound speed, about 310 m/s, enabling lower velocity operation. These results are tabulated in Table 2.2. Fill pressures were limited to 11 atm due to the relatively high peak pressures measured with this propellant. Successful propellants ranged from (2.25–2.5)CH4 + 4N2O, with 2.25CH4 being very near the heat release limit for the propellant. The highest non-dimensional thrust achieved with this propellant was 4.89, about 61% lower than BTRA theory predicts.

Table 2.2 Methane and nitrous oxide propellant tests in the hybrid BTRA 100/500

Stage Configuration	Propellant	Q	Pressure, atm	M_{in}	M_{avg}	I_{BTRA}	$I_{BTRA,theory}$	% Diff$_{I_{BTRA}}$
2m BTRA 100/500	2.50CH4 + 4N2O	9.40	11	2.26	2.60	3.75	11.42	-67%
2m BTRA 100/500	2.25CH4 + 4N2O	10.42	11	2.32	2.76	4.89	12.40	-61%
2m BTRA 100/500	2.50CH4 + 4N2O	9.28	11	3.34	3.52	2.72	12.42	-78%

The final propellant tested was hydrogen and air, a relatively high sound speed propellant, 400–500 m/s, that enables higher velocity operation. Hydrogen and air propellant results are tabulated in Table 2.3. All tests were conducted in the BTRA 500. Hydrogen and air propellants were operable in the range of (1–3)H2 + 0.5O2 + 1.88N2. A pressure scaling study was also completed. The thrust did not scale with pressure proportionally as expected, likely due to operating at heat releases much lower than the optimum. The highest non-dimensional thrust achieved with this propellant was 1.96, about 68% lower than BTRA theory predicts.

Table 2.3 Hydrogen and air propellant tests in the BTRA 500

Stage Configuration	Propellant	Q	Pressure, atm	M_{in}	M_{avg}	I_{BTRA}	$I_{BTRA,theory}$	% Diff$_{I_{BTRA}}$
2m BTRA 500	3H2 + 0.5O2 + 1.88N2	5.34	15	2.08	2.16	1.37	4.35	-69%
2m BTRA 500	2H2 + 0.5O2 + 1.88N2	6.53	15	2.22	2.29	1.12	5.10	-78%
2m BTRA 500	1H2 + 0.5O2 + 1.88N2	8.19	15	2.50	2.64	1.96	6.04	-68%
2m BTRA 500	3H2 + 0.5O2 + 1.88N2	5.34	25	2.06	2.16	1.07	4.35	-75%
2m BTRA 500	3H2 + 0.5O2 + 1.88N2	5.34	28	2.04	2.17	1.17	4.35	-73%

2.5 RTRA with Sweeper Baffles

A new ram accelerator configuration, called the RTRA with sweeper baffles, was developed and tested. This new ram accelerator concept had two primary design goals: to allow the RTRA to operate with more energetic propellants and to mitigate a potential instability occurring in the RTRA from the projectile-rail interaction. While the first goal was straightforward, matching the original purpose of the BTRA, the second goal was a bit more complicated. A natural instability has been theorized to be present in the RTRA. This instability is thought to arise from the projectile-rail interaction, where the small gap between the projectile and the rail surfaces will naturally lead to localized unstarts due to shock reflections

within the small gap. While these localized unstarts should not lead to immediate projectile unstarts, due to the larger volumes in the annular gaps between rails allowing pressure relief, they may be able to grow enough in strength to cause a full projectile unstart. This would only become more problematic at the higher Mach numbers that the RTRA would be expected to operate at. While this instability has not yet been experimentally observed, its existence is a logical assumption based on the natural differences in the flowfields between the SBRA and the RTRA.

The RTRA with sweeper baffles consists predominantly of an RTRA, where short sections of baffles are placed periodically throughout the tube, shown schematically in Fig. 2.11. These baffle sections would contain some small number of baffles, perhaps even one, and act to inhibit the forward motion of the combustion driven shock system. In this way, the RTRA with sweeper baffles achieves the same design benefit of the BTRA that allows the use of more energetic propellants, though likely with a reduced level of effectiveness. The baffles would also inhibit the motion and propagation of the localized unstart regions near the rails, delaying or preventing unstarts arising from the theorized instability. In this way, both the combustion driven shock system and the localized rail unstart regions are 'swept' back by the baffles, allowing for continued or extended operation in the rail sections. This design differs from a traditional BTRA with longer baffle chambers by the distinction that the periodic spacing between baffle sections, that is, the length of the rail sections, is longer than the projectile shoulder, meaning this design does

Fig. 2.11 Schematic of the RTRA with sweeper baffles.

not take advantage of the one-way-valve behaviour of a BTRA (except in the baffle sections). It would be expected that the sweeper baffle sections would cause drag and reduce performance compared to an RTRA, however, in an optimized design this would be offset by the higher thrust with more energetic propellants, while having an expanded operating range.

The RTRA with sweeper baffle configuration was tested utilizing existing RTRA 200 and BTRA 500 hardware. The experiment setup consisted of a two-meter-long BTRA 500 starting stage, followed by a two-meter-long RTRA 200 stage that was bisected with a five-baffle-long BTRA 500 sweeper baffle section. The starter stage was used to establish ram acceleration and provide relatively consistent inlet conditions to the RTRA with sweeper baffle stage. The starter stage was filled with a methane and enriched-air propellant (1CH4 + 2O2 + 4.67N2). The RTRA with sweeper baffle stage was filled with a methane and air propellant (ϕCH4 + 2O2 + 7.52N2), which was used in the initial RTRA 200 validation experiments.

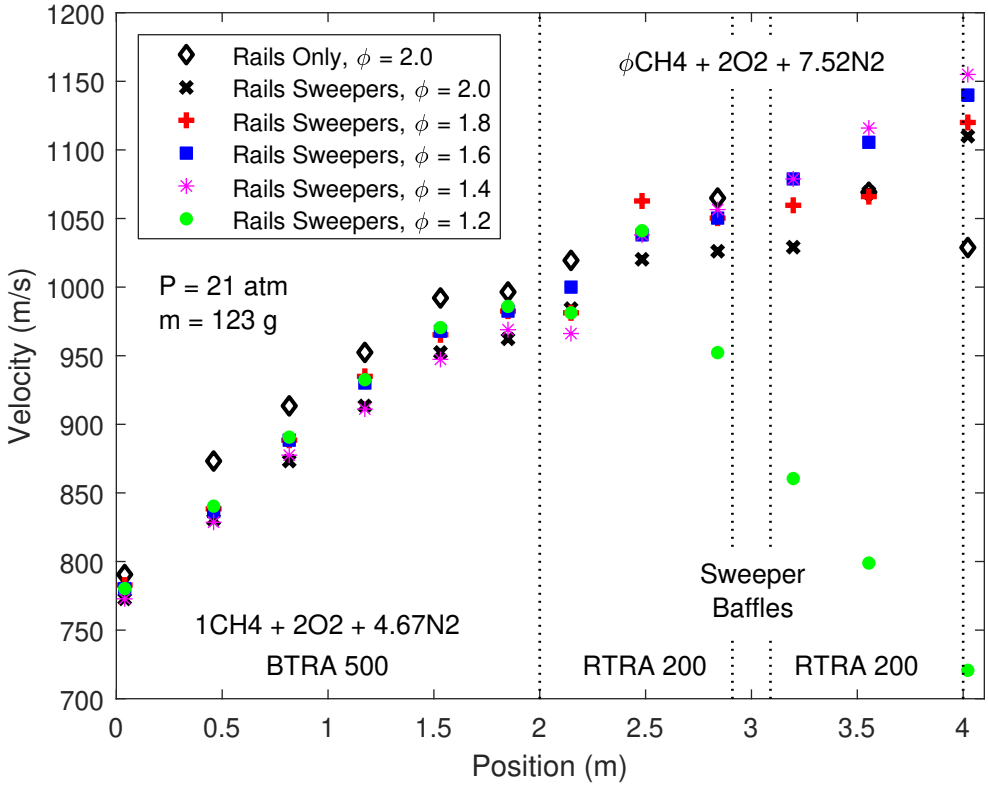

Fig. 2.12 Experimental velocity versus position curves for the RTRA with sweeper baffles and varying propellant mixtures.

All experiments were carried out at 21 atm with P300 projectiles. The velocity versus position plots are shown in Fig. 2.12. As discussed in Section 2.3, $\phi = 2.2$ was required for continuous operation in the RTRA 200 at 21 atm and above. An experiment where $\phi = 2.0$ is shown in Fig. 2.12 for comparison, where an unstart occurred just before the RTRA exit (represented by a sharp drop in velocity). To validate the sweeper baffle concept, the same experiment was repeated, with the sweeper baffles at the center of the RTRA stage. This test resulted in a clean run-out, where the projectile left the stage without an unstart, accelerating throughout. This run-out provided initial evidence that the sweeper baffles are able to delay or prevent an unstart in an otherwise too energetic propellant. Additional tests were conducted with further increasing heat releases until an unstart finally occurred before the sweeper baffles at $\phi = 1.2$. However, in theory, even this unstart could be prevented if the sweeper baffle section were moved upstream of the unstart.

Table 2.4 shows the non-dimensional heat release, non-dimensional thrust, theoretical RTRA non-dimensional thrust, percent difference between actual and theoretical non-dimensional thrust, and the ballistic efficiency (BE) for each of the RTRA with sweeper baffle tests, including the RTRA 200 $\phi = 2.0$ and $\phi = 2.2$ reference cases. Without sweeper baffles, the RTRA 200 required a non-dimensional heat release of 4.59 or lower, while the sweeper baffles could accommodate non-dimensional heat releases up to 6.75, a 47% increase. As expected, the inclusion of the five-baffle-long sweeper section reduced the non-dimensional thrust and ballistic efficiency of the RTRA, however, as the propellant heat release approached its limit, the thrust and efficiency approached the RTRA 200 values at $\phi = 2.2$.

Table 2.4 RTRA with sweeper baffle experimental results

Stage Configuration	Propellant	Q	I	$I_{\text{RTRA,theory}}$	% Diff$_{I_{\text{RTRA}}}$	BE
2m BTRA 500 + 2m RTRA 200	2.2CH4 + 2O2 + 7.52N2	4.59	3.68	4.49	-18%	9.3%
2m BTRA 500 + 2m RTRA 200	2.0CH4 + 2O2 + 7.52N2	5.08	-0.31	4.88	-	-
2m BTRA 500 + 2m RTRA w/ Sweeper Baffles	2.0CH4 + 2O2 + 7.52N2	5.08	2.04	4.89	-58%	5.8%
2m BTRA 500 + 2m RTRA w/ Sweeper Baffles	1.8CH4 + 2O2 + 7.52N2	5.60	2.38	5.26	-55%	6.2%
2m BTRA 500 + 2m RTRA w/ Sweeper Baffles	1.6CH4 + 2O2 + 7.52N2	6.16	2.67	5.57	-52%	7.7%
2m BTRA 500 + 2m RTRA w/ Sweeper Baffles	1.4CH4 + 2O2 + 7.52N2	6.75	3.02	5.92	-49%	8.6%
2m BTRA 500 + 2m RTRA w/ Sweeper Baffles	1.2CH4 + 2O2 + 7.52N2	7.41	-4.40	6.35	-	-

2.6 Baffled Start Stage

A new ram accelerator configuration, called the baffled start stage (BSS), was developed and tested. The BSS was a proposed solution for the elimination of the obturator normally required for ram accelerator operation. As discussed in Section 1.4.1, the obturator has two primary roles in the ram accelerator. First, it fully occludes the launch tube, preventing gun gas from blowing past the projectile in the initial launcher. Second, the obturator aids in the starting process of the ram accelerator where it acts as a piston, generating a region of high pressure and temperature behind the projectile and accelerating the gas along with the projectile. However, in most applications, it is undesirable to have a secondary object traveling down the tube behind the projectile. This is especially problematic within the ram accelerator where there is a high pressure combustion region behind the projectile but ahead of the obturator, and it can cause the obturator to come to a stop mid-tube. This can be a problem during system recycles, especially when intending to fire multiple times in quick succession.

The BSS consists of a short baffled tube section filled with a carefully tuned propellant and a full-bore projectile, serving as a ram accelerator starting stage that sits before the first ram stage in a system. A schematic of a BSS preceding an RTRA stage is shown in Fig. 2.13. The full-bore projectile fulfills the first role of an obturator by occluding the launch tube and preventing gun gas blowby. If a full-bore projectile is undesirable for the primary ram stages, as sub-caliber projectiles have been shown to improve performance [25], the launch system and BSS can simply be sized to a smaller tube diameter so that the full-bore projectile becomes sub-caliber in the primary ram stage. To cover the second role of obturators, the BSS takes advantage of the more energetic propellants operable in a BTRA to ensure ignition occurs reliably and the combustion quickly catches up to the projectile in the absence of an obturator. While the ram ignition process is well studied experimentally and operable starting conditions have been identified [18], the exact ignition mechanism is still currently unknown. In operation with an obturator, the large pressures and temperatures caused by the piston-like compression are thought to ignite the propellant and accelerate it along with the projectile. However, it has also been shown through

Fig. 2.13 Schematic of a BSS preceding an RTRA stage.

direct imaging, that large temperature spikes do occur at the end of the launch tube near the ram tube entrance [38]. This is due to the compression of the residual gas in the launch tube, which is typically at a rough vacuum, between the projectile and the diaphragm at the entrance to the ram stage. This large spike in temperature occurs just when the projectile enters the ram stage and should be sufficient to ignite the propellant. The full-bore projectile in the BSS should accommodate either ignition mechanism, while the baffles should help prevent immediate unstarts from occurring, allowing combustion to proceed in the baffle chambers alongside the projectile instead of being forced ahead of it. The resulting configuration is a short stage, about two projectile lengths or less, that can start the ram combustion cycle, allowing a projectile to transfer into any other ram stage (BTRA or RTRA) and experience nominal operation thereafter.

The BSS configuration was tested using BTRA 500 hardware. All tests were conducted in a 4-m-long BTRA 500 stage, where the first 10 baffles (0.36 m) were separated from the remainder via diaphragms to act as the BSS. The P496-2BL (full-bore) projectile was used in all experiments along with methane and nitrous oxide propellant ($\phi CH_4 + 4N_2O$) at 11 atm. The initial experiments were focused on finding an appropriate propellant mixture, defined here by the equivalence ratio ϕ, that could facilitate a ram start. Since identifying a working propellant was the primary goal here, the BSS was not staged separately from the remaining section of baffles and a continuous 4-m-long BTRA 500 stage was used. The entrance

velocity was held constant around 1000 m/s (Mach 3.1). Velocity versus position data for these experiments are shown in Fig. 2.14. The $\phi = 3.5$ ($Q = 6.34$) propellant was not energetic enough, experiencing supersonic drag throughout the 4-m stage. However, the velocity fluctuations in the later half of the tube are too significant to be errors with the instrumentation and may be at locations where combustion momentarily caught up with the projectile, pushing it forward. If that was the case, the $\phi = 3.5$ propellant would be very near the minimum heat release limit for starting. The next test moved to a more energetic propellant, $\phi = 3.0$ ($Q = 7.61$), and resulted in an immediate unstart, with rapid deceleration throughout the tube. This unstart bounded the range of viable propellants between $\phi = 3.5$ and $\phi = 3.0$ ($6.34 < Q < 7.61$). Splitting the range, the $\phi = 3.25$ ($Q = 6.98$) propellant was able to produce a ram start, though with a significant delay, only starting near the 1.2 m mark. In this shot, the propellant ignited immediately in the BSS and the combustion lagged behind the projectile, providing no thrust. This is evident because the projectile experiences supersonic drag up until 1.2 m, where the combustion finally caught up to the projectile and

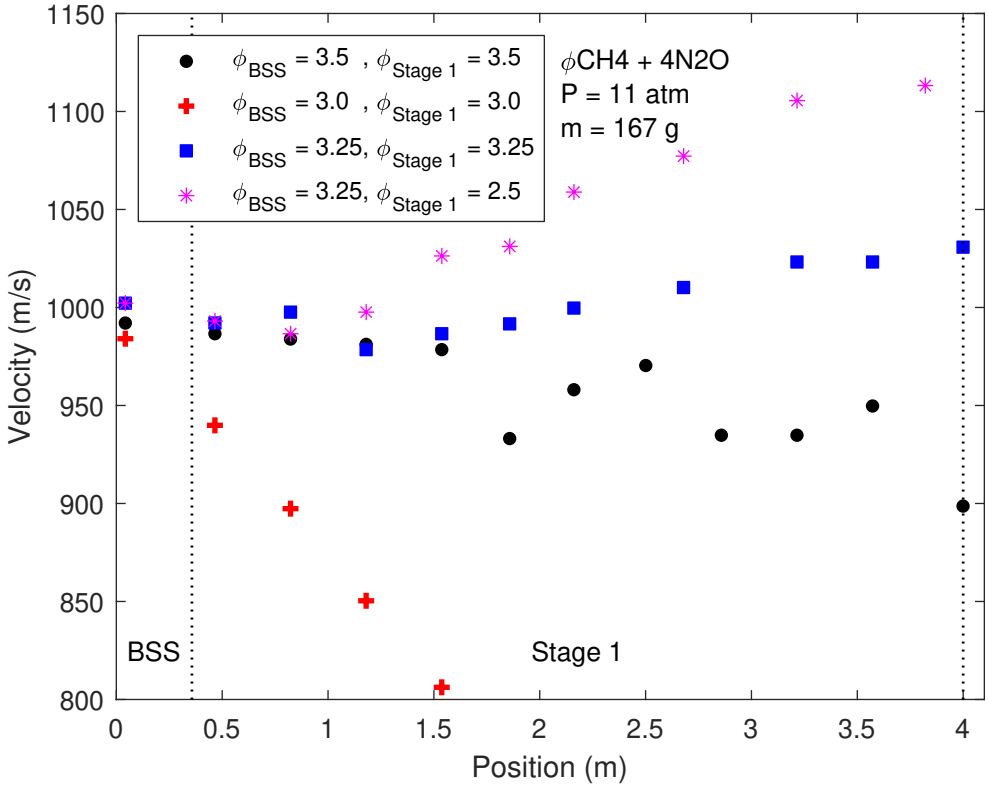

Fig. 2.14 Velocity versus position data for BSS propellant experiments.

ram acceleration began. This was further confirmed by the subsequent experiment where the BSS was separated from the first ram stage via diaphragms and a more energetic propellant was used in stage one. The $\phi = 2.5$ propellant was chosen for stage one as it fits within the range of viable propellants for nominal ram operation, as presented in Section 2.4. The more energetic propellant in stage one reduced the start delay to 0.8 m, with no change to the BSS itself.

Additional tests were carried out with the BSS to more fully characterize its operation. Figure 2.15 shows a couple experiments that significantly lowered the entrance velocity to the BSS. By lowering the entrance velocity from 1000 m/s to 700 m/s (Mach 3.1 to Mach 2.2), the start delay was increased from 0.8 m to 1.8 m. Since the propellant was unchanged, this suggests that the entrance velocity (or Mach number) plays a significant role in the kinetics and dynamics of the travelling combustion wave, as at lower velocities it takes longer to catch up to the projectile. The next test went to an even more energetic propellant in stage one, $\phi = 2.25$, which was at the heat release limit for the methane and nitrous oxide

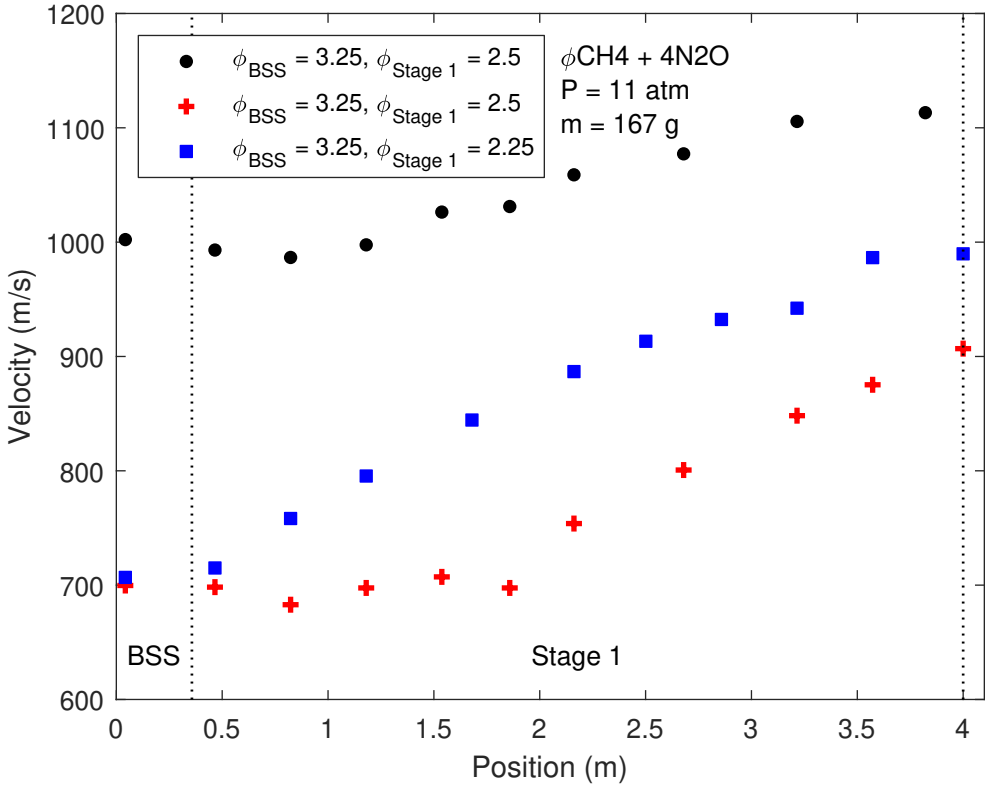

Fig. 2.15 Velocity versus position data for BSS velocity experiments.

propellants discussed in Section 2.4. The more energetic stage one propellant completely eliminated the start delay as ram acceleration began immediately after the projectile exited the BSS.

A final test was conducted to determine the effect of a pressure differential between the BSS and the first stage. This test kept the 11 atm fill pressure in the BSS, but increased the fill pressure in stage one to 14 atm. This test is shown in Fig. 2.16 along with the prior test case that had no start delay. The pressure increase introduced a start delay at around 0.8 m. This suggests that an ideal BSS should contain propellant at the same pressure as the first ram stage so no start delays are incurred.

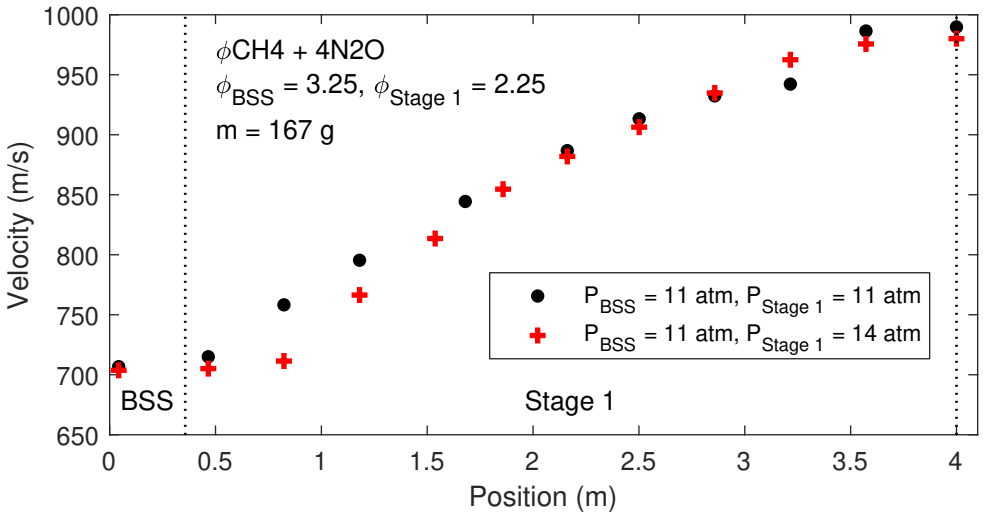

Fig. 2.16 Velocity versus position data for BSS pressure experiments.

2.7 Discussion

The BTRA 500 experiments and their comparison to prior BTRA 100 experiments led to a couple of key conclusions on BTRA operation. First, smaller baffle chamber diameters lead to higher thrust and more efficient ram operation. This is clearly shown in the non-dimensional thrust and ballistic efficiency comparisons in Fig. 2.7. Second, larger baffle chamber diameters lead to an expanded operational envelope, specifically enabling operation at lower Mach numbers. This is shown in the start and unstart data for the BTRA 500 and BTRA 100 in Fig. 2.8.

The higher thrust and more efficient operation in smaller baffle chambers leads to the logical extrapolation to the minimum sized baffle chamber, a smooth bore (or railed tube), producing the maximum possible thrust and efficiency. However, there will exist a trade-off as smaller diameter baffle chambers will require lower heat release propellants to operate, lowering their thrust potential. This is evident due to the large gap in allowable propellant heat releases that has been demonstrated between the BTRA and the RTRA. That said, there has been no significant difference between operable propellant heat releases found between the BTRA 500 and the BTRA 100, despite their differences in baffle chamber diameter. This suggests that rather than a gradual change in operable propellant heat releases with changing baffle chamber diameters, there may be certain thresholds of baffle chamber diameters that require significant jumps in propellant heat releases to maintain operation. Alternatively, there may simply be a certain range of baffle chamber diameters, near the small end, where operable propellant heat releases are highly sensitive to the chamber diameter, with lower sensitivity at larger diameters. Regardless, it is evident that more experiments with BTRAs of varying baffle chamber diameters will be required to confirm this nature and find the optimal baffle design and propellant combination to maximize performance.

Another insight from the BTRA testing is a better understanding of the role of the volume void ratio, β, in the calculation of theoretical non-dimensional thrusts for the BTRA. This was briefly discussed at the start of Section 2.4 but it merits further discussion in a broader context. As previously discussed, β should not be used to further modify the non-dimensional thrusts calculated in Eq. (1.15), as the thrust is already normalized by the flow area. Instead, β should only be used as a parameter defined for actual BTRA hardware that quantifies the relative volume taken up by the baffles, rails, or other geometric features that are part of the design. In practice, β, once calculated for a particular baffle design, should be used as a convenient means of calculating the reference flow area used in converting experimental thrust results into non-dimensional form for comparisons to theory or other experiments. In addition, β can be defined for RTRAs, where it simply accounts for the volume taken up by the rails and other geometric features in the absence of baffles. All of the above arguments on the appropriate use of β for BTRAs apply to RTRAs as well.

One outcome of this new insight on the β parameter is that all BTRAs have the same theoretical non-dimensional thrust for a given propellant and Mach number, as it is no longer adjusted by β. This is now consistent with both SBRA and RTRA non-dimensional thrust calculations.

The new insight on the use of the β parameter, when considered alongside the non-dimensional thrust results of the BTRAs, the RTRA 200, and the theory in Fig. 2.9a, leads to a better understanding of the large difference between actual performance and theory predictions for the BTRA. Logically, the causes for this discrepancy could be due to some combination of baffle drag and combustion efficiency, that is, how much combustion occurs in close proximity to the projectile so that its energy can be transferred to the projectile efficiently. Since both the BTRA 100 and BTRA 500 non-dimensional thrusts are to be compared to the same theory curve, it is clear that the smaller baffle chamber diameter leads to better agreement with theory. While the baffle drag should decrease with decreasing baffle chamber diameter, allowing the experimental performance to approach the theoretical prediction more closely, the drag models discussed in Section 1.4.2 and shown in Fig. 1.16 do not account for the sizable difference. While the baffle drag models may not be particularly accurate, there is good reason to believe that combustion efficiency is a more significant factor. In a BTRA CFD study by Daneshvaran and Knowlen [26], it was shown that pockets of unreacted propellants can remain near the outer walls of the baffle chambers multiple projectile lengths behind the projectile. An image showing the temperature contours from one such simulation in a normal baffle is shown in Fig. 2.17, case 3. This simulation used a methane

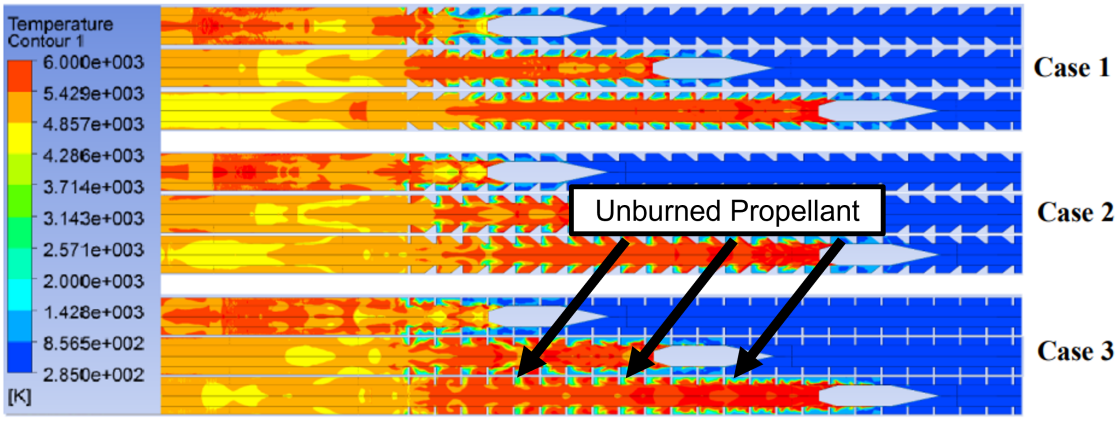

Fig. 2.17 Static temperature contours from BTRA reactive flow CFD simulations [26].

and oxygen propellant ($1CH_4 + 2O_2$), which is significantly more energetic than the propellants used in the experiments herein, thus suggesting that there is a sizable fraction of propellant that is burning far behind the projectile, where it may never transfer its energy to the projectile. If one assumes that this combustion inefficiency is primarily responsible for the severe underperforming of BTRA experiments when compared to theory, it explains why the smaller baffle chamber diameters perform better. It would be expected that larger baffle chamber diameters would lead to larger pockets of unburned propellant surviving longer, causing significant drops in combustion efficiency. If a baffle and/or projectile design can encourage more rapid and complete combustion within baffle chambers, BTRA performance may start to approach the theoretically predicted levels, surpassing the RTRA/SBRA as originally intended.

While the BTRA 100 and BTRA 500 work well at reducing the minimum required Mach number for ram operation, the RTRA 200 is a high performing and relatively efficient ram configuration for use with axisymmetric projectiles. As shown in Fig. 2.9, the non-dimensional thrust and ballistic efficiency of the RTRA 200 is significantly higher than either BTRA. That said, the RTRA 200 requires a much higher Mach number to operate, as shown in Fig. 2.10.

The BTRA propellant study found viable propellants having low, moderate, and high sound speeds to enable ram acceleration at low, moderate, and high velocities. Methane and enriched-air propellant, $1CH_4 + 2O_2 + 4.67N_2$ ($Q \approx 10.3$) was found to be a very robust propellant with moderate sound speed (350 m/s). It achieved non-dimensional thrusts up to 2.37, about 71% lower than theory predicts. This propellant was also shown to scale well with pressure up to at least 28 atm. Methane and nitrous oxide was found to be a high performing propellant with relatively low sound speed (310 m/s). Successful propellants ranged from $(2.25–2.5)CH_4 + 4N_2O$ ($9.3 < Q < 10.4$) and non-dimensional thrusts went as high as 4.89, about 61% lower than theory predicts. Finally, hydrogen and air proved to be a viable propellant with relatively high sound speed (400–500 m/s). Operable propellants were in the range of $(1–3)H_2 + 0.5O_2 + 1.88N_2$ ($5.3 < Q < 8.2$) and the highest non-dimensional thrust achieved was 1.96, about 68% lower than theory predicts. Notably, more energetic hydrogen propellants, utilizing enriched-air, may be operable but have not yet been tested. Methane and enriched-air has been the most well tested propellant in the BTRA to

date and is operable over a wide range of velocities. However, this propellant study has shown that other propellants can be successfully used to expand the velocity limits of the BTRA. Additionally, diluents with high or low sound speeds could be added to any of these propellants to further modify their sound speeds, and push the velocity limits of the BTRA even further.

As discussed in Section 2.5, the RTRA with sweeper baffles is a new ram accelerator configuration designed to enable the use of more energetic propellants in an RTRA and to mitigate a theorized, inherent instability in RTRA systems. The proof of concept experimental series, whose results are shown in Fig. 2.12 and summarized in Table 2.4, validated this new configuration. The experimental configuration of the RTRA with sweeper baffles allowed a nearly 50% increase in propellant heat release. While these proof of concept tests achieved their goals even better than anticipated, the non-dimensional thrust and ballistic efficiency achieved by even the most energetic propellant fell short of those achieved by the nominal propellant in the RTRA without sweeper baffles. Additionally, the percent difference from theory predictions was typically around 50%, much closer to the typical differences in baffles rather than rails. This highlights the trade-offs of the RTRA with sweeper baffle concept. In order to operate with more energetic propellants and prevent or delay unstarts in the RTRA, baffles can be introduced, along with their associated reductions in thrust and efficiency. However, it is important to note that these results represent just one configuration of the RTRA with sweeper baffle concept. The number of sweeper baffles and their periodic spacing throughout the RTRA can be further optimized. Given the increasing performance demonstrated with increasing propellant heat releases in the initial tests, even a slightly more optimized configuration should allow the use of even more energetic propellants with even less drag induced from the sweeper baffles. This is an area where a comprehensive experimental test program would be of great interest. Experimentally determining the optimum number of baffles per sweeper section and their spacing throughout the tube, including how these scale with Mach number, will be of critical importance for developing a high performance design that should far exceed the thrust and efficiency capabilities of both the BTRA and RTRA.

The BSS was shown to be an effective tool for operating a ram accelerator without the use of an obturator. This is a significant advancement that will prove essential for a large number of applications that cannot accommodate secondary bodies travelling down tube, most notably are any applications that would operate with rapid firing cadences. This is primarily due to the elimination of any concerns over the obturator getting stuck in the ram tube, especially in baffles.

Several important insights were learned from the initial BSS experiments. First, the BSS requires a relatively low energy propellant to start the ram accelerator. The BSS used a $Q = 7.0$ propellant, about 25% lower than propellants used in a normal stage with the same baffles where Q is between 9.3 and 10.4. Additionally, it is a relatively narrow band of propellant heat releases that can achieve the obturator-less start. In essence, the propellant must be sufficiently energetic to ignite and have the combustion catch up to the projectile, but not so energetic as to ignite and immediately overtake the projectile. Second, a ram start delay can be incurred in the first ram stage if non-optimal propellants are used. That is, when a propellant that is near the heat release limit for the stage is used, the ram starts immediately upon stage entry. If less energetic propellants are used, the projectile may drift into the tube for some distance until the combustion catches up and the projectile starts accelerating. These starting delays can also be reduced or eliminated by raising the entrance Mach number of the projectile. Finally, the fill pressure in the BSS should match the fill pressure of the first ram stage, or else a start delay may be incurred.

Another remarkable lesson from the BSS experiments is confirmation that the ram starting transients are very short lived. This is evident from the nature of BSS operation. The projectile enters the BSS and the propellant is ignited but combustion lags behind the projectile, producing no thrust in the BSS. As shown in Figs. 2.14 and 2.15, the projectile will continue to drift through the first stage until the combustion catches up and the projectile starts accelerating. When the first stage propellant is sufficiently energetic, acceleration occurs immediately upon entrance, meaning the combustion immediately catches up to the projectile and a stable ram flowfield is established. In all cases, regardless of any start delays, once ram acceleration began, performance was nominal, bearing no apparent effects from the starting process.

The BSS still remains to be optimized in its length. The BSS used in the initial testing was just under two projectile lengths long due to hardware constraints. However, due to the rapid starting capabilities achieved with the configuration and the nature of its operation, it can likely be significantly shortened. Since the role of the BSS was found to be in facilitating propellant ignition while preventing immediate unstarts, it can likely be shortened to about one projectile length, perhaps even shorter. Further testing will be needed to determine the minimum BSS length.

Chapter 3

Modeling

The modeling goals of this work focused around the development of a new computational model for the ram accelerator. This model was developed to be robust in its ability to model the SBRA, RTRA, and the BTRA, specifically including new methods to account for the effect of baffles on ram acceleration. The BTRA modeling was of keen interest due to the noted discrepancies between experiments and existing theory (see Fig. 2.7) and the obvious shortcomings of prior baffle drag models (discussed in Section 1.4.2). In this chapter, the newly developed one-dimensional ram accelerator model will be detailed, its results will be compared to both prior models and experimental results, and new physical understandings from the model will be presented. This chapter concludes with a summary discussion of the significant outcomes and lessons from the new model as well as outstanding questions and further avenues for development.

3.1 Ram Accelerator PFR Model

The new ram accelerator model was developed to consider any ram accelerator configuration operating in the thermally choked operating mode. The prior control volume model, discussed in Sections 1.3.1 and 1.3.2, worked well for SBRA operation with great experimental agreement (see Fig. 1.6). However, this modeling method fell short when applied to the BTRA, as discussed in Chapter 2. The baffle drag models discussed in Section 1.4.2 were unable to accurately account for the effects of baffles, notably predicting zero drag

at the point of peak thrust. While CFD is a natural solution to this modeling problem, as discussed in Section 1.5, CFD modeling of the ram accelerator is a difficult task that has not yet obtained the accuracy required to influence BTRA designs and developments. Additionally, ram accelerator CFD simulations are far too computationally intensive to be used for parametric design studies without significant time and cost requirements. Thus, a middle ground was proposed which is presented here.

The new ram accelerator model took a quasi-one-dimensional (1D) approach, instead of the 'black box' control volume approach of the general ram accelerator model, resolving a 1D flowfield around the ram projectile. This approach was significantly influenced by the prior work by Sasoh and Knowlen [39], where a similar model was developed that resolved the flowfield around the projectile in a quasi-1D manner. However, this new model goes beyond the Sasoh model in a few key areas. First, the new model accounts for the geometry of baffles and rails, instead of considering only smooth bore operation. Second, the projectile geometry is considered in full, allowing for realistic design features such as the truncated projectile bases used in all experimental projectiles (instead of the symmetric biconical projectiles used by Sasoh). Third, the effects of the non-inertial, accelerating projectile reference frame are included. Finally, a different chemical kinetic model is applied, resolving the combustion with increased fidelity.

The new ram accelerator model got its namesake, the ram accelerator PFR model, from the modeling framework used: the plug flow reactor (PFR). A PFR is a quasi-1D model that considers transverse slices through the computational domain, dividing it into discrete sections, or plugs, that feature unidirectional reactive flow. In this manner, a PFR can compute the flow changes from one end of the computational domain to the other, sequentially, one plug at a time. In the ram PFR model, the entire computational domain is discretized into cells in which the PFR model is applied. Thus, each computational cell, or PFR, is linked together in sequence to form a chemical reactor network (CRN) describing the whole ram flowfield. The ram PFR is a modified version of the PFR model laid out by Turns [40]. The basic model assumptions are as follows:

- The flow is steady.
- There is no axial mixing.
- The gas in each cell is perfectly mixed.
- The flow is one-dimensional.

- The flow is frictionless.
- The flow exhibits ideal-gas behavior.

Additionally, while the flow is considered steady, to simplify the computation by excluding all time dependent terms, the effects of the non-inertial reference frame are optionally included in the model. This accounts for the acceleration of the projectile reference frame in which the computations are done. This inertial correction was included so that Newton's laws could be applied in the model with more rigorous accuracy. The other major departure from the standard PFR model is the addition of the projectile and the force it exerts on the surrounding flow.

Ram PFR Model Structure

The ram PFR computational model was implemented using MATLAB software [41]. The computational domain is constructed using the combination of user defined projectile and tube dimensions, starting just before the projectile nose cone tip and ending some distance behind the projectile to ensure combustion completes within. An example of one such domain for the P300 in a BTRA 500 is shown in Fig. 3.1, including enlarged computational cells for clarity. Once the computational domain boundaries are defined, it is divided into computational cells. The nominal length of each computational cell is set based on which section of the domain it resides in: the nose cone, shoulder, tail cone, or aft. Each cell is further shortened in length when near a geometric feature, such as baffle wall edges or projectile section changes, so that exact geometry changes are captured. Finally, the cells are further refined in close proximity to the thermally choked plane, where the reaction rates are significant. This refinement occurs when 5% of the oxidizer has been consumed. This ensures the reaction is modeled with high accuracy and the thermally choked plane is accurately identified. A cell refinement study was completed to determine the nominal cell sizes for

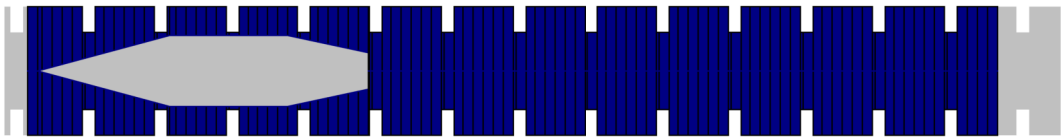

Fig. 3.1 Ram PFR example computational domain for the P300 projectile in the BTRA 500 (computational cells are enlarged for visibility).

each section as well as the combustion cell refinements required to produce converged solutions. These cell size refinements are tabulated in Table 3.1. The tail cone and aft sections required smaller cell sizes to calculate more accurate normal shock locations and chemical reactions.

Table 3.1 Ram PFR model cell size refinement results

Cell Location	Nominal Cell Length, mm
Nose Cone	0.5
Shoulder	0.5
Tail Cone	0.1
Aft	0.1
Combustion Zone Cell Divisions	30

The ram PFR model used the GRI-Mech 3.0 combustion mechanism along with Cantera software for the combustion reaction modeling [12, 13]. The GRI-Mech 3.0 combustion mechanism was used due to its well demonstrated accuracy and capabilities, as well as to handle the wide array of propellants that are often used in the ram accelerator. While reduced chemical kinetics mechanisms have been developed for the ram accelerator, they were not used in the present study due to their propellant limitations [42]. That said, reduced kinetics mechanisms could be used in the future to reduce the computation time for the model if desired. Additionally, future studies may look into the effects of combustion mechanism choice on the PFR model output, but that is beyond the scope of the present study.

The ram accelerator PFR model consists of four different models, which will be detailed in the following sections. The primary model that is used in every computational cell is the ram PFR model, where the overall model gets its name. This model calculates the changes in all flow parameters across the length of each cell and is detailed in Section 3.1.1. At a predefined location on the projectile tail cone, a normal shock will occur. This location is determined via the convergence algorithm discussed in Section 3.1.5. A separate normal shock model is applied at this location, using the PFR model output from the cell as an input, effectively putting the normal shock at the aft end of the cell. This model is detailed in Section 3.1.2. At the projectile base, a separate model is used to account for the rapid area expansion. This model is applied before the PFR model in the cell and is detailed in Section 3.1.3. Finally, all baffle walls throughout

the domain are handled via a separate model that accounts for the cumulative effect of a baffle wall only at each aft baffle wall edge. This model is applied before the PFR model in each cell that is adjacent to an aftward facing baffle wall edge and is detailed in Section 3.1.4. The unique solution for each set of input conditions is determined by satisfying the thermally choked operating condition, which is detailed in Section 3.1.5. Selected MATLAB codes for the ram accelerator PFR model can be found in the Appendix.

3.1.1 Ram PFR Model

As discussed above, the ram PFR model is a modified version of a typical PFR model suited for the ram accelerator. It follows all of the assumptions discussed above for the overall model. The model is developed by applying the conservation laws to each computational cell in the domain.

First, the conservation of mass is applied to the control volume as shown in Fig. 3.2a. Writing out the steady conservation of mass where the mass flow into the control volume equals the mass flow out yields

$$\rho u A = \left(\rho + \frac{d\rho}{dz}\Delta z\right)\left(u + \frac{du}{dz}\Delta z\right)\left(A + \frac{dA}{dz}\Delta z\right) . \tag{3.1}$$

Rearranging and simplifying Eq. (3.1), where higher order Δz terms are ignored, the final expression for the conservation of mass can be written as

$$\frac{1}{\rho}\frac{d\rho}{dz} + \frac{1}{u}\frac{du}{dz} + \frac{1}{A}\frac{dA}{dz} = 0 . \tag{3.2}$$

Next, the conservation of momentum is applied to the control volume as shown in Fig. 3.2b. Here, it is important to note that the direction of projectile acceleration is in the negative direction. This means that the inertial force from the accelerating frame of reference acts in the positive direction. Additionally, the force of the projectile on the control volume is defined in the positive direction so that positive values represent thrust, while negative values represent drag. Writing out the steady conservation of momentum,

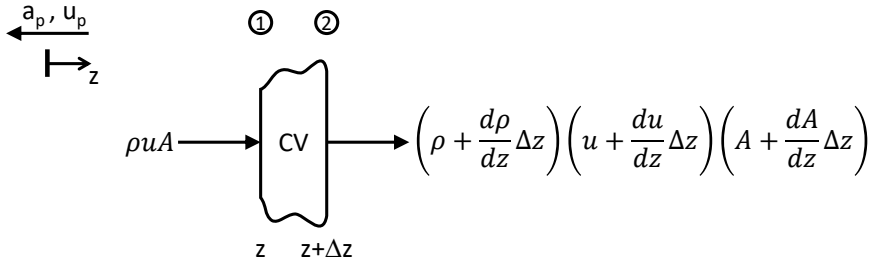

(a)

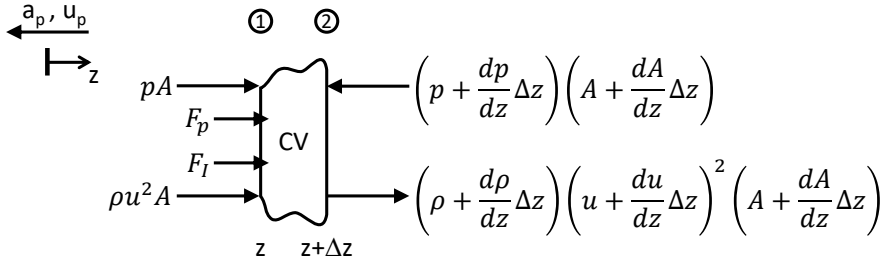

(b)

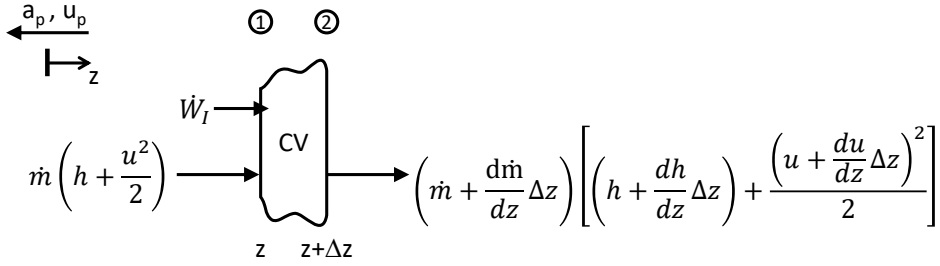

(c)

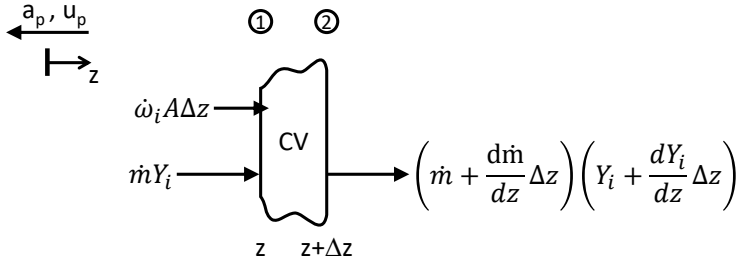

(d)

Fig. 3.2 Conservation of mass (a), momentum (b), energy (c), and species (d) for the ram PFR model control volume.

where the sum of the forces on the control volume equals the change in the momentum, yields

$$pA - \left(p + \frac{dp}{dz}\Delta z\right)\left(A + \frac{dA}{dz}\Delta z\right) + F_p + F_I = \left(\rho + \frac{d\rho}{dz}\Delta z\right)\left(u + \frac{du}{dz}\Delta z\right)^2\left(A + \frac{dA}{dz}\Delta z\right) - \rho u^2 A\,. \tag{3.3}$$

The force of the projectile on the control volume is defined as the average pressure multiplied by the area differential across the control volume. The area differential is chosen so that positive force values represent thrust. This relation is written as

$$F_p = p_{avg}(A_2 - A_1) = \frac{p + \left(p + \frac{dp}{dz}\Delta z\right)}{2}\left[\left(A + \frac{dA}{dz}\Delta z\right) - A\right], \tag{3.4}$$

which is further simplified by eliminating higher order Δz terms, yielding

$$F_p = p\frac{dA}{dz}\Delta z\,. \tag{3.5}$$

The inertial force is written as

$$F_I = C_I \int_{CV} \rho a_p dV \approx C_I \rho_{avg} a_p V_{CV}\,, \tag{3.6}$$

where the inertial force coefficient, C_I, is a Boolean toggle for optionally including the term. The volume of the control volume is calculated using the cylindrical volume of the cell and subtracting the projectile volume, generally modeled as a frustum, yielding

$$V_{CV} = A_{cyl}\Delta z - \frac{\Delta z}{3}\left(2A_{cyl} - A_1 - A_2 + \sqrt{(A_{cyl} - A_1)(A_{cyl} - A_2)}\right). \tag{3.7}$$

The common Δz terms can be factored out, leaving an alternative expression for the volume of the control volume

$$V_{CV} = A^*_{CV}\Delta z\,, \tag{3.8}$$

where the effective cross-sectional area of the control volume is defined as

$$A^*_{CV} = A_{cyl} - \frac{1}{3}\left(2A_{cyl} - A_1 - A_2 + \sqrt{(A_{cyl} - A_1)(A_{cyl} - A_2)}\right) . \tag{3.9}$$

The average density can be written as

$$\rho_{avg} = \frac{\rho + \left(\rho + \frac{d\rho}{dz}\Delta z\right)}{2} . \tag{3.10}$$

By substituting Eqs. (3.8)–(3.10) into Eq. (3.6) and eliminating higher order Δz terms, the inertial force can be rewritten as

$$F_I = C_I \rho a_p A^*_{CV} \Delta z . \tag{3.11}$$

Finally, by substituting Eqs. (3.5) and (3.11) into Eq. (3.3), the conservation of momentum can be rewritten as

$$\rho u \frac{du}{dz} + \frac{dp}{dz} - C_I \rho a_p \frac{A^*_{CV}}{A} = 0 . \tag{3.12}$$

Next, the conservation of energy is applied to the control volume as shown in Fig. 3.2c. Note, the heat release due to combustion is integrated into the enthalpy terms and not shown here explicitly. The relation between enthalpy and chemistry will be defined later. Aside from the chemical reaction, the only other energy input or output of the system is the inertial work done on the system due to the accelerating reference frame. Thus, the conservation of energy, where the rate of change in energy of the system is equal to the net power input, can be written as

$$\left(\dot{m} + \frac{d\dot{m}}{dz}\Delta z\right)\left[\left(h + \frac{dh}{dz}\Delta z\right) + \frac{1}{2}\left(u + \frac{du}{dz}\Delta z\right)^2\right] - \dot{m}\left(h + \frac{u^2}{2}\right) = \dot{W}_I . \tag{3.13}$$

Recognizing that the mass flow rate is constant due to the steady flow assumption, the $\frac{d\dot{m}}{dz}$ term can be eliminated. The inertial power input is generated due to the inertial force acting on the control volume at

the projectile velocity, and can be written as

$$\dot{W}_I = F_I u_p = C_I \rho a_p A^*_{CV} u_p \Delta z \,. \tag{3.14}$$

Substituting Eq. (3.14) into Eq. (3.13) and eliminating higher order Δz terms, the conservation of energy can be rewritten as

$$\frac{dh}{dz} + u\frac{du}{dz} - \frac{C_I \rho a_p u_p A^*_{CV}}{\dot{m}} = 0 \,. \tag{3.15}$$

Finally, the conservation of species is applied to the control volume as shown in Fig. 3.2d. The conservation of species accounts for each molecular species in the gas mixture, taking into account the chemical reactions that take place within the control volume. The conservation of species, where the net change in species mass flow rates equals the net production rates for each species, is written as

$$\left(\dot{m} + \frac{d\dot{m}}{dz}\Delta z\right)\left(Y_i + \frac{dY_i}{dz}\Delta z\right) - \dot{m} Y_i = \dot{\omega}_i A \Delta z \,. \tag{3.16}$$

Again, the $\frac{d\dot{m}}{dz}$ term can be eliminated and Eq. (3.16) can be simplified to

$$\frac{dY_i}{dz} - \frac{\dot{\omega}_i}{\rho u} = 0 \,. \tag{3.17}$$

Equation (3.17) is really N equations, where N is the number of species in the chemical kinetics model.

Now that all of the conservation equations have been applied, a few more equations are needed to close the model. First, as mentioned above, a relation is needed between the enthalpy and the chemical composition of the gas. This is also a function of temperature and can be expressed as

$$\frac{dh}{dz} = c_p \frac{dT}{dz} + \sum_{i=1}^{N} h_i \frac{dY_i}{dz} \,. \tag{3.18}$$

Additionally, the ideal gas equation of state,

$$p = \rho\left(\frac{R_u}{MW_{mix}}\right)T\,, \tag{3.19}$$

can be differentiated and written as

$$\frac{1}{p}\frac{dp}{dz} = \frac{1}{\rho}\frac{d\rho}{dz} + \frac{1}{T}\frac{dT}{dz} - \frac{1}{MW_{mix}}\frac{dMW_{mix}}{dz}\,. \tag{3.20}$$

The ideal gas relation introduced another new variable, the molecular weight of the gas mixture, that is defined as

$$MW_{mix} = \left[\sum_{i=1}^{N}\frac{Y_i}{MW_i}\right]^{-1}\,. \tag{3.21}$$

This equation can also be differentiated and written as

$$\frac{dMW_{mix}}{dz} = -MW_{mix}^2\sum_{i=1}^{N}\frac{1}{MW_i}\frac{dY_i}{dz}\,. \tag{3.22}$$

The ram PFR model is now fully defined with 6+N equations (Eqs. (3.2), (3.12), (3.15), (3.17), (3.18), (3.20), and (3.22)) and 6+N unknowns ($\frac{d\rho}{dz}$, $\frac{du}{dz}$, $\frac{dp}{dz}$, $\frac{dh}{dz}$, $\frac{dY_i}{dz}$, $\frac{dT}{dz}$, and $\frac{dMW_{mix}}{dz}$). Note that all areas and area derivatives are assumed to be known based on predefined tube and projectile geometries and the species mass production rates are provided by an outside chemical kinetics model. Additionally, all thermodynamic properties can be looked up in a database. To solve this system of equations, they will first be combined and reduced down to a system of 2+N equations:

$$\frac{d\rho}{dz} = \frac{C_I\rho a_p A_{CV}^*\left(\frac{u_p}{\dot{m}c_pT} - \frac{1}{pA}\right) + \frac{1}{\rho u}\sum_{i=1}^{N}\dot{\omega}_i\left(\frac{MW_{mix}}{MW_i} - \frac{h_i}{c_pT}\right) + \frac{u^2}{A}\left(\frac{1}{c_pT} - \frac{\rho}{p}\right)\frac{dA}{dz}}{\frac{u^2}{p} - \frac{u^2}{\rho c_pT} - \frac{1}{\rho}}\,, \tag{3.23}$$

$$\frac{dT}{dz} = \frac{C_I\rho a_p u_p A_{CV}^*}{\dot{m}c_p} - \frac{1}{\rho u c_p}\sum_{i=1}^{N}h_i\dot{\omega}_i + \frac{u^2}{c_p}\left(\frac{1}{\rho}\frac{d\rho}{dz} + \frac{1}{A}\frac{dA}{dz}\right)\,, \tag{3.24}$$

and

$$\frac{dY_i}{dz} = \frac{\dot{\omega}_i}{\rho u} \,. \tag{3.25}$$

This coupled set of 2+N ordinary differential equations (ODEs) can be solved for density, pressure, and gas composition, given a set of initial conditions. From these solved properties, all other state properties can be readily calculated or looked up in a database. The set of coupled ODEs is solved using the built in MATLAB solver, *ode15s*, which is capable of solving the stiff differential equations using the variable order method [43]. The code for the ram PFR model solver and its ODEs can be found in Appendix A.1 and A.2, respectively.

3.1.2 Normal Shock Model

The normal shock location is defined for each solution iteration by the convergence algorithm discussed in Section 3.1.5. The normal shock is always positioned at the end of a computational cell, using the PFR model output from the cell as its input. A further assumption is made that a normal shock cannot occur underneath a baffle wall (i.e., it must occur within a baffle chamber). This is because the normal shock location is defined to occur at a specific flow area, so that the shock strength is such that the thermally choked plane conditions can match those of the thermally choked condition for the given set of inputs. Since the flow area between the baffle walls and the projectile is so drastically smaller than that between the baffle chambers and the projectile, it is only in extreme edge cases where the shock could occur underneath the baffle wall. Even then, when the truly transient nature of the ram accelerator is considered, along with the intended one-way valve nature of BTRA operation, it makes more sense for the normal shock wave to get 'stuck' on the aft end of a baffle wall until it is able to surge forward when the projectile passes the obstruction. The normal shock is modeled using the standard normal shock relations [44].

3.1.3 Projectile Base Area Change Model

At the base of the projectile, where there is a large step change in the flow area, a separate model is applied to account for the flow area change before passing the results to the ram PFR model for the normal cell computation. This is necessary because the ram PFR model cannot handle large step changes in flow area accurately. Additionally, this model allows for a more accurate calculation of the pressure on the projectile base, which is a significant contributor to the overall projectile thrust.

The projectile base area change model takes a different solution approach than the differential equations solved in the ram PFR model. Instead, the integral forms of the conservation equations are solved across the infinitesimally thin control volume shown in Fig. 3.3. Since the control volume is infinitesimally thin, inertial effects are negligible and ignored. First, the conservation of mass in the axial direction can be written as

$$\begin{aligned} \frac{\partial}{\partial t}\int_{CV} \rho dV &= -\int_{CS} \rho \bar{v}\cdot\bar{n}dS \\ &= 0 = -\rho_1(-u_1)A_1 - \rho_2(u_2)A_2\,, \end{aligned} \tag{3.26}$$

where the time derivative term is ignored due to the steady flow assumption. Rearranging, the conservation of mass can be written as

$$\rho_1 u_1 A_1 = \rho_2 u_2 A_2\,. \tag{3.27}$$

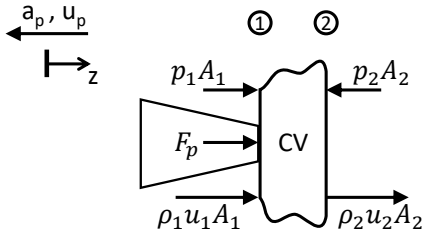

Fig. 3.3 Control volume for the projectile base area change model.

Next, the conservation of momentum for the control volume in the axial direction can be written as

$$\begin{aligned}\frac{\partial}{\partial t}\int_{CV}\rho\overline{v}dV &= -\int_{CS}\rho\overline{v}(\overline{v}\cdot\overline{n})dS - \int_{CS}p\overline{n}dS + \overline{F_p} \\ &= 0 = -\rho_1(-u_1)(-u_1)A_1 - \rho_2(-u_2)(u_2)A_2 - p_1(1)A_1 - p_2(-1)A_2 - F_p\,,\end{aligned} \tag{3.28}$$

again, where the time derivative term is ignored. The force of the projectile on the control volume must also be defined for this case. In determining the force on the projectile base, it makes the most sense to consider the base pressure to be the pressure after the area expansion, p_2. Thus, the projectile force can be written as

$$F_p = p_2(A_2 - A_1)\,. \tag{3.29}$$

Substituting Eq. (3.29) into Eq. (3.28) and rearranging, the conservation of momentum can be rewritten as

$$(\rho_1 u_1^2 + p_1)A_1 = \rho_2 u_2^2 A_2 + p_2 A_1\,. \tag{3.30}$$

Finally, the conservation of energy for the control volume can be written as

$$\begin{aligned}\frac{\partial}{\partial t}\int_{CV}\rho\left(e+\frac{u^2}{2}\right)dV + \int_{CS}\left(h+\frac{u^2}{2}\right)\rho\overline{v}\cdot\overline{n}dS &= \dot{Q} - \dot{W} \\ = 0 + \left(h_1+\frac{u_1^2}{2}\right)\rho_1(-u_1)A_1 + \left(h_2+\frac{u_2^2}{2}\right)\rho_2(u_2)A_2 &= 0 - \dot{W}_{BL}\,,\end{aligned} \tag{3.31}$$

where the time derivative term is ignored. Due to the infinitesimally thin control volume, the heat power input term is assumed to be zero. Additionally, an optional loss term ($\dot{W}_{BL}$) is added to account for the losses due to the rapid expansion at the base. For the results presented in this paper, this term is ignored. The base power loss term can be modified to be in terms of the mass flow rate and rewritten as

$$\dot{W}_{BL} = \dot{m}W_{BL} = \rho_1 u_1 A_1 W_{BL}\,. \tag{3.32}$$

Substituting Eq. (3.32) into Eq. (3.31) and rearranging, the conservation of energy can be written as

$$h_1 + \frac{u_1^2}{2} - W_{BL} = h_2 + \frac{u_2^2}{2} \,. \tag{3.33}$$

Now, the ideal gas equation of state,

$$p = \rho R T \,, \tag{3.34}$$

can be substituted into Eq. (3.27), yielding

$$p_2 = \frac{\rho_1 u_1 A_1 R_2 T_2}{u_2 A_2} \,. \tag{3.35}$$

Equations (3.34) and (3.35) can be substituted into Eq. (3.30) and rearranged, yielding

$$\left[\rho_1 u_1\right] u_2^2 - \left[\rho_1 u_1^2 + p_1\right] u_2 + \left[\rho_1 u_1 \frac{A_1}{A_2} R_2 T_2\right] = 0 \,. \tag{3.36}$$

This is a quadratic equation that can be solved for u_2, where the bracketed terms are the coefficients. However, since T_2 is an unknown, an iterative solution process must be taken. First, T_2 is assumed to be equal to T_1 and Eq. (3.36) is solved for u_2. The lower velocity solution from Eq. (3.36) is chosen since the post-shock, subsonic flow expansion at the projectile base must result in a velocity reduction. Now, Eqs. (3.34) and (3.35) can be solved and remaining state two properties can be calculated or looked up in a database. Finally, both sides of Eq. (3.33) can be calculated and a residual difference can be determined. The temperature guess for T_2 can be updated and the above process repeated until the residual is reduced to an acceptable level and the solution is converged. A custom convergence algorithm was developed to solve this model efficiently and its code can be found in Appendix A.3.

3.1.4 Baffle Wall Model

The baffle wall model accounts for the net effects of each baffle wall on the local flow. Through the initial iterations of this model, it was found that individually modeling the effects of both the forward and aftward

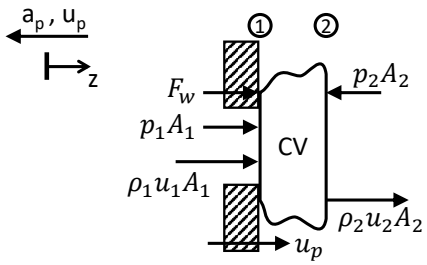

Fig. 3.4 Control volume for the baffle wall model.

facing baffle walls on the local flow would lead to significant flow alterations that would be unrecoverable in the quasi-1D framework of the overall ram PFR model. These flow breakdowns were largely due to the significant flow area reductions between the baffle walls and the projectile. In the quasi-1D framework, these flow area reductions are typically well beyond the limits imposed by the Kantrowitz or isentropic limits discussed in Section 1.3.3. To overcome this impediment, the net affects of each baffle, accounting for both the forward and aftward facing baffle walls, would be applied only at the aftward facing baffle wall edge. Additionally, the flow constriction across the baffle wall would be ignored, where the effects of the constriction and expansion into the subsequent baffle chamber would be included in the baffle model.

The goal of the baffle wall model was to capture the flow effects of the baffles on the local flow by using directly modeled physics, instead of using empirical coefficients as in typical drag models. Thus, each individual baffle would be modeled as a body applying a force on the local flow, while moving at the projectile velocity. This is shown in the control volume diagram in Fig. 3.4. In this model, the control volume is infinitesimally thin, so projectile effects can be ignored. The flow areas A_1 and A_2 are identical, since the control volume sits adjacent to the baffle wall and is infinitesimally thin. However, the flow areas are left as independent variables so that the model can be used where non-identical baffles are placed next to each other, in which case the model will account for the instantaneous flow area change.

First, the conservation of mass is applied to the control volume shown in Fig. 3.4 and can be written as

$$\begin{aligned} \frac{\partial}{\partial t}\int_{CV} \rho dV &= -\int_{CS} \rho\bar{v}\cdot\bar{n}dS \\ &= 0 = -\rho_1(-u_1)A_1 - \rho_2(u_2)A_2\,, \end{aligned} \tag{3.37}$$

where the time derivative is eliminated due to the steady flow assumption. This can be rearranged to write the conservation of mass as

$$\rho_1 u_1 A_1 = \rho_2 u_2 A_2 \,. \tag{3.38}$$

Next, the conservation of momentum in the axial direction for the control volume can be written as

$$\begin{aligned} \frac{\partial}{\partial t}\int_{CV} \rho \bar{v} dV &= -\int_{CS} \rho \bar{v}(\bar{v}\cdot\bar{n}) dS - \int_{CS} p\bar{n} dS + \overline{F_w} \\ &= 0 = -\rho_1(u_1)(-u_1)A_1 - \rho_2(u_2)(u_2)A_2 - p_1(-1)A_1 - p_2(1)A_2 + F_w \,, \end{aligned} \tag{3.39}$$

where the time derivative is once again ignored. This can be rearranged and written as

$$\rho_1 u_1^2 A_1 + p_1 A_1 = \rho_2 u_2^2 A_2 + p_2 A_2 - F_w \,. \tag{3.40}$$

The force of the baffle wall on the control volume, F_w, is really the net force applied on the flow from both the forward and aft facing baffle faces. Ideally, this net force would be derived from both pressure forces and momentum exchange with the fluid near the baffle wall faces. However, since this is a quasi-1D model, the momentum exchange cannot be derived directly without introducing a scaling coefficient to account for the 1D domain of the model. Since the goal of this model, as stated above, was to model the baffle effects from direct physical interactions as opposed to relying on empirical scaling coefficients, the momentum component of the baffle wall force was dropped. The net baffle wall force is calculated using the local gas pressure at the forward and aftward facing baffle walls, as shown in Fig. 3.5. Thus, the net force of the baffle wall on the control volume can be written as

$$F_w = F_{wa} - F_{wf} = p_{wa}A_{wa} - p_{wf}A_{wf} = p_2 A_{wa} - p_{wf}A_{wf} \,, \tag{3.41}$$

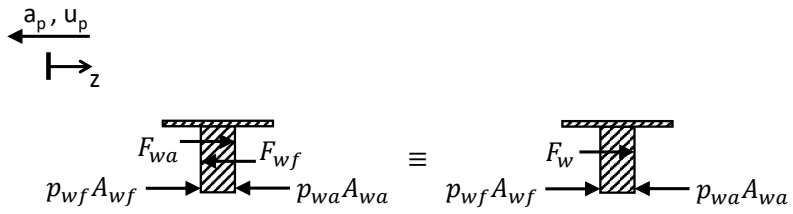

Fig. 3.5 Free body diagram of a baffle wall.

where the baffle wall areas are known and the pressure at the forward facing baffle wall has already been found. Equation (3.41) can be substituted into Eq. (3.40) and rearranged to yield

$$\rho_1 u_1^2 A_1 + p_1 A_1 - p_{wf} A_{wf} = \rho_2 u_2^2 A_2 + p_2 (A_2 - A_{wa}) \,. \tag{3.42}$$

Finally, the conservation of energy for the control volume can be written as

$$\begin{aligned} &\frac{\partial}{\partial t} \int_{CV} \rho \left(e + \frac{u^2}{2} \right) dV + \int_{CS} \left(h + \frac{u^2}{2} \right) \rho \bar{v} \cdot \bar{n} dS = \dot{Q} - \dot{W} \\ &= 0 + \left(h_1 + \frac{u_1^2}{2} \right) \rho_1 (-u_1) A_1 + \left(h_2 + \frac{u_2^2}{2} \right) \rho_2 (u_2) A_2 = 0 + \dot{W}_w \,, \end{aligned} \tag{3.43}$$

where the time derivative term is eliminated. Since the baffles are moving through the control volume at the projectile speed, they do work on the fluid with a positive power input, $\dot{W}_w$. This work is only done by the aftward facing baffle wall since the baffle wall is traveling faster than the fluid at all points in the computational domain. Since the fluid is also moving at some velocity, the relative velocity between the baffle wall and the fluid is used to calculate the power input due to the baffle wall. This can be written as

$$\dot{W}_w = F_{wa} (u_p - u_2) = p_2 A_{wa} (u_p - u_2) \,. \tag{3.44}$$

Substituting Eq. (3.44) into Eq. (3.43), the conservation of energy can be written as

$$h_1 + \frac{u_1^2}{2} = h_2 + \frac{u_2^2}{2} - \frac{p_2 A_{wa}}{\rho_1 u_1 A_1} (u_p - u_2) \,. \tag{3.45}$$

Now, the ideal gas equation of state, Eq. (3.34), can be plugged into Eq. (3.38) to yield

$$p_2 = \frac{\rho_1 u_1 A_1 R_2 T_2}{u_2 A_2} \,. \tag{3.46}$$

Equations. (3.34) and (3.46) can be substituted into Eq. (3.42) and rearranged, yielding

$$\left[1\right] u_2^2 - \left[\frac{\rho_1 u_1^2 A_1 + p_1 A_1 - p_{wf} A_{wf}}{\rho_1 u_1 A_1}\right] u_2 + \left[\left(1 - \frac{A_{wa}}{A_2}\right) R_2 T_2\right] = 0 \,. \tag{3.47}$$

This is a quadratic equation that can be solved for u_2, where the bracketed terms are the coefficients. This is solved in the same iterative manner as the projectile base area change model discussed in Section 3.1.3. In this case, the choice of solution from Eq. (3.47) must be conditionally chosen. The higher velocity solution is chosen when the flow is supersonic and the lower velocity solution is chosen when the flow is subsonic. Also, the conservation of energy equation, Eq. (3.45), is used to calculate the residual for convergence. The same custom convergence algorithm that was used in the projectile base area change model is also used here and the code can be found in Appendix A.4.

3.1.5 Thermally Choked Convergence Criterion

The unique solution for the thermally choked ram accelerator is determined by satisfying the thermally choked convergence criterion. That is, the exit plane of the ram accelerator flowfield should be a sonic point. This has also been shown to be an entropy extremum, making it a uniquely defined state for a given set of inlet conditions [11]. In the context of this model, this choking condition can be generalized in a similar manner as done by Sasoh [39].

Combining the conservation equations, enthalpy relation, and the ideal gas equation of state from the ram PFR model, Eqs. (3.2), (3.12), (3.15), (3.18), and (3.20), the derivative of the mass averaged particle velocity can be written in non-dimensional form as

$$\frac{1}{u}\frac{du}{dz} = \frac{-\frac{1}{c_p T}\sum_{i=1}^{N} h_i \frac{dY_i}{dz} - \frac{1}{A}\frac{dA}{dz} - \frac{1}{MW_{mix}}\frac{dMW_{mix}}{dz} + C_I \rho a_p A_{CV}^* \left(\frac{u_p}{\dot{m} c_p T} - \frac{1}{pA}\right)}{1 - M^2} \,. \tag{3.48}$$

For flow properties to be continuous throughout the domain, the numerator in Eq. (3.48) must be zero at the sonic point (where the denominator is zero). Thus, the following equation can be written as the generalized choking condition for the ram PFR model:

$$-\frac{1}{c_p T}\sum_{i=1}^{N} h_i \frac{dY_i}{dz} - \frac{1}{A}\frac{dA}{dz} - \frac{1}{MW_{mix}}\frac{dMW_{mix}}{dz} + C_I \rho a_p A^*_{CV}\left(\frac{u_p}{\dot{m} c_p T} - \frac{1}{pA}\right) = 0\,. \tag{3.49}$$

The first term in Eq. (3.49) is the heat release of the chemical reaction. The second term can be assumed to be zero in the region behind the projectile where the thermally choked plane sits, assuming that mechanical choking does not occur in the area constriction between the baffle walls. This assumption is enforced in the model, where results are thrown out when this phenomena occurs. Also, if choking were to occur on the projectile, say in the transdetonative operating mode, this term would be non-zero and be critical in determining the correct solution. The third term is generally negligible, as argued by Sasoh [39]. Finally, the fourth term is unique to the ram PFR model as it accounts for the effects of the non-inertial reference frame. For computational simplicity, this term is ignored in the present model but could be included in future versions for improved accuracy. This leaves the heat release as the only surviving term that now must be equal to zero. Thus, the thermally choked convergence criterion for the ram PFR model is where the heat release goes to zero at the thermally choked plane.

The thermally choked convergence criterion is enforced in the ram PFR model by iteratively choosing normal shock locations on the projectile tail cone until the criterion is satisfied. This occurs when the sonic point is reached just as the heat release of the reaction goes to zero. When the shock is positioned too far back on the projectile, and the normal shock is too strong, the sonic point is reached before heat release goes to zero. If the shock is positioned too far forward on the projectile, and the shock is not strong enough, combustion goes to completion without achieving a sonic point. An algorithm was developed to iterate through shock location guesses until the appropriate shock location is narrowed down to a single computational cell. Each iteration requires a full solution of the ram flow field and produces either a choked or not-choked result. To speed up this computation, combustion completion and choking completion checks were introduced. These checks identified when either combustion had completed or a

sonic point had been reached, at which point all remaining cells in the computational domain were held constant, skipping their computations. The code for the ram PFR convergence algorithm can be found in Appendix A.5.

3.2 Ram Accelerator PFR Model Results

A number of studies were carried out using the new ram accelerator PFR model. The first study focused on the initial validation of the model by comparing results to prior theory and experiments, as well as individually studying the effects of the baffle wall model and the non-inertial reference frame corrections. These results are presented in Section 3.2.1. The second study compared the performance of different BTRA geometries, namely the BTRA 500 and BTRA 100. This study is presented in Section 3.2.2. Next, the RTRA 200 was studied, with results presented in Section 3.2.3. Finally, the operational envelopes of all ram configurations were studied with results presented in Section 3.2.4. A summary discussion of all of the ram accelerator PFR model results can be found in Section 3.3.

3.2.1 Model Validation Results

The initial validation of the ram accelerator PFR model was carried out using the RTRA 200 configuration, due to its simpler geometry. Since there are no baffles in the RTRA, the PFR model results can be compared directly to control volume theory discussed in Section 1.3. In this study, the P300 projectile was modeled in the RTRA 200, using $2.2CH_4 + 2O_2 + 7.52N_2$ propellant at 21 atm and 300 K. Simulations were carried out with projectile accelerations of 10,000 g and 0 g, where 10,000 g is a typical projectile acceleration in the experiments discussed in Chapter 2. Figure 3.6 shows the non-dimensional thrust, the shock distance from the projectile base, and the normalized thermally choked plane distance from the projectile base versus Mach number for this study. As shown in Fig. 3.6a, the 10,000 g thrust curve from the ram PFR model has a distinctly different curvature than the CV theory curve. The CV theory has been well validated with both SBRA experiments and the initial RTRA experiments discussed in Section 2.3,

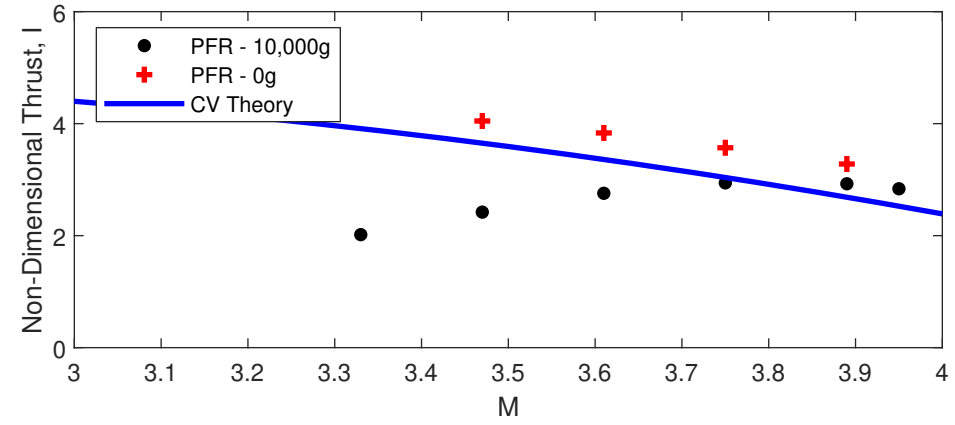

(a)

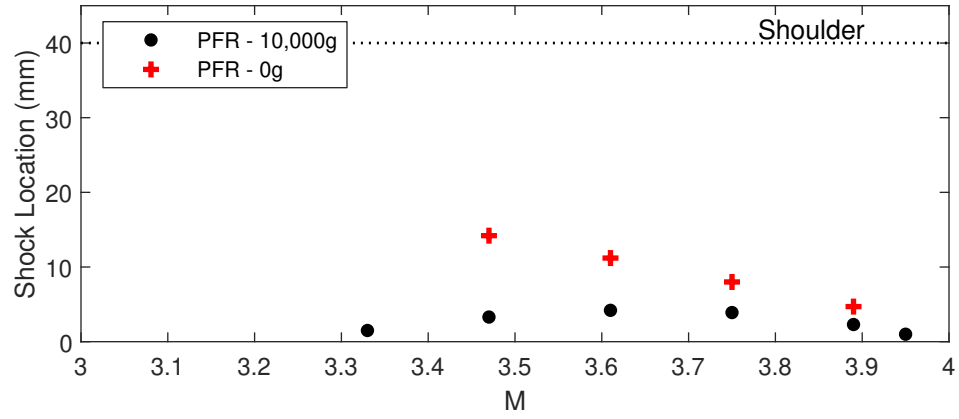

(b)

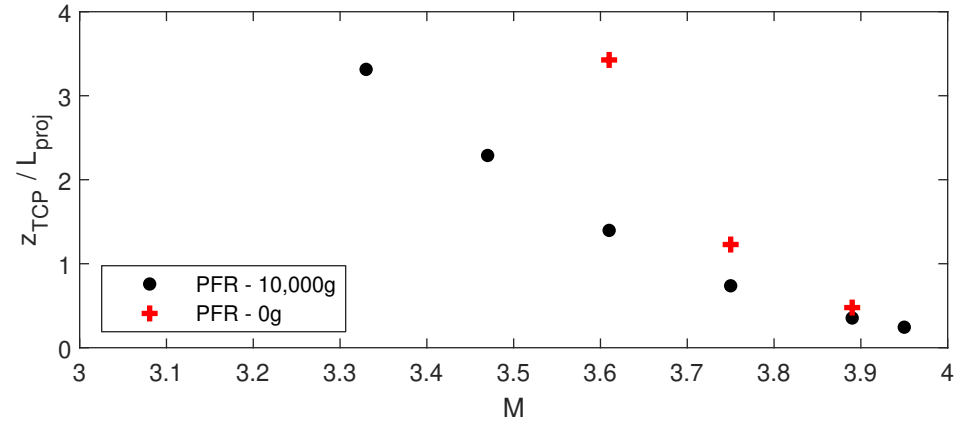

(c)

Fig. 3.6 Non-dimensional thrust (a), shock distance from projectile base (b), and the normalized thermally choked plane location (c) versus Mach number for the ram accelerator PFR model with a P300 projectile in the RTRA 200, using 2.2CH4 + 2O2 + 7.52N2 propellant.

so this discrepancy was initially concerning. However, the thrust in the 0 g case, where there is no inertial correction term, has a curvature that matches that of the CV theory very well, with a slight offset. This indicates that the projectile acceleration, and the associated inertial corrections, are the primary reason for the difference in curvature of the ram PFR thrust curve. The reason for the lower thrusts calculated by the ram PFR model becomes apparent when looking at the shock location curves in Fig. 3.6b. With no projectile acceleration, the normal shock falls further back on the projectile with increasing Mach number in a linear relation. The 10,000 g acceleration causes the normal shock to move further back on the projectile at lower Mach numbers. However, as the projectile Mach number increases, the shock starts to move forward to a maximum distance, and then begins receding, converging with the linear shock location curve of the 0 g case at high Mach numbers. The shock location curves are naturally correlated to the thrust curves since the thrust is calculated by integrating the pressure forces across the projectile body, and the high pressure region that provides the thrust begins immediately behind the normal shock. Thus, the further the normal shock is on the projectile body, the higher the thrust. While this result suggests the inertial corrections for projectile acceleration are inaccurate, later results will show that the shock locations predicted while accounting for the projectile acceleration match experiments remarkably well.

The thrust in the 0 g case in Fig. 3.6a matches the curvature of the CV theory curve, but overpredicts thrust by a consistent offset. After looking into the cause for this, it was found that the propellant heat release predicted by the ram PFR model exceeded that of the CV theory by about 30%, which accounts for the higher thrust predictions. After simulating the same case but with a stoichiometric propellant, $1CH_4 + 2O_2 + 7.52N_2$, it was found that both the thrust and heat release matched the CV theory. These results are shown in Fig. 3.7. This stoichiometric propellant showed the same differences with varying projectile accelerations, but the offset in the thrust curve at 0 g was gone, matching the CV theory well. The heat release predicted by the ram PFR model matched that of the CV theory within about 2%. This close agreement was also consistent across all later ram PFR simulations of stoichiometric propellants in both the RTRA and the BTRA. This result suggests that the chemical kinetics model cannot accurately simulate the combustion of fuel-rich propellant mixtures for the ram system. This really only affects the

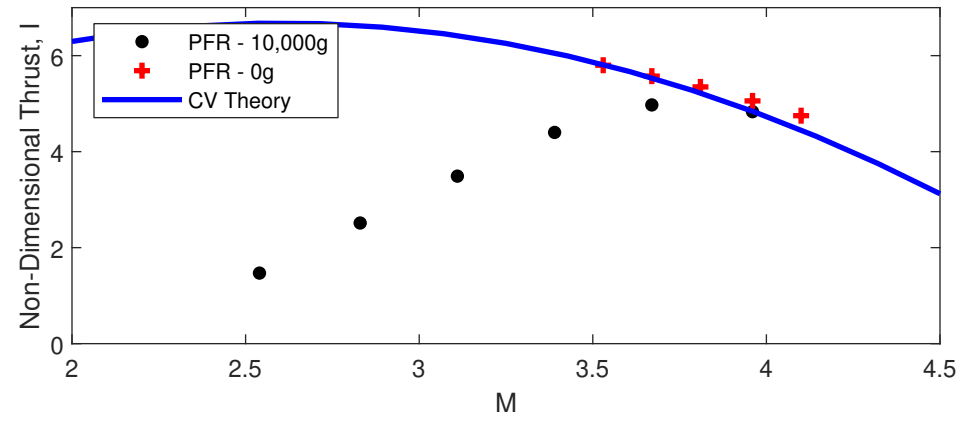

(a)

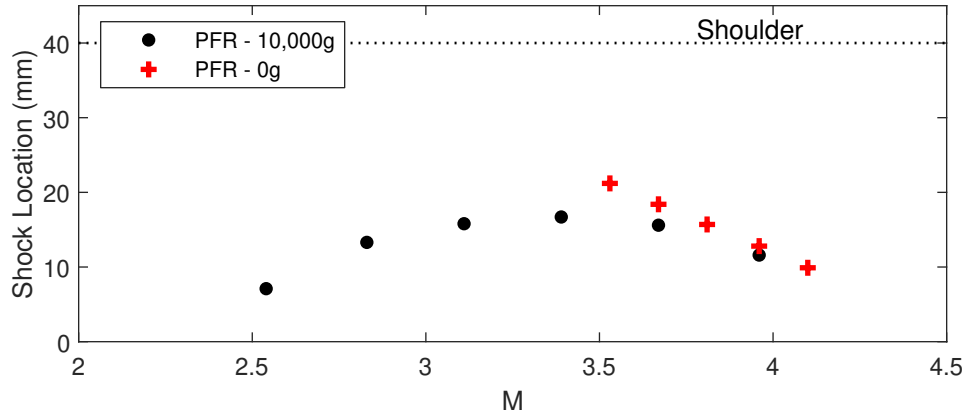

(b)

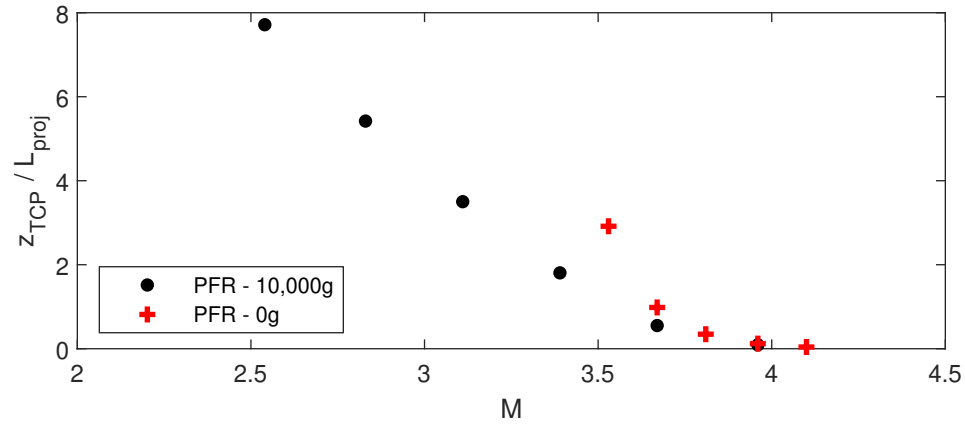

(c)

Fig. 3.7 Non-dimensional thrust (a), shock distance from projectile base (b), and the normalized thermally choked plane location (c) versus Mach number for the ram accelerator PFR model with a P300 projectile in the RTRA 200, using 1CH4 + 2O2 + 7.52N2 propellant.

RTRA modeling, which typically uses fuel-rich propellants, but should not affect the BTRA modeling since all BTRA propellant mixtures are stoichiometric.

The good agreement of the ram PFR thrust curve with the CV theory for an RTRA, as shown in Fig. 3.7a, is promising evidence for the validity of the ram accelerator PFR model.

The ram PFR model validation for the BTRA began with a comparison of the modeled ram flowfields with those from the prior Sasoh model [39]. Figures 3.8 and 3.9 show the major property profiles throughout the ram flowfield for two different Mach number cases, 3.89 and 2.82. These figures show the Mach number, O_2 mass fraction, pressure ratio, and temperature ratio profiles throughout the ram flowfield, with the P300 projectile and BTRA 500 baffles overlaid for reference. The propellant used was 1CH4 + 2O2 + 4.67N2, which was the typical propellant used in experiments. These profiles have the same general shape and trends as produced by the Sasoh model. They also highlight the trend shown in the Sasoh model where higher Mach number operation results in shorter combustion zone lengths. This is expected since the normal shock is stronger at higher Mach numbers, causing higher post-shock pressures and temperatures that significantly speed up combustion. The most evident deviations from the Sasoh model are due to the projectile shape and the presence of baffles. The P300 projectile used in the ram PFR model features a constant area shoulder region, which shows up as a section of near-constant properties after the nose cone region, and the truncated base, which causes a step change in properties across it. The effects of the baffles are a bit harder to see in Figs. 3.8 and 3.9. Instead, Fig. 3.10 shows the zoomed in Mach number an temperature ratio profiles along the projectile and behind the projectile, respectively. The baffles cause a local increase in Mach number in the supersonic flow along the nose cone compression region but have little effect along the projectile shoulder, due to the only minor flow changes in the constant area region. This has a net effect of raising the effective projectile Mach number for a given projectile velocity. The zoomed in temperature ratio behind the projectile, shown in Fig.3.10b, highlights the effect of the baffles on the propellant combustion. Where the temperature is otherwise steadily increasing as combustion grows in intensity, the baffles cause local temperature increases. This accelerates the combustion reaction and has the net effect of reducing the total combustion zone length.

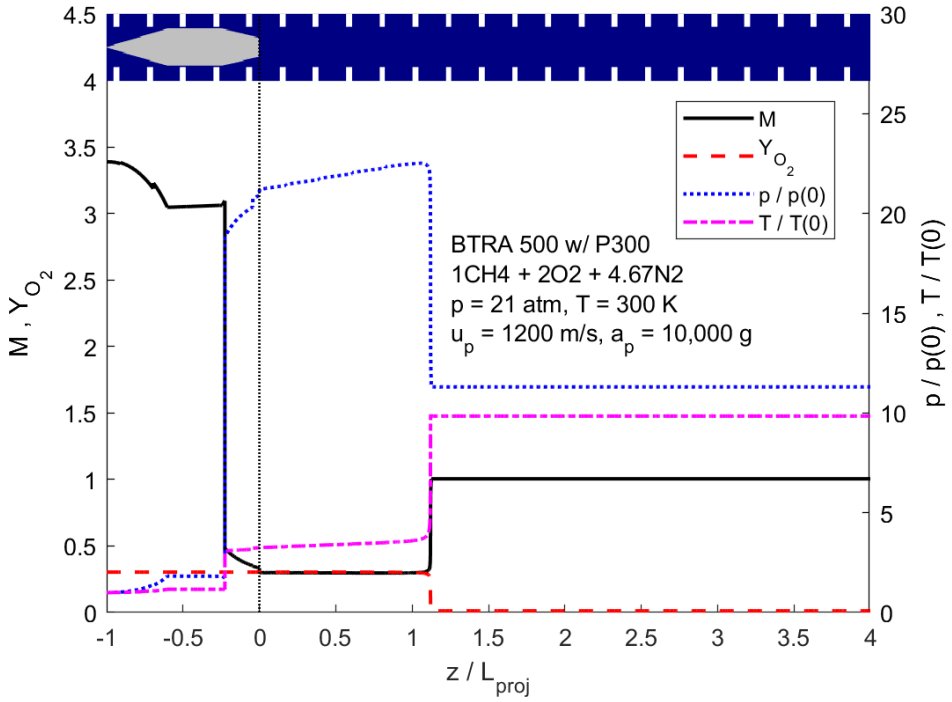

Fig. 3.8 Mach number, O_2 mass fraction, pressure ratio, and temperature ratio profiles from the ram PFR model in the BTRA 500 with 1CH4 + 2O2 + 4.67N2 propellant at Mach 3.89.

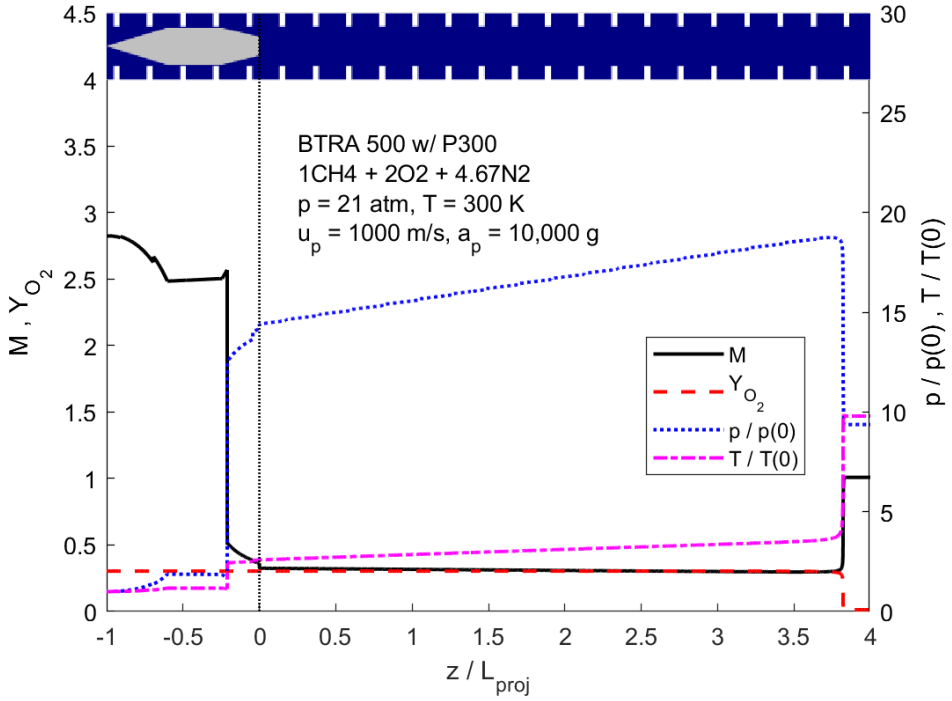

Fig. 3.9 Mach number, O_2 mass fraction, pressure ratio, and temperature ratio profiles from the ram PFR model in the BTRA 500 with 1CH4 + 2O2 + 4.67N2 propellant at Mach 2.82.

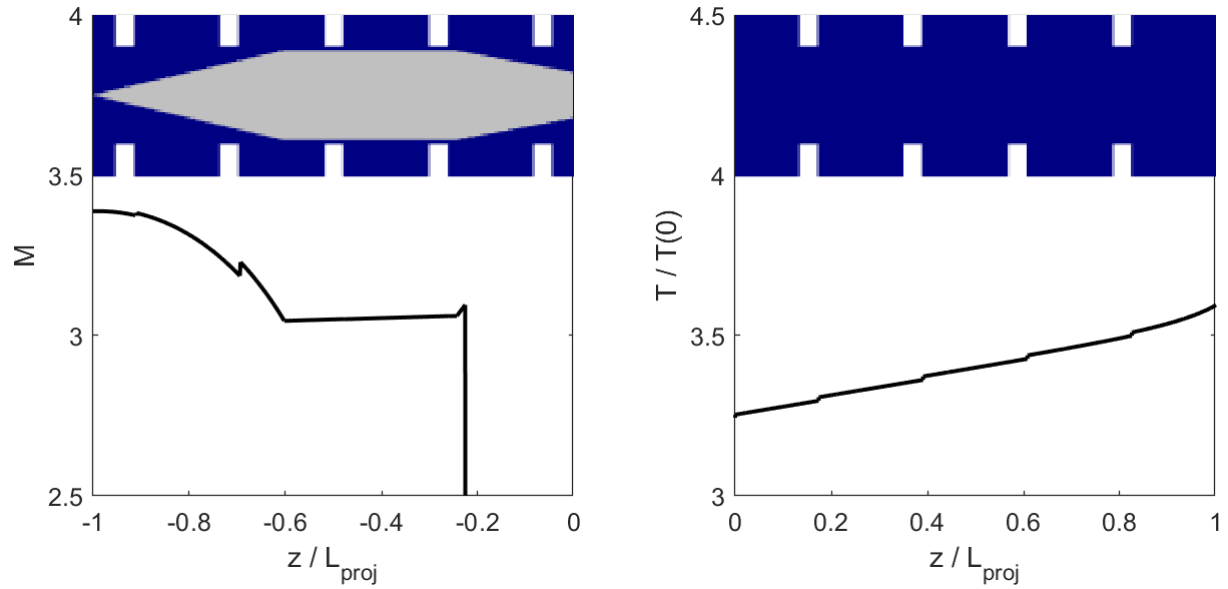

Fig. 3.10 Zoomed in Mach number profile along the projectile (a) and temperature ratio behind the projectile (b) for the ram PFR model in the BTRA 500 with 1CH4 + 2O2 + 4.67N2 propellant at Mach 3.89.

The results presented in Figs. 3.8 and 3.9 are for just a single projectile position within the BTRA 500. In reality, the projectile will transit each baffle and the flowfield around the projectile should be affected by the relative positions of each baffle wall. Thus, for any given case to be studied, solutions must be obtained for projectile locations spanning the length of one full baffle. An example of a set of five projectile locations is shown in Fig. 3.11, where the projectile base location is referenced to a forward facing baffle wall edge.

To study the effects of projectile position within a baffle, a sweep of 17 projectile locations was done for a reference case of the BTRA 500 with 1CH4 + 2O2 + 4.67N2 propellant at 21 atm and 300 K. The projectile was a P300 at Mach 3.89. Figure 3.12 shows the non-dimensional thrust, the shock distance from the projectile base, and the normalized thermally choked plane distance from the projectile base over the range of projectile locations in the baffled tube. There are four different solution types that are displayed on these plots. First, the nominal solution type is one that satisfied all the assumptions of the model described in the sections above. Second, the shock on baffle wall solution is one where the normal shock occurs on an aftward facing baffle wall edge. This occurs when the shock would otherwise occur underneath

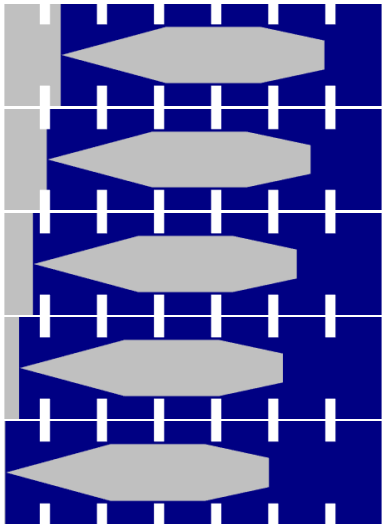

Fig. 3.11 Projectile positioning at different z_{baffle} locations (z_{baffle} = 0.5 mm, 9.2 mm, 17.9 mm, 26.5 mm, and 35.2 mm).

the baffle wall but is forced back to the aft edge, as discussed in Section 3.1.2. The third solution type occurs when the thermally choked plane occurs on an aftward facing baffle wall edge. This case represents mechanical choking between the baffle walls but does not represent a physically or numerically accurate solution as discussed in Section 3.1.5. Finally, the fourth solution type is the shock on shoulder solution. This is where the normal shock is positioned beyond the projectile tail cone and onto the shoulder, or beyond. In this situation, the baffles in a BTRA should prevent the shock from surging forward and causing an unstart. Since, the ram PFR model does not have a way of modeling this due to its quasi-1D formulation, these situations are not modeled in full. Instead, the normal shock is assumed to occur at the start of the shoulder, resulting in a solution that does not satisfy the generalized choking condition.

In Fig. 3.12, the shock on baffle wall solutions occur when the nominal normal shock location is obstructed by a baffle wall, in this case, correlating very closely to the top and bottom projectile positions shown in Fig. 3.11. The non-dimensional thrusts in these cases are relatively low and represent an expected thrust loss when the normal shock, and resultant high pressure region, is pushed further back on the projectile. Since the projectile thrust is calculated by summing the pressure forces on the projectile from each cell, the loss in area for the high pressure region to push on reduces the total thrust. This phenomena

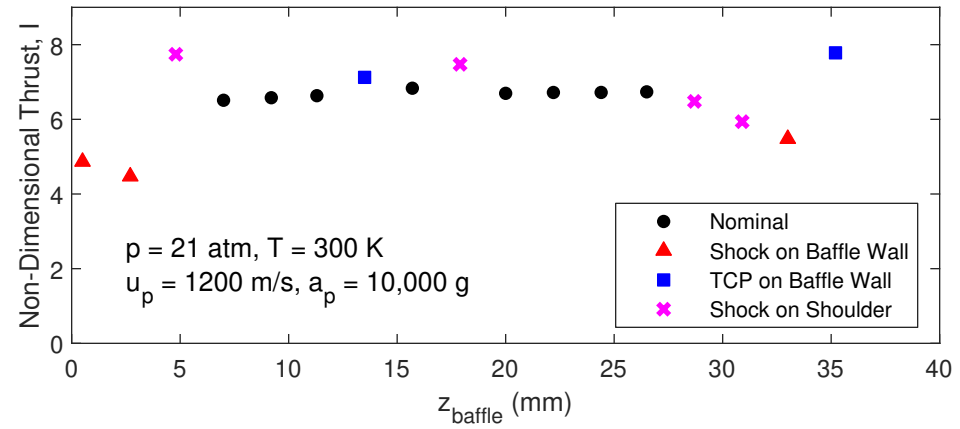

(a)

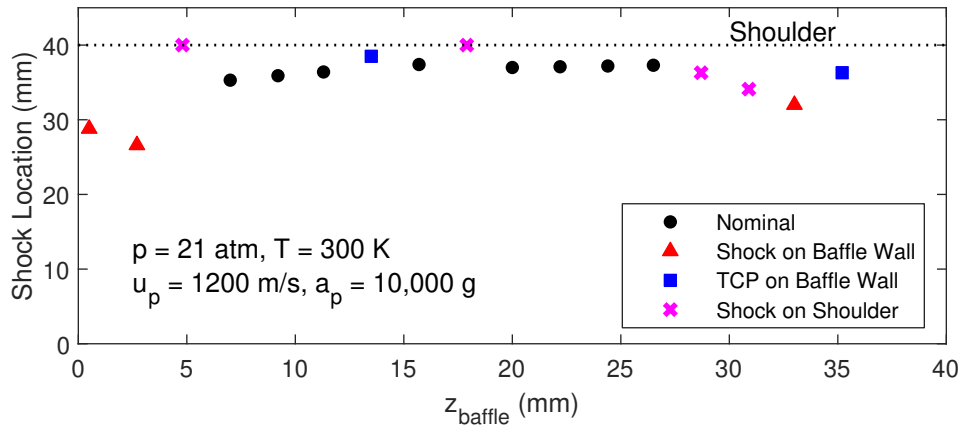

(b)

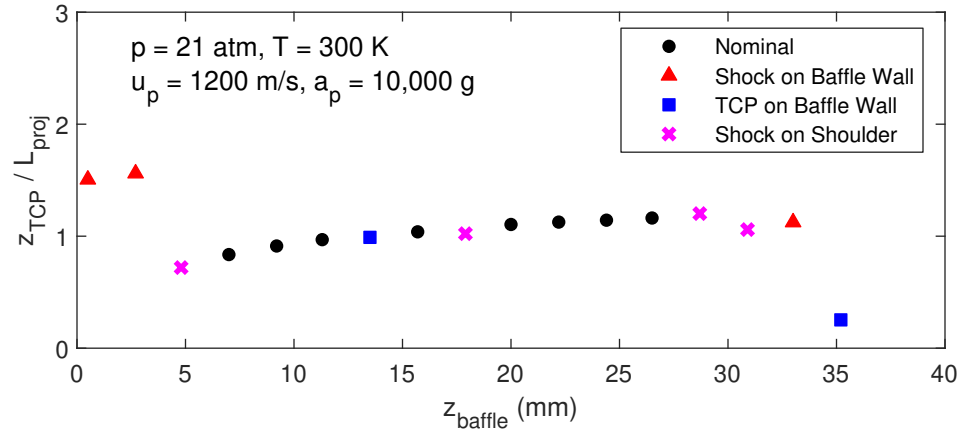

(c)

Fig. 3.12 Non-dimensional thrust (a), shock distance from projectile base (b), and the normalized thermally choked plane location (c) versus projectile position in a baffle for the ram accelerator PFR model with a P300 projectile in the BTRA 500, using 1CH4 + 2O2 + 4.67N2 propellant.

is evident due to the close correlation between the non-dimensional thrust and shock location plots in Fig. 3.12a and 3.12b, respectively. The thermally choked plane on baffle wall solutions vary from minor to major deviations from the nominal solutions. This is not surprising because the early mechanical choking can occur at various stages of combustion completion, which can lead to unpredictable deviations from the generalized choking criterion that governs the nominal solutions. As expected, the shock on shoulder solutions generally lead to higher than nominal thrust since the shock is positioned further up on the projectile. However, these solutions do not satisfy the generalized choking condition so should not be considered as accurate.

Both the non-dimensional thrust and shock location remain relatively constant throughout the baffle transit when considering the nominal solutions only. However, the thermally choked plane distance from the projectile base generally increases as the projectile base moves further from the forward facing baffle wall. The thermally choked plane distance then experiences a step change when the shock passes from one side of a baffle wall to the other. Since the profiles shown in Fig. 3.12 represent one full baffle transit, the solutions represent just one period of a periodic solution. In order to get singular values for each parameter for a given operating condition, the average values of all the nominal solutions for each baffle transit were taken. Though this excludes the lower performance effects of the shock on baffle wall solutions, they were omitted since they were not numerically or physically accurate solutions in their current forms. It is assumed that the exclusion of these cases will have only a minor impact on the overall results, especially when compared to the expected inaccuracies due to the other model assumptions.

After the initial ram PFR model solutions were studied and well understood for a single baffle transit, a full study was conducted to compare results to those from the prior CV theory (from Section 1.3.2) and experiments. This study utilized the P300 projectile in the BTRA 500 with $1CH_4 + 2O_2 + 4.67N_2$ propellant at 21 atm and 300 K. For this and all later studies, unless otherwise noted, the projectile acceleration was set to 10,000 g, a typical value in experiments. Instead of the 17 baffle transit locations used in the prior study, nine locations were used in this and all future studies to reduce the total computation time. Figure 3.13a compares the non-dimensional thrust versus Mach number for the ram PFR model,

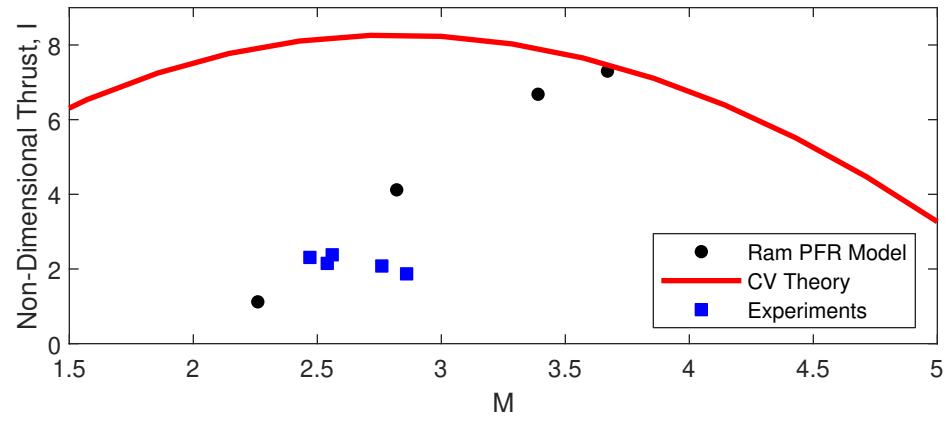

(a)

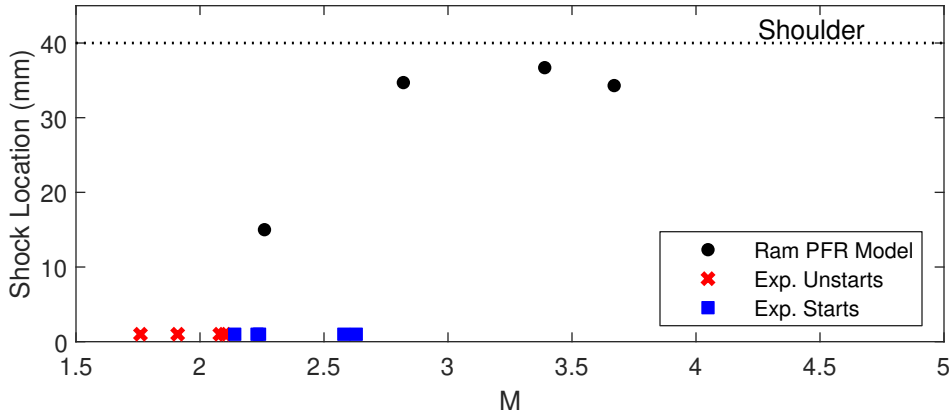

(b)

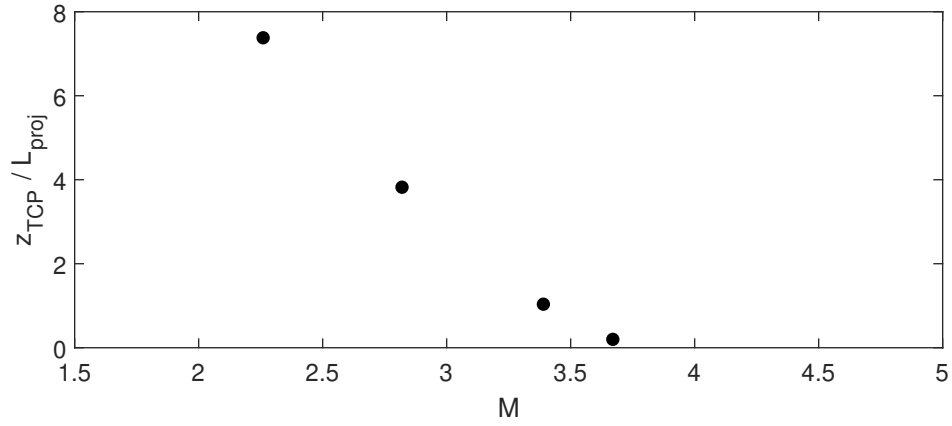

(c)

Fig. 3.13 Non-dimensional thrust (a), shock distance from projectile base (b), and the normalized thermally choked plane location (c) versus Mach number for the ram accelerator PFR model with a P300 projectile in the BTRA 500, using 1CH4 + 2O2 + 4.67N2 propellant.

the CV theory, and experiments. The ram PFR model and the CV theory predict distinctly different thrust curves. This is due to the 10,000 g projectile acceleration in the ram PFR case, as discussed above. While the ram PFR model at 10,000 g more closely matches the experimental thrust magnitudes, the CV theory (and the 0 g ram PFR case) predicts the general curvature of the thrust curve more accurately. In Section 2.7, combustion efficiency was discussed as the likely reason for large offsets between CV theory and experiments. However, this has yet to be proven so the ram PFR model with non-zero accelerations cannot be entirely discounted for thrust predictions.

The flowfield parameters of shock location and the thermally choked plane location for this study are shown in Figs. 3.13b and 3.13c, respectively. The shock location has a roughly parabolic shape to its curve. The points where this curve crosses the zero line are where the normal shock falls off the back of the projectile. The lower Mach number crossing is where the normal shock first catches up to the projectile and represents the minimum operable Mach number for the propellant. The higher Mach number crossing represents the true 'wave falloff' condition discussed in Section 1.3.3, where the combustion driven shock system is no longer energetic enough to keep up with the projectile. However, in this particular case, the thermally choked plane catches up to the projectile before this condition occurs. This happens where the thermally choked plane position crosses the zero line in Fig. 3.13c and is representative of the transition into the transdetonative ram accelerator mode where combustion completes on the projectile body. The Mach numbers of several experimental starts and unstarts are shown in Fig. 3.13b, along with the ram PFR model shock location results. This figure highlights that the ram PFR model does a remarkably good job at predicting the minimum operable Mach number through its prediction of when the normal shock first catches up to the projectile. Notably, this is a prediction that is heavily affected by both the baffle wall model and non-inertial reference frame corrections, indicating that these are both important components of the ram PFR model.

Next, the direct effects of the baffle wall model were studied by comparing results for two identical tube configurations, where the effects of the baffles were completely ignored in one. Since the ram PFR model does not consider flow area changes underneath baffle walls, this is as simple as turning the baffle

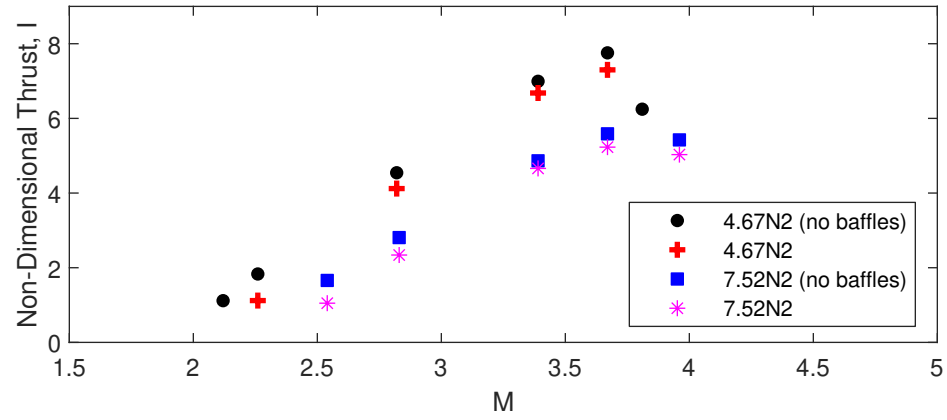

(a)

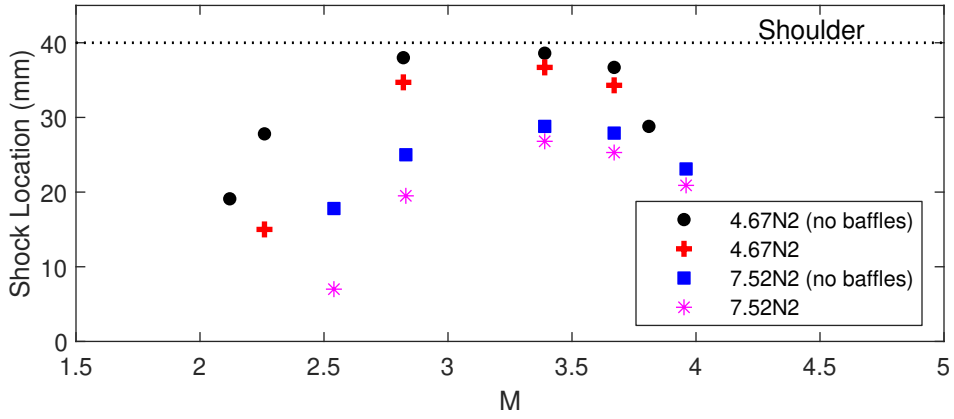

(b)

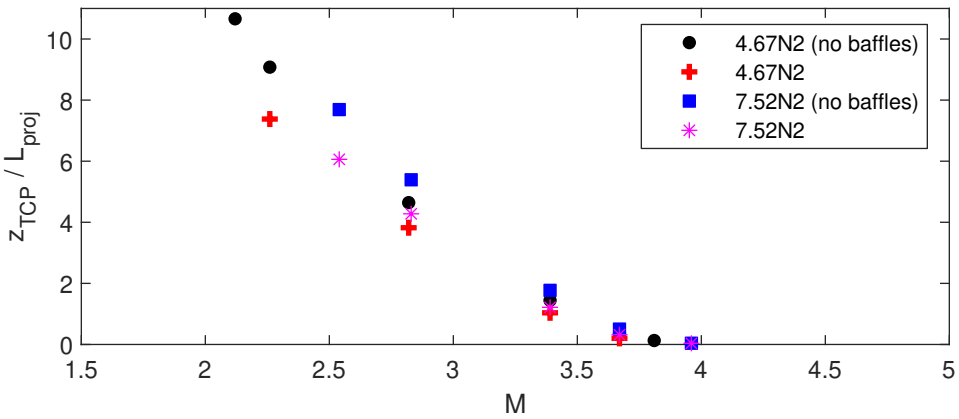

(c)

Fig. 3.14 Comparisons of non-dimensional thrust (a), shock distance from projectile base (b), and the normalized thermally choked plane location (c) versus Mach number for the ram accelerator PFR model with a P300 projectile in the BTRA 500 with and without the baffle walls modeled, using 1CH4 + 2O2 + xN2 propellant.

wall model off, while using the same tube geometry. This was done in the BTRA 500 with the P300 projectile. Two different propellants at 21 atm and 300 K were used to identify any chemistry influences. The results of this study are shown in Fig. 3.14. The inclusion of the baffle wall model causes a reduction in the non-dimensional thrust at all Mach numbers. This is well correlated to the shock location which falls further back on the projectile tail cone when the baffles are included. Finally, the inclusion of the baffle wall model causes the combustion zone length to shorten. Additionally, the effect of the baffles on all three parameters tended to be larger at lower Mach numbers. These trends were consistent for both propellants tested in this study. In effect, the baffle wall model shows that baffles reduce the operational envelope of a given propellant mixture in the thermally choked operating mode, at least in terms of the operable Mach number range. This is accompanied by a corresponding reduction in thrust performance. Initially, this may seem at odds with the demonstrated effects of baffles on the ram accelerator, where they have been shown to enable operation at lower Mach numbers as discussed in Chapter 2. However, it has already been shown that to operate in a smooth bore or railed tube, such as in the 'no baffle' cases here, much lower heat release propellants are required. Thus, the reduced operating envelope caused by the baffles is offset by the expanded operating envelope in the more energetic propellants made possible by the baffles.

Finally, the effect of the non-inertial reference frame corrections was studied. In this study, a variety of projectile accelerations were compared to each other to determine the relative effects of the inertial corrections. Simulations were ran with the P300 projectile in the BTRA 500 with $1CH_4 + 2O_2 + 4.67N_2$ propellant at 21 atm and 300 K. These results are shown in Fig. 3.15. At all Mach numbers, increasing projectile accelerations caused a reduction in the non-dimensional thrust, pushed the normal shock further back on the projectile, and reduced the combustion zone length. Of note, in the 0 g acceleration case, where there is no inertial correction, only solutions at high Mach numbers were found since the normal shock moves to the projectile shoulder at lower Mach numbers. Additionally, the measurable differences in the Mach number limits due to the inertial corrections suggests that they are, in fact, vital in determining the true operating limits of the ram accelerator. These limits are discussed in more detail in Section 3.2.4.

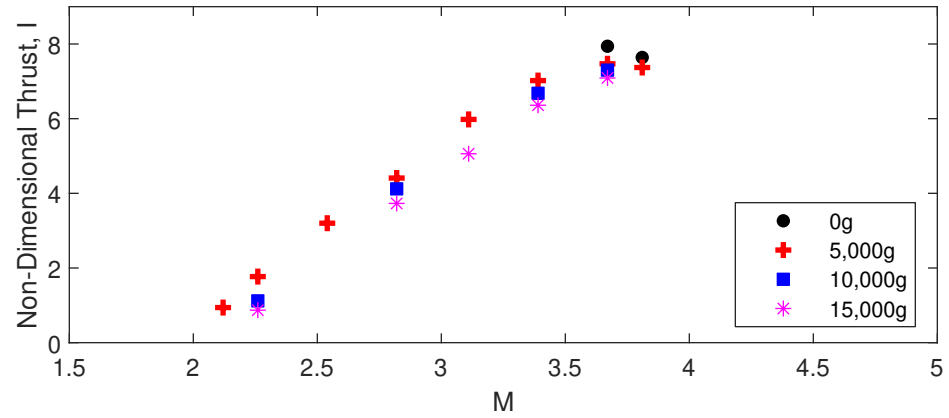

(a)

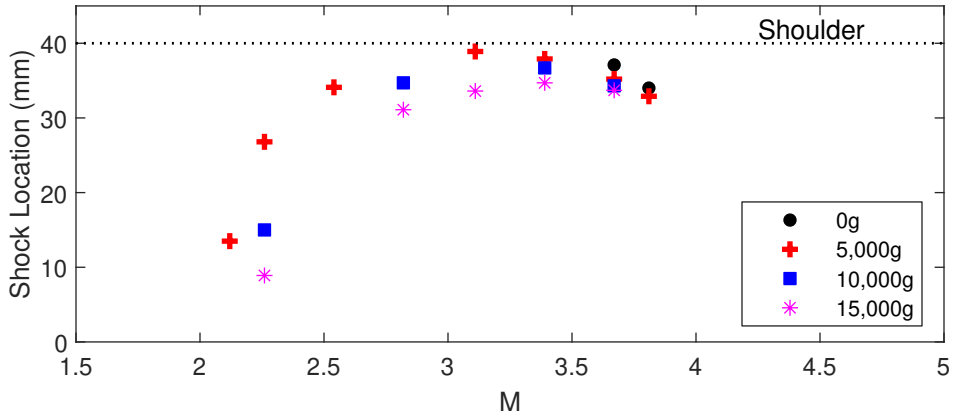

(b)

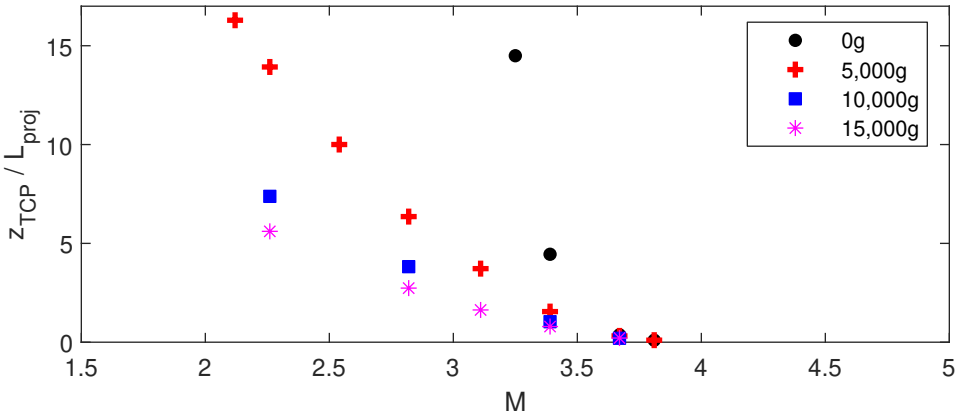

(c)

Fig. 3.15 Comparisons of non-dimensional thrust (a), shock distance from projectile base (b), and the normalized thermally choked plane location (c) versus Mach number for the ram accelerator PFR model with a P300 projectile in the BTRA 500 at different projectile accelerations, using 1CH4 + 2O2 + 4.67N2 propellant.

3.2.2 BTRA Geometry Studies

The ram PFR model was used to study the effects of different baffle geometries on ram accelerator performance. Specifically, the effect of baffle chamber diameter on ram performance was studied, using the BTRA 500 and BTRA 100 designs as a basis. It was initially found that using the typical experimental propellant, $1CH_4 + 2O_2 + 4.67N_2$, in the BTRA 100 would result in the shock on projectile shoulder solution for most Mach numbers since the normal shock tends to move further up on the projectile body when the tube diameter increases. Thus, a less energetic propellant, $1CH_4 + 2O_2 + 7.52N_2$, was used in the BTRA simulation comparisons. As a consequence, there is no experimental data to add to these comparisons. As can be seen in Fig. 3.16, the non-dimensional thrust and the combustion zone length are virtually unaffected by the differences in baffle chamber size. This means that the (dimensional) thrust in the BTRA 100 should be higher than the that of the BTRA 500, due to the larger effective area. However, this is not seen in experimental results, where the opposite is true. This is likely due to the combustion efficiency problem discussed in Section 2.7. The primary difference that is observed between the ram PFR model results for both BTRAs is in the shock location, as shown in Fig 3.16b. The larger baffle chamber diameters cause the normal shock to move further up on the projectile body at all Mach numbers. This is due to the lower amount of ram compression in the larger diameter baffle chambers, resulting in lower pressures upstream of the normal shock that allow it to be pushed forward. This has the net effect of expanding the range of operable Mach numbers in a BTRA by increasing the baffle chamber diameter. A full comparison of the operating envelopes of the BTRA 500 and BTRA 100 can be found in Section 3.2.4.

This comparison was also extended to a potential future BTRA design, the BTRA 620, which features an even smaller baffle chamber diameter at 50.8 mm. This design was chosen as a natural candidate for future experiments due to the observed trends of increased performance in smaller diameter baffle chamber configurations, as discussed in Chapter 2. The simulation results for this BTRA configuration are plotted alongside the BTRA 500 and BTRA 100 results in Fig. 3.16. The results continued the trends seen in the prior BTRA simulations, while showing some slight performance improvement at lower Mach numbers. These are compelling results that add further motivation to explore smaller diameter BTRAs.

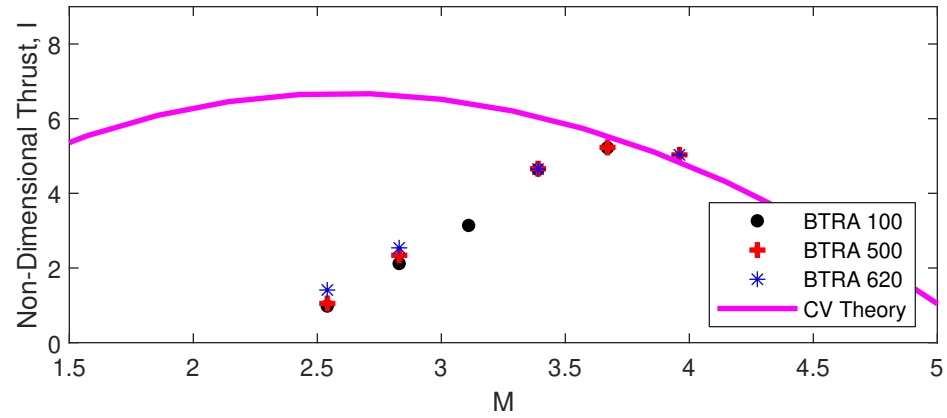

(a)

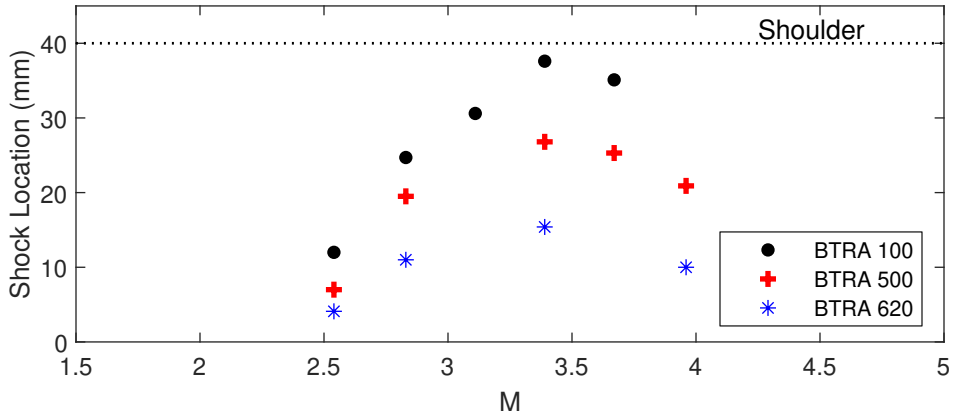

(b)

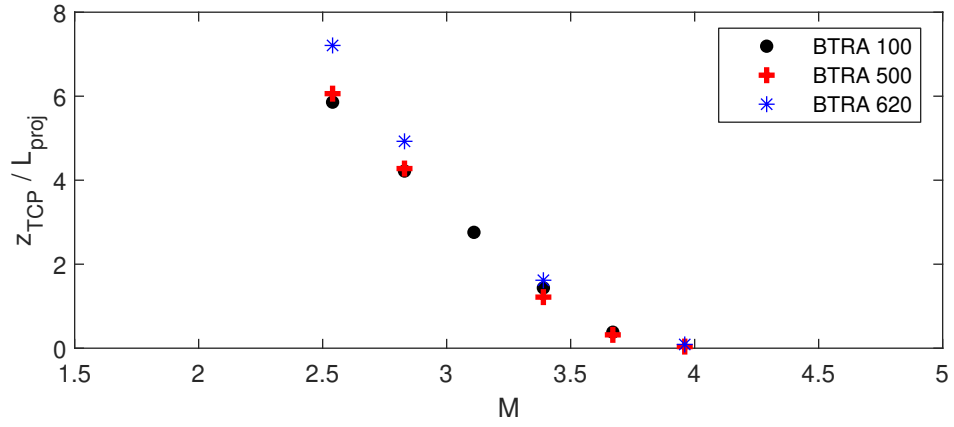

(c)

Fig. 3.16 Comparisons of non-dimensional thrust (a), shock distance from projectile base (b), and the normalized thermally choked plane location (c) versus Mach number for the ram accelerator PFR model in the BTRA 500, BTRA 100, and BTRA 620, using 1CH4 + 2O2 + 7.52N2 propellant.

3.2.3 RTRA 200 Study

The ram accelerator PFR model was also used to study the RTRA 200. Initially, simulations were run using $2.2CH_4 + 2O_2 + 7.52N_2$ propellant. This was the nominal propellant used in experiments at 21 atm or higher, as discussed in Section 2.3. The P300 projectile was used with the propellant fill pressure and temperature set to 21 atm and 300 K, respectively. The results of this study are shown in Fig. 3.17. The non-dimensional thrust results for the ram PFR model of the RTRA 200 are much closer to the CV theory results than they were for the BTRAs. Though, there is still a clear difference in curvatures between the two predicted thrust curves. This difference was explained in Section 3.2.1, above. The experimental thrust results are fairly close to both the CV theory and the ram PFR model results, though they tend to match the curvature of the CV theory better. This is also consistent with the BTRA comparisons to experiments. It is clear from the shock locations in Fig. 3.17b that this propellant is just barely energetic enough to maintain ram operation, as the normal shock sits relatively far back on the projectile tail cone throughout the range of Mach numbers. This is consistent with the experimental results, where experiments with lower fill pressures required more energetic propellants to operate (see Section 2.3). Another notable feature of this particular case is that the normal shock crosses the zero axis at a lower Mach number than the thermally choked plane location does, opposite to most cases discussed thus far. That means that for this propellant, a projectile will experience a wave falloff failure before it can transition to the transdetonative operating mode. In order to avoid this, a more energetic propellant would be required at higher Mach numbers to allow that transition before wave falloff occurs.

Additional propellants were simulated in the RTRA 200 using the ram PFR model to get a better representation of its operational limits. These results are presented and discussed in more detail in Section 3.2.4, alongside the similar BTRA results.

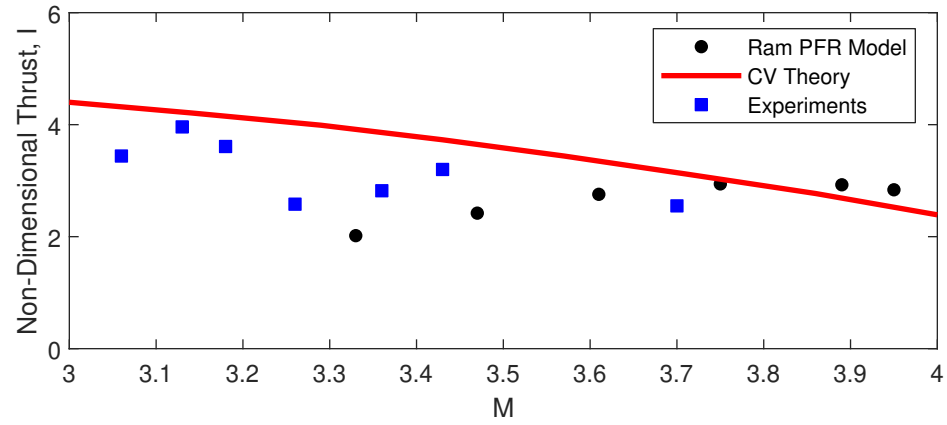

(a)

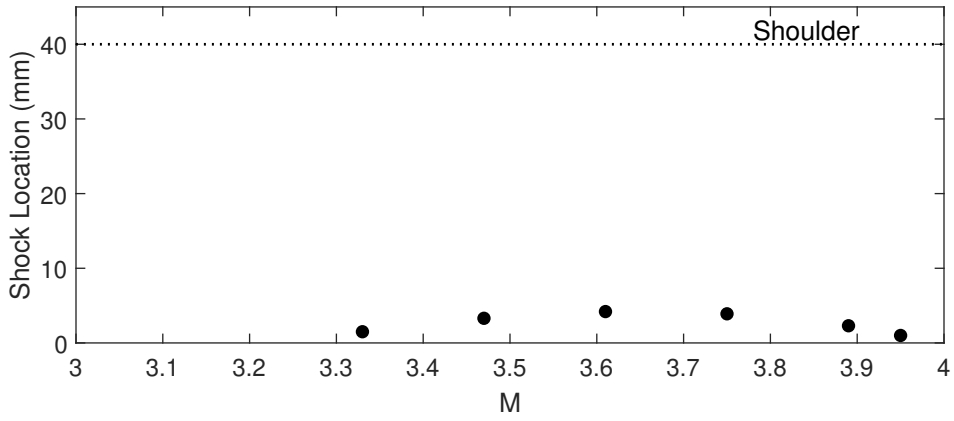

(b)

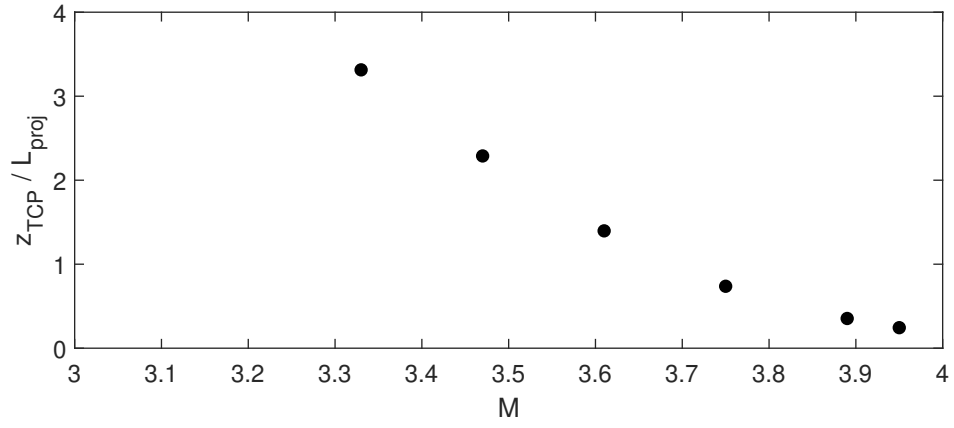

(c)

Fig. 3.17 Non-dimensional thrust (a), shock distance from projectile base (b), and the normalized thermally choked plane location (c) versus Mach number for a P300 projectile in the RTRA 200, using $2.2CH_4 + 2O_2 + 7.52N_2$ propellant.

3.2.4 Operational Envelope Studies

Propellant heat release studies were conducted using the ram PFR model for the three primary ram tubes of interest: the BTRA 500, BTRA 100, and the RTRA 200. These studies led to the creation of new plots depicting the operational envelopes of each tube configuration. Note, all of the following operational envelopes are specific to the P300 projectile, where slight variations would be expected for projectiles with different dimensions.

First, the ram PFR model was used to generate the operational envelope of the BTRA 500. The results, plotted in the *Q*-*M* plane, are shown in Fig. 3.18. There are four distinct boundaries to the operational envelope, detailed in Fig. 3.18a. The minimum Mach number limit is the limit where the normal shock is at the projectile base. For a given propellant heat release, this boundary defines the minimum Mach number required for ram acceleration. Notably, at higher heat releases, the minimum Mach number appears to asymptotically approach the isentropic limit, as defined in Section 1.3.3. Next, the transdetonative transition is the point when the thermally choked plane catches up to the base of the projectile. For a given

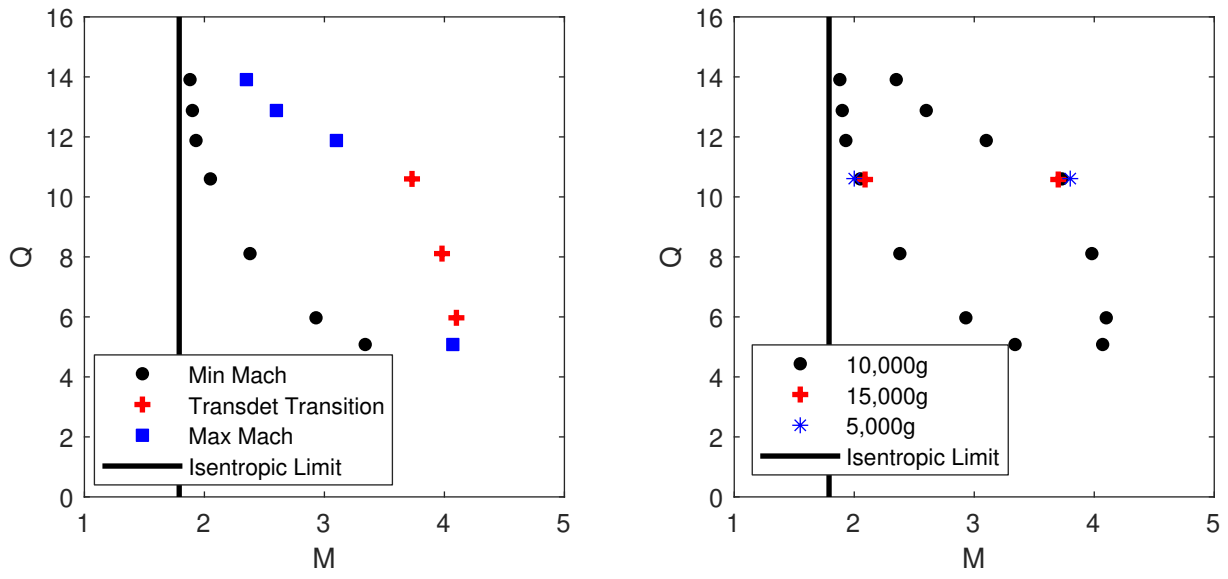

(a) (b)

Fig. 3.18 Operational envelope of the BTRA 500 (a) and the projectile acceleration effects on the operational envelope (b) from the ram accelerator PFR model.

propellant heat release, this boundary defines the Mach number at which the projectile will transition from the thermally choked ram mode to the transdetonative ram mode. The final two boundaries represent maximum Mach number limits for ram operation. The limit at higher propellant heat releases represents the case where the normal shock is pushed forward, past the projectile tail cone. This may or may not lead to an unstart, depending on how effectively the baffles impede the wave motion along the projectile shoulder as intended. The ram PFR model cannot capture this effect so it is left here as a limit. It is expected that operation should extend past this boundary, but the extent by which must be empirically determined. The maximum Mach number limit at lower propellant heat releases represents the wave falloff case, as discussed in Section 1.3.3. This is the case where the normal shock falls off the back of the projectile before the thermally choked plane can catch up and transition to transdetonative operation. This failure would lead to a projectile coasting through the ram tube, ahead of the combustion activity.

It was found that the projectile acceleration can have a measurable affect on ram performance and operability. This was already discussed, in part, in Section 3.2.1. In Fig. 3.18b, the effects of projectile acceleration on the operational envelope are graphically depicted. Here, it is shown that increasing the projectile acceleration causes a constriction in the operational envelope. Higher accelerations raise the minimum required operating Mach number and lower the Mach number of the transdetonative mode transition. This projectile acceleration should effect all the operating limits discussed above in a similar manner.

The BTRA 500 operating envelope produced by the ram PFR model agrees remarkably well with experiments. Figure 3.19 shows BTRA 500 experimental data overlaid on the ram PFR operating envelope. The experimental data is divided into unstarts, starts, and runouts. The unstart data depict the Mach number and heat release at which unstarts occurred upon entry to the ram accelerator. The start data shows the Mach numbers and heat releases where the projectile started upon entry to the ram accelerator. The runout data shows the Mach number and heat release at the exit of a ram accelerator where the projectile left without any form of failure. In all of the experiments, the projectile acceleration was typically 10,000–15,000 g, while the operational envelope is for exactly 10,000 g.

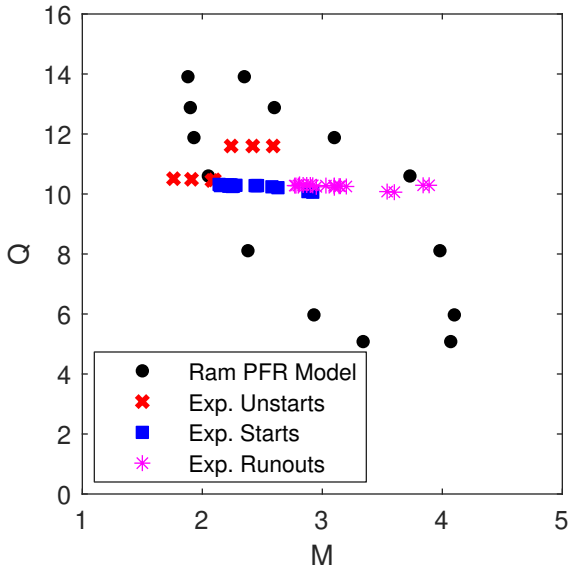

Fig. 3.19 The operational envelope for the BTRA 500 at 10,000 g from the ram PFR model, including experimental data for starts, unstarts, and runouts.

The ram PFR model was able to accurately predict the minimum required Mach number of 2.15 for the BTRA 500 with the propellants used in experiments. This is contrasted with the prior best estimate for minimum operating Mach number of 1.79, provided by the isentropic limit, shown in Fig. 3.18 and discussed in Section 1.3.3. The ram PFR model makes clear the influence that propellant heat release has on this limit, which was not accounted for in the prior estimates. There are additional unstarts within the operational envelope at non-dimensional heat releases around 12. This is in a region of heat releases where the projectile is predicted to encounter an unstart before the transdetonative transition. This may be evidence that operation in this region is inherently more unstable. Since propellants with these heat releases can unstart due to rapid shock transit across the projectile tail cone as Mach numbers increase, it may be that in the truly unsteady operation of the ram accelerator, the localized unstarts that periodically occur during baffle transits may become permanent. This unstart and restart process was depicted schematically in Fig.1.12. If the propellant is too energetic and/or the baffle chambers are too small, the unstarts may never fully recover, which may be what happened in these experiments. The unstarts depicted here warrant caution when trying to operate a ram accelerator in this region in the future.

The projectile runout cases in experiments correlate fairly well with the transdetonative mode transition predicted by the ram PFR model. Figure 3.19 shows projectile runouts for a number of BTRA 500 experiments where the goal was to maximize Mach number. This was done by raising fill pressures and entrance Mach numbers and, ultimately, adding more BTRA stages. In all of these experiments, thrust performance generally decreased as the projectile approached Mach 4, more so than prior theory predicted. Experiments with stronger aluminum projectiles were even used to eliminate concerns over projectile degradation in the tube, but similar results were still achieved. The close correlation with the new results from the ram PFR model now suggest that this may be directly tied to the transition to the transdetonative operating mode. What remains unclear is the nature of this boundary in the BTRA. In SBRA operation, smooth transitions from thermally choked operation to superdetonative operation has been demonstrated [2]. However, with the introduction of baffles obstructing the flow, this transition may not be so smooth in the BTRA. In fact, superdetonative operation in the BTRA may not even be possible. This is still an outstanding question that requires further experiments to be able to confirm the nature of this boundary.

The BTRA 100 operational envelope from the ram PFR model is compared to the the BTRA 500 operational envelope in Fig. 3.20a. The BTRA 100 minimum Mach number limit displays the same asymptotic behavior at high propellant heat releases as the BTRA 500, with the expected lower overall minimum Mach number due to the larger baffle chambers. This showed good correlation to the isentropic limit. However, at lower propellant heat releases, the minimum required Mach number matched that of the BTRA 500 almost exactly. Seemingly, baffle geometry does not have a significant effect on the minimum required Mach number for low heat release propellants. That said, both the transdetonative mode transition and the lower heat release max Mach limit were reduced in the BTRA 100. Additionally, the transition into the region of higher propellant heat releases that encounters the maximum Mach limit occurs at a much lower heat release than the BTRA 500 ($Q = 8$ versus $Q = 11$). This is due to the fact that larger baffle chambers cause the normal shock to sit relatively far up on the projectile tail cone, as discussed in Section 3.2.2, meaning lower heat release propellants may be required to compensate.

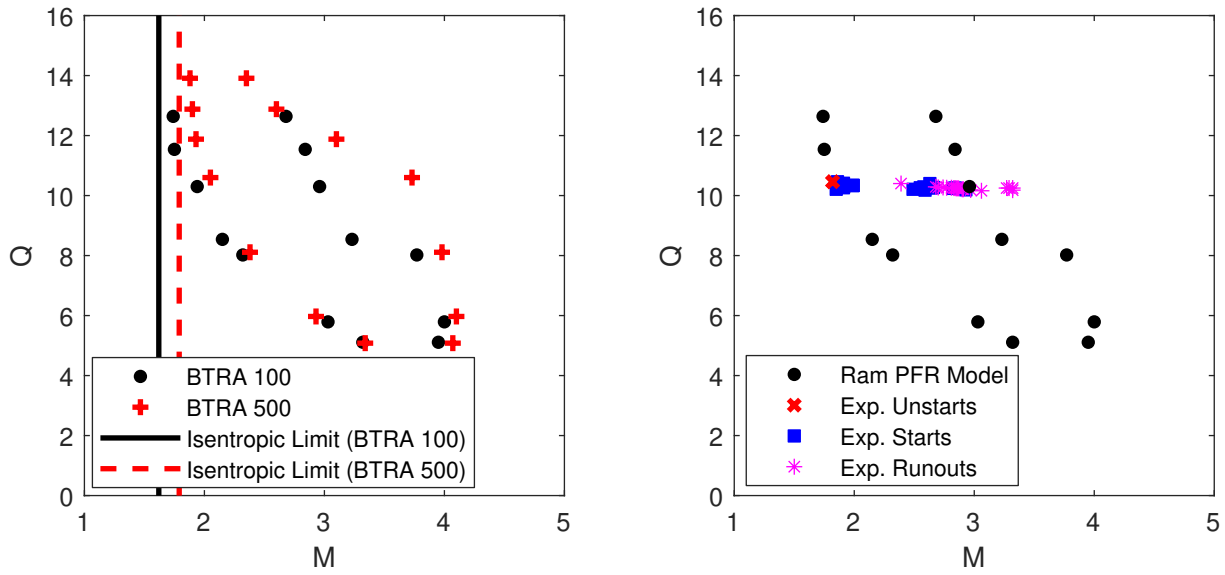

Fig. 3.20 Operational envelope of the BTRA 100 compared to the BTRA 500 from the ram PFR model (a) and comparisons to BTRA 100 experiments, including data for starts, unstarts, and runouts (b).

The operational envelope of the BTRA 100 from the ram PFR model also agrees remarkably well with experiments. Figure 3.20b shows the BTRA 100 operational envelope from the ram PFR model compared to experiments, highlighting the unstarts, starts, and projectile runouts. Once again, the minimum required Mach number is predicted with good accuracy at about 1.85, compared to the isentropic limit prediction of 1.62. Ram starts were demonstrated all the way up to the maximum Mach number limit predicted by the ram PFR model but the projectile runouts went well beyond. Notably, the maximum Mach number runouts occur near where the transdetonative mode transition would occur if the curve was extended to higher heat releases. This suggests two things: first, the BTRA 100 is able to push past the maximum Mach number limit for its propellant. This suggests that the BTRA 100 is better able to prevent or delay unstarts than the BTRA 500. This is likely due to the larger baffle chambers providing more room for recovery from the periodic local unstarts. Second, this is further evidence to support the link between a potential maximum operating Mach number for a BTRA being tied to the transdetonative mode transition, as discussed for the BTRA 500 above. While this may not be any true limit to operation,

it is clear that there are some significant performance effects tied to this transition and it warrants further investigation.

The RTRA 200 operational envelope from the ram PFR model is compared to the the BTRA 500 operational envelope in Fig. 3.21a. The operational envelope was more fully resolved at the low heat releases where the RTRA 200 was experimentally operable. The upper part of the envelope was not completed since it is far outside the range of operable propellants in practical experiments. The boundaries appear similar to the BTRA 500 except at the lowest propellant heat releases, where the RTRA 200 has a more restricted operational envelope and the transdetonative transition is inhibited at a higher heat release. Additionally, the minimum Mach number no longer asymptotically approaches the isentropic limit. This is not much cause for concern as both the asymptotic limit and the isentropic limit correlate to propellant heat releases much higher than have been shown to be operable in experiments. Primarily, this points out that for the RTRA 200, propellant heat release is a significant factor in the minimum required Mach number for operation.

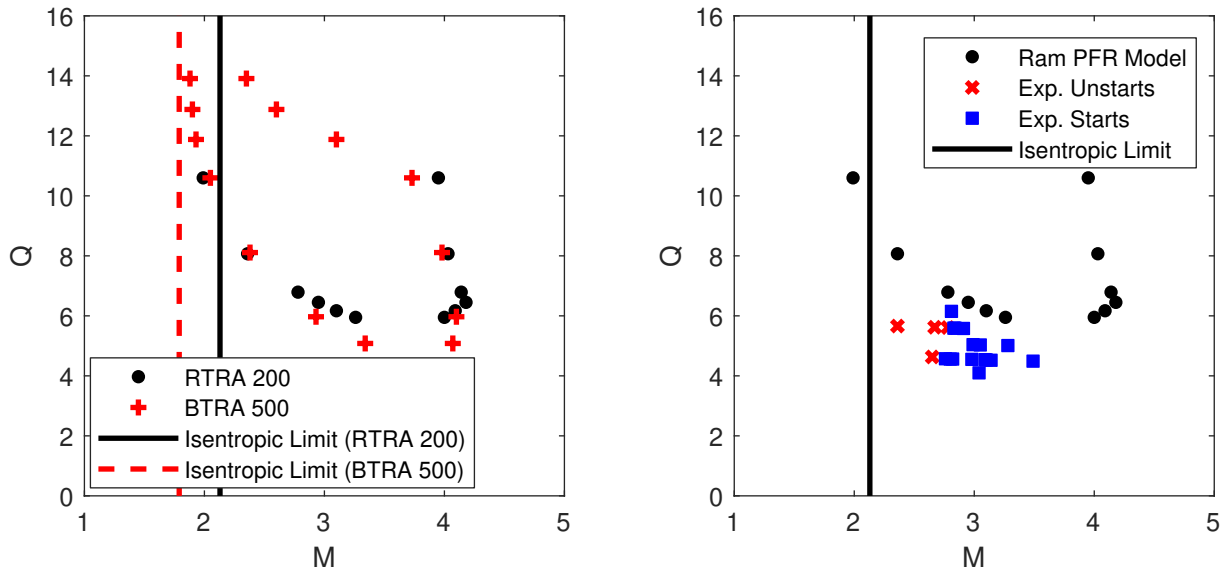

(a) (b)

Fig. 3.21 Operational envelope of the RTRA 200 compared to the BTRA 500 from the ram PFR model (a) and comparisons to RTRA 200 experiments, including data for starts and unstarts (b).

The experimental data for the RTRA 200 does not have very good agreement with the operational envelope produced by the ram PFR model, as shown in Fig. 3.21b. All of the experimental data points, including all starts and unstarts, lie outside the predicted operational envelope. Upon closer analysis, it was found that the propellant heat releases calculated for the ram PFR model in the RTRA 200 had a relatively large disagreement with those predicted by the CV theory. In the RTRA 200, the ram PFR model calculated heat releases that differed from CV theory by up to 30%, whereas in all BTRA simulations, these differences remained below 5%. As discussed in Section 3.2.1, this is due to inaccurate combustion calculations that only occur for fuel-rich propellants in this model. This accounts for the large discrepancy between the ram PFR operational envelope and the RTRA 200 experimental data. Figure 3.22 shows the 'corrected' operational envelope, where the ram PFR model results are plotted with the propellant heat releases from the CV theory predictions. While many of the experimental data points still remain outside the predicted operational envelope, the minimum Mach number predictions now agree much better with the experimental results. The reduced precision in this agreement, compared to the BTRA predictions, can be attributed to the aforementioned heat release discrepancies and their effect on the ram

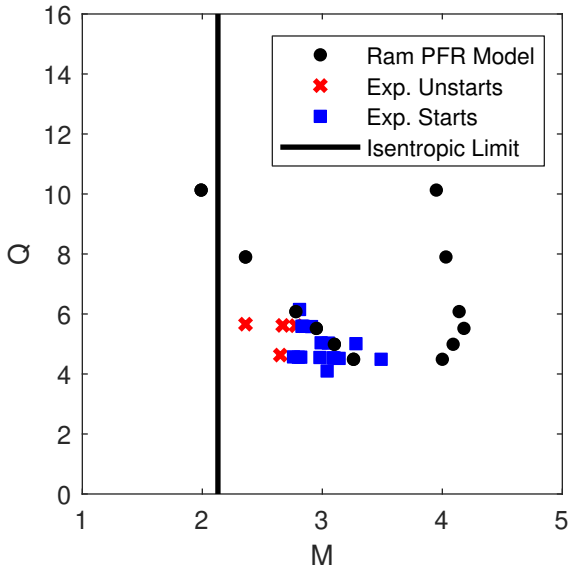

Fig. 3.22 The operational envelope for the RTRA 200 from the ram PFR model using propellant heat releases from CV theory, including experimental data for starts and unstarts.

PFR model results. Regardless, the minimum operational Mach numbers for the RTRA 200 are much more accurately predicted by the ram PFR model than by the isentropic limit.

3.3 Discussion

The ram accelerator PFR model implemented several key, new capabilities for ram accelerator modeling. Most importantly, it included the first implementation of baffle modeling, using a direct physical means of modeling the effects of baffles on ram acceleration instead of a tacked on bluff body drag model. The ram PFR model was also designed to allow the use of actual projectile geometries that match those used in experiments. The ram PFR model included corrections for the non-inertial projectile reference frame that most prior models ignored. The model also included a detailed combustion kinetics model, utilizing the well-developed GRI-Mech 3.0 mechanism for all simulations [12].

The baffle wall model proved to be a vital part of the overall ram PFR model. While the local effects on the flowfield are highlighted in Fig. 3.10, the bulk effects of the baffles throughout the control volume are clearly shown in Fig. 3.14. As implemented in the model, the inclusion of baffles has the net effect of pushing the normal shock further back on the projectile. While this does constrict the range of operable Mach numbers for a given propellant, it allows more energetic propellants to be used without unstarting. This combined effect is what allows the BTRA to operate at much lower Mach numbers than the RTRA or SBRA, as seen in experiments. The good agreement with experiments for both the BTRA 500 and BTRA 100, particularly in the prediction of Mach number limits, serves as good evidence to suggest the baffle wall model was an accurate representation of the net effects of baffles on the ram acceleration. As discussed in Section 3.1.4, the baffle wall model omitted momentum transfer effects from the fluid and only considered local pressure forces on the baffle walls. As discussed, this was done simply to avoid the necessary inclusion of an empirical scaling factor in the model due to its quasi-1D nature. It was anticipated that the momentum component of the force on the baffle wall would have been significant, if included. Since the model agreed so well with experiment without this momentum component, it suggests that it may not be a significant component after all. This has significant physical implications.

If there is no significant momentum exchange between the gas and the baffle walls, the fluid must have very little axial speed in the baffle chambers and the net force on the baffle walls only comes from the static pressure differentials across them. This also means that there will be a significant difference between the core flow velocity (in the center bore) and the flow velocity in the baffle chambers. In effect, this may make a difficult to penetrate barrier in the shear layer between these two regions due to the large velocity differential. This may affect the combustion propagation into the baffle chambers and could be a contributor to the theorized low combustion efficiencies, as discussed in Section 2.7. This is an area of focus that CFD studies may be able to shed more light on.

As alluded to above, the higher propellant heat releases achievable in a BTRA compared to an RTRA are perhaps a more significant driver for the reduced Mach number operation than the flow area differences, as previously thought. This is supported by both the BTRA 500 and BTRA 100 operational envelopes shown in Fig. 3.20a, where the minimum Mach number limits vary significantly with propellant heat releases, especially at lower heat releases. RTRAs and SBRAs typically require $Q < 6$, whereas BTRAs typically operate with Q just above 10. Consequently, the minimum Mach number changes more significantly due to that difference in heat release than it does due to geometry differences. That said, baffle chamber diameters still dominate the minimum Mach number limits between BTRAs that operate with similar propellants. However, as smaller diameter baffle chamber configurations are tested in the future, they will likely require lower heat release propellants that will start to have a significant impact on the minimum operable Mach numbers.

The ram PFR model produced good predictions for the operational envelopes of the BTRA configurations. This was a significant improvement over prior models for the ram accelerator operational envelope, as discussed in Section 1.3.3. The comparisons between ram PFR theory and experiments for both the BTRA 500 and BTRA 100 are shown in Figs. 3.19 and 3.20b, respectively. The minimum Mach numbers for each BTRA were predicted with great accuracy. Given that the baffle wall model and the non-inertial reference frame corrections were both shown to have significant effects on the operating limits, as shown in Figs. 3.14 and 3.15, each of these effects was critical in the accurate prediction of the BTRA operating

limits. While this is good evidence that the baffle wall model was reasonably accurate, as discussed above, it serves as new evidence to suggest that the effects of the non-inertial reference frame are significant in the calculation of the ram accelerator operating limits. The inertial effects were shown to be negligible in the thrust calculations of the control volume theory by Bruckner et al. [30], but this was never shown for the 1D ram flowfield models. This discrepancy can at least partially explain why the theoretical operational envelopes produced by prior models failed to match experiments so significantly.

The large discrepancies between the fuel-rich propellant heat releases predicted by the ram PFR model and the CV theory warrant further investigation. While largely irrelevant for BTRA modeling, since stoichiometric propellants can be used, fuel-rich propellants are typically used in the RTRA and cannot be ignored. Other reaction mechanisms, beyond the GRI-Mech 3.0, can be implemented in the ram PFR model for a comparison of results. In particular, the reduced kinetics mechanism developed by Petersen and Hanson [42] would be of interest since it was developed specifically for the ram accelerator. It was not chosen for this initial study due to its more limited propellant options. The Petersen mechanism, or another reduced mechanism, may also have the benefit of reducing the total computation time of the ram PFR model.

As it stands, the ram PFR model can continue to be used to explore new BTRA and RTRA configurations as well as different projectile and propellant combinations. However, there are many avenues for further development of the ram PFR model. After identifying the significance of including the non-inertial reference frame corrections, the ram PFR model could be modified to utilize the correction in the generalized convergence criterion, Eq. (3.49), as discussed in Section 3.1.5. It would then be a natural extension to generalize a little further and allow for transdetonative mode solutions. This may help shed some light on the apparent boundary found in experiments near the transdetonative mode transition in the BTRA. Additionally, the ram PFR model could be modified to account for real gas effects, which have previously been shown to be a significant factor in ram operation, especially at higher projectile accelerations. Regardless, the ram PFR model should remain a valuable tool for ram performance modeling and aid significantly in the development of new ram accelerator configurations.

Chapter 4

Conclusion

New experiments in the BTRA led to an improved understanding on how BTRA design impacts ram accelerator operation and performance. Smaller baffle chamber diameters produce more thrust and operate more efficiently, while larger baffle chamber diameters allow for operation at lower Mach numbers. The BTRA has now been demonstrated to operate at as low as Mach 1.85. To date, all BTRAs have achieved significantly lower thrust than existing theory has predicted. The new BTRA results support the theory that combustion efficiency may be a significant performance factor. There is evidence to suggest that pockets of unburned propellant may remain in the baffle chambers well after the projectile has passed, causing less energy to be released and transferred to the projectile. Smaller diameter baffle chambers should continue to reduce this inefficiency and higher performance BTRA operation should be achievable.

The RTRA was developed and tested, achieving relatively high thrust and efficiency, much higher than any BTRA configuration. This came with the requirement of higher minimum Mach numbers and lower propellant heat releases.

The new ram accelerator configuration called the RTRA with sweeper baffles was developed and successfully tested. This hybrid ram tube configuration features periodically spaced sections of baffles throughout a railed tube. The RTRA with sweeper baffles was shown to allow the operation of much more energetic propellants in an RTRA and delay unstarts. An optimized version of this configuration

should be able to significantly improve the thrust and efficiency of an RTRA, while also expanding its operational envelope with more stable operation.

A new ram accelerator starting technology was developed, called the BSS. The BSS features a short section of baffles filled with a carefully tuned propellant, allowing a full-bore projectile to enter and affect a ram start as it passes through the BSS and into a primary ram stage. This is all achieved without the use of an obturator, which is typically required to start all ram accelerators. This was proven to be a viable technology in initial testing and will prove to be a critical technology in the eventual commercialization of the ram accelerator.

The ram accelerator PFR model proved to be a significant advancement in the modeling of ram accelerator operation. It included the critical additions of baffled tube modeling and accommodations for real projectile geometries from experiments. It also added new corrections for the non-inertial projectile reference frame, which had a significant effect on the results. The most significant advantage of the new ram PFR model was its ability to model the operational envelope of BTRAs with high accuracy. This model led to new insights on the importance of non-inertial reference frame corrections in the calculation of ram accelerator operating limits and elucidated the significant dependence of the minimum Mach number limit on the propellant heat release. The ram PFR model should serve as a valuable tool in the design and development of future ram accelerator configurations.

References

[1] Hertzberg, A., Bruckner, A. P., and Bogdanoff, D. W., "Ram Accelerator: A New Chemical Method for Accelerating Projectiles to Ultrahigh Velocities," *AIAA Journal*, Vol. 26, No. 2, 1988, pp. 195–203. https://doi.org/10.2514/3.9872.

[2] Hertzberg, A., Bruckner, A. P., and Knowlen, C., "Experimental investigation of ram accelerator propulsion modes," *Shock Waves*, Vol. 1, 1991, pp. 17–25. https://doi.org/10.1007/BF01414864.

[3] Kaloupis, P., and Bruckner, A. P., "The Ram Accelerator: A Chemically Driven Mass Launcher," *AIAA Paper 1988–2968*, July 1988. https://doi.org/10.2514/6.1988-2968.

[4] Bogdanoff, D. W., "Ram Accelerator Direct Space Launch System: New Concepts," *Journal of Propulsion and Power*, Vol. 8, No. 2, 1992, pp. 481–490. https://doi.org/10.2514/3.23502.

[5] Knowlen, C., and Bruckner, A. P., "Direct Space Launch Using Ram Accelerator Technology," *AIP Conference Proceedings 552*, 2001, pp. 583–588. https://doi.org/10.1063/1.1357980.

[6] Strawa, A. W., Chapman, G. T., Canning, T. N., and Arnold, J. O., "Ballistic Range and Aerothermodynamic Testing," *Journal of Aircraft*, 1991, pp. 443–449. https://doi.org/10.2514/3.46047.

[7] Naumann, K. W., and Bruckner, A. P., "Ram Accelerator Ballistic Range Concept for Softly Accelerating Hypersonic Free-Flying Models," *Journal of Aircraft*, 1994, pp. 1310–1316. https://doi.org/10.2514/3.46652.

[8] Russel, M. C., "Ram Accelerator System," U.S. Patent 9,500,419 B2, issued 22 Nov. 2016.

[9] Cengel, Y. A., and Boles, M. A., *Thermodynamics: An Engineering Approach*, 7th ed., McGraw-Hill, New York, 2011.

[10] Higgins, A. J., "Ram Accelerators: Outstanding Issues and New Directions," *Journal of Propulsion and Power*, 2006, pp. 1170–1187. https://doi.org/10.2514/1.18209.

[11] Knowlen, C., and Bruckner, A. P., "Hugoniot analysis of the ram accelerator," *Shock Waves*, edited by K. Takayama, Springer, Berlin, Heidelberg, 1992, pp. 617–622. https://doi.org/10.1007/978-3-642-77648-9_97.

[12] Smith, G. P., Golden, D. M., Frenklach, M., Moriarty, N. W., Eiteneer, B., Goldenberg, M., Bowman, C. T., Hanson, R. K., Song, S., Gardiner Jr., W. C., Lissianski, V. V., and Qin, Z., "GRI-Mech 3.0," *Gas Research Institute*, 2000. URL http://combustion.berkeley.edu/gri-mech/version30/text30.html.

[13] Goodwin, D. G., Speth, R. L., Moffat, H. K., and Weber, B. W., "Cantera: An Object-oriented Software Toolkit for Chemical Kinetics, Thermodynamics, and Transport Processes," Version 2.5.1, 2021. https://doi.org/10.5281/zenodo.4527812, URL https://www.cantera.org.

[14] Higgins, A. J., Knowlen, C., and Bruckner, A. P., "Ram Accelerator Operating Limits, Part 1: Identification of Limits," *Journal of Propulsion and Power*, Vol. 14, No. 6, 1998, pp. 951–958. https://doi.org/10.2514/2.5359.

[15] Higgins, A. J., Knowlen, C., and Bruckner, A. P., "Ram Accelerator Operating Limits, Part 2: Nature of Observed Limits," *Journal of Propulsion and Power*, Vol. 14, No. 6, 1998, pp. 959–966. https://doi.org/10.2514/2.5360.

[16] Kantrowitz, A., and Donaldson, C. d., "Preliminary Investigation of Supersonic Diffusers," Tech. rep., NACA, ACR No. L5D20, 1945.

[17] Liepmann, H. W., and Roshko, A., *Elements of Gasdynamics*, Dover Publications, Inc., New York, 2001. Republication of the work published by John Wiley & Sons, Inc., New York, 1957.

[18] Burnham, E. A., "Investigation of Starting and Ignition Transients in the Thermally Choked Ram Accelerator," Ph.D. thesis, University of Washington, Seattle, WA, 1993.

[19] Schultz, E., Knowlen, C., and Bruckner, A. P., "Obturator and detonation experiments in the subdetonative ram accelerator," *Shock Waves*, Vol. 9, 1999, pp. 181–191. https://doi.org/10.1007/s001930050153.

[20] Schultz, E., Knowlen, C., and Bruckner, A. P., "Starting Envelope of the Subdetonative Ram Accelerator," *Journal of Propulsion and Power*, Vol. 16, No. 6, 2000, pp. 1040–1052. https://doi.org/10.2514/2.5674.

[21] Bundy, C., Knowlen, C., and Bruckner, A. P., "Unsteady Effects on Ram Accelerator Operation at Elevated Fill Pressures," *Journal of Propulsion and Power*, Vol. 20, No. 5, 2004, pp. 801–810. https://doi.org/10.2514/1.12550.

[22] Takayama, K., and Sasoh, A. (eds.), *Ram Accelerators*, Springer-Verlag, Berlin, 1998.

[23] Higgins, A. J., Knowlen, C., and Kiyanda, C. B., "Gasdynamic Operation of Baffled Tube Ram Accelerator in Highly Energetic Mixtures," *Proceedings of the 20th International Colloquium on the Dynamics of Explosions and Reactive Systems, Paper 178*, 2005.

[24] Knowlen, C., Glusman, J. F., Grist, R., Bruckner, A. P., and Higgins, A. J., "Experimental Investigation of a Baffled-Tube Ram Accelerator," *AIAA Paper 2016–4813*, July 2016. https://doi.org/10.2514/6.2016-4813.

[25] Knowlen, C., Byrd, T., Dumas, J., Daneshvaran, N., Glusman, J., Bruckner, A. P., and Higgins, A. J., "Baffled-Tube Ram Accelerator Operation with Inclined Baffles," *AIAA Paper 2017–4959*, July 2017. https://doi.org/10.2514/6.2017-4959.

[26] Daneshvaran, N., and Knowlen, C., "Transient Computational Fluid Dynamic Modeling of Baffled Tube Ram Accelerator," *AIAA Paper 2017–0119*, January 2017. https://doi.org/10.2514/6.2017-0119.

[27] Knowlen, C., Daneshvaran, N., Byrd, T., and Dumas, J., "Computational Fluid Dynamic Modeling of Baffled Tube Ram Accelerator Experiments," *AIAA Paper 2018–1417*, January 2018. https://doi.org/10.2514/6.2018-1417.

[28] Gu, L. S., Knystautas, R., and Lee, J. H., "Influence of Obstacle Spacing on the Propagation of Quasidetonation," *Dynamics of Explosions*, edited by A. Kuhl, J. Bowen, J. Leyer, and A. Borisov, Progress in Astronautics and Aeronautics, AIAA, 1988, pp. 232–247. https://doi.org/10.2514/5.9781600865886.0232.0247.

[29] Seiler, F., Patz, G., Smeets, G., and Srulijes, J., "Progress of ram acceleration with ISL's RAMAC 30," *J. Phys. IV France*, Vol. 10, No. PR11, 2000, pp. Pr11–31–Pr11–40. https://doi.org/10.1051/jp4:20001104.

[30] Bruckner, A. P., Knowlen, C., Hertzberg, A., and Bogdanoff, D. W., "Operational Characteristics of the Thermally Choked Ram Accelerator," *Journal of Propulsion and Power*, Vol. 7, No. 5, 1991, pp. 828–836. https://doi.org/10.2514/3.23398.

[31] Bauer, P., Knowlen, C., and Bruckner, A., "Real gas effects on the prediction of ram accelerator performance," *Shock Waves*, Vol. 8, 1998, pp. 113–118. https://doi.org/10.1007/s001930050104.

[32] Knowlen, C., Bauer, P., Bengherbia, T., Yao, Y. F., Bruckner, A. P., and Giraud, M., "Unsteady 1-D Thrust Modeling with EOS Effects for Ram Accelerator Experiments at Different Bores," *Aerotecnica Missili & Spazio*, Vol. 97, 2018, pp. 19–26. https://doi.org/10.1007/BF03404761.

[33] Bruckner, A. P., "The ram accelerator: overview and state of the art," *Ram Accelerators*, edited by K. Takayama and A. Sasoh, Springer-Verlag, Berlin, 1998, pp. 3–23.

[34] Bogdanoff, D. W., Knowlen, C., Murakami, D., and Stonich, I., "Magnetic Detection for Projectiles in Tubes," *AIAA Journal*, Vol. 28, No. 11, 1990, pp. 1942–1944. https://doi.org/10.2514/3.10502.

[35] Knowlen, C., "Theoretical and Experimental Investigation of the Thermodynamics of the Thermally Choked Ram Accelerator," Ph.D. thesis, University of Washington, Seattle, WA, 1991.

[36] Leege, B. J., Daneshvaran, N., Donkelaar, F. v., Liu, S., Knowlen, C., and Higgins, A., "Ram Accelerator Operation in Railed and Baffled Tubes," *AIAA Paper 2020–3516*, August 2020. https://doi.org/10.2514/6.2020-3516.

[37] Leege, B. J., Smith, C., Knowlen, C., and Higgins, A., "Baffled Tube Ram Accelerator Operation with Normal Baffles," *AIAA Paper 2022–2071*, January 2022. https://doi.org/10.2514/6.2022-2071.

[38] Sasoh, A., Maemura, J., Hirakata, S., Takayama, K., and Falcovitz, J., "Diaphragm rupture. Impingement by a conically-nosed, ram-accelerator projectile," *Shock Waves*, Vol. 9, 1999, pp. 19–30. https://doi.org/10.1007/s001930050135.

[39] Sasoh, A., and Knowlen, C., "Ram Accelerator Operation Analysis in Thermally Choked and Transdetonative Propulsive Modes," *Transactions of The Japan Society for Aeronautical and Space Sciences*, Vol. 40, 1997, pp. 130–148.

[40] Turns, S. R., "Coupling Chemical and Thermal Analyses of Reacting Systems," *An Introduction to Combustion: Concepts and Applications*, 3rd ed., McGraw Hill Education (India) Private Limited, Chennai, 2012, Chap. 6, pp. 183–219.

[41] MATLAB, *version 9.8.0.1323502 (R2020a)*, The MathWorks Inc., Natick, Massachusetts, 2020.

[42] Petersen, E. L., and Hanson, R. K., "Reduced Kinetics Mechanisms for Ram Accelerator Combustion," *Journal of Propulsion and Power*, Vol. 15, No. 4, 1999, pp. 591–600. https://doi.org/10.2514/2.5468.

[43] "Solve stiff differential equations and DAEs–variable order method - MATLAB ode15s," MathWorks, Accessed Apr. 27, 2022. URL https://www.mathworks.com/help/matlab/ref/ode15s.html.

[44] "Equations, Tables, and Charts for Compressible Flow," , NACA Rept. 1135, 1953.

Appendix

A.1 Ram PFR Model Solver (ramPFR_v2.m)

```
function [rho2,T2,Y2,cp2,R2,P2,u2,cv2,gamma2,s2,a2,h2,M2,u2_lab,M2_lab,Tt2,
    Pt2,rhot2,ht2,F_proj,F_wall,F_i,W_dot_i,mdot2,q,tr,p_cell_type,z_tcp,
    t_avg] = ramPFR_v2(n_divs,gas,Y,P,T,A1,A2,L,mdot,u,CI,rho,ap,up,Ac,cp,V,
    combustion)
%ramPFR_v2 Solves the ram accelerator flow field using a plug flow reactor
%model.
%   Uses a plug flow reactor model with Cantera chemical kinetics models to
%   solve the ram flowfield with or without combustion.

set(gas,'Temperature',T,'Pressure',P,'MassFractions',Y); % Set the inlet gas
     state
nsp = nSpecies(gas); % Number of species in model
h = enthalpy_mass(gas); % Enthalpy at inlet [J/kg]

% Assume that area change is linear with distance (reasonable over the
    length of a single cell)
dAdz = (A2-A1)/L; % Set dA/dz derivative [m]
dz = L/n_divs; % Set dz (total p_cell length divided by total divisions (
    extra combustion cells) [m]

z = 0:dz:L; % Set distance array [m]
z_tcp = 0; % Set tcp location to zero (will replace with a value if tcp is
    reached) [m]

Acv_star = Ac - 1/3*(2*Ac-A1-A2+sqrt((Ac-A1)*(Ac-A2))); % Effective CV x-
    sect area (eq 19)[m^2]
% Note: Acv_star is the average value for the entire "cell" (p_cell) in
% which the intergration is performed and is roughly constant for small
```

```
% cells.

% Initialize solution arrays
rho_soln = zeros(length(z),1); % Density [m/s]
T_soln = zeros(length(z),1); % Temperature [K]
Y_soln = zeros(length(z),nsp); % Mass fractions [kg/kg]
tr_soln = zeros(length(z),1); % Residence time [s]

A = zeros(length(z),1); % Area [m^2]
R = zeros(length(z),1); % Specific gas constant [J/kg*K]

% Initialize solution
rho_soln(1) = rho; % Initial density [m/s]
T_soln(1) = T; % Initial temperature [K]
Y_soln(1,:) = Y'; % Initial mass fractions [kg/kg]
tr_soln(1) = 0; % Initial residence time [s]
A(1) = A1; % Initial area [m^2]
R(1) = gasconstant()/meanMolecularWeight(gas); % Initial specific gas
    constant [J/kg*K]

% Set ode solver settings
options = odeset('RelTol',1e-6,'AbsTol',1e-10);

for n = 2:length(z)
    % Set solution format to [u,T,Y]
    inlet_soln(1) = rho_soln(n-1);
    inlet_soln(2) = T_soln(n-1);
    inlet_soln(3:nsp+2) = Y_soln(n-1,:);
    inlet_soln(nsp+3) = tr_soln(n-1); % Initial residence time [s]
    limits = [z(n-1) z(n)]; % Set integration limits (z distances)

    % Using ode15s solver, "stiff" solver since variables in the solution
        have large differences in magnitudes
    [t_temp,F] = ode15s(@ramPFR_solver_v2,limits,inlet_soln,options,gas,CI,
        ap,up,Acv_star,mdot,cp(n-1),P(n-1),A1,u(n-1),dAdz,nsp,combustion);

    % Can use sol = ode15s(...) to get the solutions at each step - do this
    % to repeat the n step when M_check > 1 to pull out the exact TCP data
    % (more exact - utilizing the sub-integration steps)

    t(1:length(t_temp),n) = t_temp;
    t_length(n) = length(t_temp); % Number of integration steps in the
        current cell subdivision [-]
```

```
    rho_soln(n) = F(end,1); % New density [m/s]
    T_soln(n) = F(end,2); % New temperature [K]
    Y_soln(n,:) = F(end,3:nsp+2); % New mass fractions [kg/kg]
    tr_soln(n) = F(end,nsp+3); % New residence time [s]

    % Calculate all properties used in the solution for the next iteration
    set(gas,'Temperature',T_soln(n),'Density',rho_soln(n),'MassFractions',
        Y_soln(n,:)); % Set new gas state
    cp(n) = cp_mass(gas); % Specific heat at constant pressure [J/kg*K]
    R(n) = gasconstant()/meanMolecularWeight(gas); % Specific gas constant [
        J/kg*K]
    P(n) = rho_soln(n)*R(n)*T_soln(n); % Pressure (by ideal gas law) [Pa]
    A(n) = A1 + dAdz*limits(end); % Area [m^2]
    u(n) = mdot/(rho_soln(n)*A(n)); % Velocity (by continuity) [m/s]
    ss_check = soundspeed(gas); % Sound speed [m/s] (only used for Mach
        check)
    M_check = u(n)/ss_check; % Mach number [—] (used for TCP check)

    if combustion == true && M_check > 1 % Stop iteration when Mach 1 (TCP)
        is reached
        % Truncate solution arrays (get rid of zeros at the end)
        rho_soln(n+1:end) = [];
        T_soln(n+1:end) = [];
        Y_soln(n+1:end,:) = [];
        tr_soln(n+1:end) = [];
        A(n+1:end) = [];
        R(n+1:end) = [];

        % Set TCP z location
        z_tcp = z(n); % Set current z location as the TCP [m]

        break; % End loop (saving current values as the final values)

    end

end

% Define all the final values (for function output)
rho2 = rho_soln(end); % Density [kg/m^3]
T2 = T_soln(end); % Temperature [K]
Y2 = Y_soln(end,:)'; % Mass fractions [kg/kg]
cp2 = cp(end); % Specific heat at constant pressure [J/kg*K]
```

```
R2 = R(end); % Specific gas constant [J/kg*K]
P2 = P(end); % Pressure [Pa]
u2 = u(end); % Velocity [m/s]
tr = tr_soln(end);

% Calculate all other properties of interest
cv2 = cv_mass(gas); % Specific heat at constant volume [J/kg*K]
gamma2 = cp2/cv2; % Specific heat ratio [-]
s2 = entropy_mass(gas); % Entropy [J/kg*K]
a2 = soundspeed(gas); % Sound speed [m/s]
h2 = enthalpy_mass(gas); % Enthalpy [J/kg]
M2 = u2/a2; % Mach [-]
u2_lab = up - u2; % Relative velocity of the fluid w.r.t. the projectile/
    wall [m/s] (fluid velocity in lab frame)
M2_lab = abs(u2_lab)/a2; % Mach # of fluid w.r.t. the projectile/wall [-] (
    fluid mach in lab frame)
Tt2 = T2*(1+(gamma2-1)/2*M2^2); % Total temperature (isentropic relation)[K]
Pt2 = P2*(1+(gamma2-1)/2*M2^2)^(gamma2/(gamma2-1)); % Total pressure (
    isentropic relation)[Pa]
rhot2 = rho2*(1+(gamma2-1)/2*M2^2)^(1/(gamma2-1)); % Total density (
    isentropic relation)[kg/m^3]
ht2 = h2 + u2^2/2; % Total enthalpy [J/kg]
F_proj = (P(1)+P2)/2*(A2-A1); % Force on projectile [N]
F_wall = 0; % Force on baffle wall (always zero in this model) [N]
F_i = -CI*(rho(1)+rho2)/2*V*ap; % Inertial force on the cell (negative z
    direction - in original model coordinate system) (Eq 2)[N]
W_dot_i = CI*(rho(1)+rho2)/2*V*ap*up; % Power input due to inertial forces (
    Eq 6)[W]
mdot2 = mdot; % Mass flow rate (held constant) [kg/s]
q = -(h2 - h - (cp(1)+cp2)/2*(T2-T)); % Heat released in cell [J/kg] (=
    enthalpy change - sensible enthalpy change, neg sign to make positive)
p_cell_type = 20; % Set cell type to PFR

t_avg = mean(t_length(2:end)); % Average number of integration steps per
    cell subdivision [-]

end
```

A.2 Ram PFR ODEs (ramPFR_solver_v2.m)

```
function [F] = ramPFR_solver_v2(z,inlet_soln,gas,CI,ap,up,Acv_star,mdot,cp,P
    ,A1,u,dAdz,nsp,combustion)
%ramPFR_solver_v2 Solves the system of ODEs for the ramPFR_v2 model.
%   When used in the ramPFR function, in conjuction with the ode15s solver,
%   provides solutions to the system of 2+nsp ODEs in the format of
%   F = [rho;T;Y].

% Pull initial values for rho, T, and Y from inlet_soln
rho = inlet_soln(1); % Density [kg/m^3]
T = inlet_soln(2); % Temperature [K]
Y = inlet_soln(3:nsp+2); % Mass fractions

% Set area for the current integration location
A = A1 + dAdz*z; % Area [m^2]

set(gas,'Temperature',T,'Density',rho,'MassFractions',Y); % Set gas state
nsp = nSpecies(gas); % Number of species in the gas model [—]

% Calculate properties based on the current gas state (using Cantera)
MWi = molecularWeights(gas); % Species molecular weights [kg/kmol]
hi = enthalpies_RT(gas)*T*gasconstant()./MWi; % Species enthalpies [J/kg]

if combustion == true % Combustion in cell
    omega_dot_i = netProdRates(gas).*MWi; % Species net mass production
        rates [kg/m^3*s]
elseif combustion == false % No combustion in cell
    omega_dot_i = MWi*0; % No change in species
else
    error('This should not have happened :(')
end

MWmix = meanMolecularWeight(gas); % Molecular weight of the gas [kg/kmol]

% Define the PFR differential equations for rho, T, and Y in the format
% F = [drho/dz,dT/dz,dY/dz].

% drho/dz (eq 33)
```

```
F(1) = (CI*rho*ap*Acv_star*(up/(mdot*cp*T)-1/(P*A)) + 1/(rho*u)*sum(
   omega_dot_i.*(MWmix./MWi-hi./(cp*T))) + u^2/A*(1/(cp*T)-rho/P)*dAdz) / (u
   ^2/P - u^2/(rho*cp*T) - 1/rho);

% dT/dz (eq 34)
F(2) = CI*rho*ap*up*Acv_star/(mdot*cp) - 1/(rho*u*cp)*sum(hi.*omega_dot_i) +
    u^2/cp*(1/rho*F(1) + 1/A*dAdz);

% dYi/dz (eq 28)
F(3:nsp+2) = omega_dot_i/(rho*u);

% dtr/dz (tr: residence time)
F(nsp+3) = 1/u;

% Flip the solution into a single column vector (required for ode15s)
F = F';

end
```

A.3 Projectile Base Area Change Model (base_area_change.m)

```
function [P2,T2,rho2,u2,h2,R2,M2,s2,cp2,cv2,gamma2,a2,u_lab2,M_lab2,mdot2,
   Tt2,Pt2,rhot2,ht2,F_proj_base] = base_area_change(R1,T1,rho1,u1,P1,A1,A2,
   h1,gas,Y,WBL,u_proj)
%base_area_change Calculates the effect of the base area change on the flow
%field.
%   Assumes a zero volume cell for an instantaneous area change at the
%   projectile base. Used to calculate the base pressure and force on
%   projectile. Results should be passed to the PFR model to calculate the
%   chemistry changes for the actual cell behind the projectile.

R2 = R1; % Gas constant (no change in this cell) [J/kg*K]
% Assume T2, then solve system and iterate until convergence
kk = 2; % Initialize index for convergence loop
nn = 1; % Initialize increment modifier
nnn = 1; % Initialize increment modifier
T_guess = T1; % Guess as the temperature at the previous cell [K]
CoE_residual = 10; % Initialize CoE residual [J/kg]
CoE_conv = 1e-6; % Set CoE convergence criteria [J/kg]
CoE_RHS = 1; % Initialize RHS
% Iterate until CoE converges
while abs(CoE_residual(kk-1)/CoE_RHS)>CoE_conv
    if kk == 2 % If the first iteration
        T_guess(kk) = T_guess(kk-1); % Temperature [K]
        T_up(kk) = false; % Indicates if temp is raised for this iteration

    elseif CoE_residual(kk-1) > 0 % Lower T_guess to reduce residual
        T_up(kk) = false; % Indicates if temp is raised for this iteration
        if T_up(kk-1) % If last temp change was an increase (decrease by a
           smaller increment)
            T_mod(kk) = (1-0.0001*1/nn); % Modifier for T_guess [-]
            T_guess(kk) = T_guess(kk-1)*T_mod(kk); % Temperature [K]
            if nn > 200 % If iterations get high, decrease the step change
               size to speed up convergence
                nn = nn + 20;
            elseif nn > 100
                nn = nn + 10;
            else % Increment normally
                nn = nn + 3; % Increment the increment modifier to produce a
                    smaller step next time
```

```
        end
        nnn = 1; % Reset nnn to 1
    else % If last temp change was a decrease (continue at same change
        size until sign change in residual)
        if nnn > 5 % If the last some# iterations did not change step
            size
            T_mod(kk) = (1-0.0001*1/nn*nnn/3); % Increase the step size
                (temporarily)
        else
            % Normal T_mod
            T_mod(kk) = (1-0.0001*1/nn); % Modifier for T_guess [-]
        end
        T_guess(kk) = T_guess(kk-1)*T_mod(kk); % Temperature [K]
        % Do not increment nn (keep same step size)
        nnn = nnn + 1; % Increment nnn (to track sequential steps at
            same step size
    end

elseif CoE_residual(kk-1) < 0 % Higher T_guess to increase residual
    T_up(kk) = true; % Indicates if temp is raised for this iteration
    if T_up(kk-1) % If last temp change was an increase (continue at
        same change size until sign change in residual)
        if nnn > 5 % If the last some# iterations did not change step
            size
            T_mod(kk) = (1+0.0001*1/nn*nnn/3); % Increase the step size
                (temporarily)
        else
            % Normal T_mod
            T_mod(kk) = (1+0.0001*1/nn); % Modifier for T_guess [-]
        end
        T_guess(kk) = T_guess(kk-1)*T_mod(kk); % Temperature [K]
        % Do not increment nn (keep same step size)
        nnn = nnn + 1; % Increment nnn (to track sequential steps at
            same step size
    else % If last temp change was a decrease (increase by a smaller
        increment)
        T_mod(kk) = (1+0.0001*1/nn); % Modifier for T_guess [-]
        T_guess(kk) = T_guess(kk-1)*T_mod(kk); % Temperature [K]
        if nn > 200 % If iterations get high, decrease the step change
            size to speed up convergence
            nn = nn + 20;
        elseif nn > 100
            nn = nn + 10;
```

```
            else % Increment normally
                nn = nn + 3; % Increment the increment modifier to produce a
                    smaller step next time
            end
            nnn = 1; % Reset nnn to 1
        end

    end
    T2 = T_guess(end); % Set T to the final guess
    quad_A = rho1*u1; % Coefficient A in quadratic equation
    quad_B = -(rho1*u1^2+P1); % Coefficient B in quadratic equation
    quad_C = rho1*u1*A1/A2*R2*T2; % Coefficient C in quadratic equation
    quad_soln = roots([quad_A quad_B quad_C]); % Solve quadratic equation
       for u2 (eq 7) [m/s]

    if isempty(quad_soln) % If no solution to quad eq
        error('No solution to quadratic equation')
    end

    % Velocity should be the lower of the two (since subsonic expansion
    % decreases velocity)
    u2 = min(quad_soln); % Set u to the lower value of the solution [m/s]
    if ~isreal(u2) % If the solution is complex, it is not valid
        u2 = max(quad_soln); % Try other solution for u [m/s]
        if ~isreal(u2) % If both solutions are complex
            error('No real solution to quad equation for u2')
        end
    end

    P2 = rho1*u1*A1*R2*T2/(u2*A2); % Pressure (eq 6) [Pa]
    rho2 = P2/(R2*T2); % Density (eq 5) [kg/m^3]

    set(gas,'Temperature',T2,'Pressure',P2,'MassFractions',Y); % Set gas
       state
    h2 = enthalpy_mass(gas); % Enthalpy of gas [J/kg]

    CoE_LHS = h1 + u1^2/2 - WBL; % LHS of CoE (eq 4) [J/kg]
    CoE_RHS = h2 + u2^2/2; % RHS of CoE (eq 4) [J/kg]
    CoE_residual(kk) = CoE_RHS-CoE_LHS; % Residual of the CoE equation (eq
       4) [J/kg]

    kk = kk + 1;
end
```

```
if u2 < 0 % If u is negative
    error('Negative u') % Display error if u is found to be negative
end

% Gas state is already set from h calc in the convergence loop
s2 = entropy_mass(gas); % Entropy [J/kg*K]
cp2 = cp_mass(gas); % Specific heat at constant pressure [J/kg*K]
cv2 = cv_mass(gas); % Specific heat at constant volume [J/kg*K]
gamma2 = cp2/cv2; % Specific heat ratio [-]
a2 = soundspeed(gas); % Sound speed [m/s]

M2 = u2/a2; % Mach [-]
u_lab2 = u_proj - u2; % Relative velocity of the fluid w.r.t. the projectile
   /wall [m/s] (fluid velocity in lab frame)
M_lab2 = abs(u_lab2/a2); % Mach # of fluid w.r.t. the projectile/wall [-] (
   fluid mach in lab frame)
mdot2 = rho2*u2*A2; % Mass flow rate (Eq 1)[kg/s]
Tt2 = T2*(1+(gamma2-1)/2*M2^2); % Total temperature [K]
Pt2 = P2*(1+(gamma2-1)/2*M2^2)^(gamma2/(gamma2-1)); % Total pressure in cell
    (isentropic relation)[Pa]
rhot2 = rho2*(1+(gamma2-1)/2*M2^2)^(1/(gamma2-1)); % Total density (
   isentropic relation)[kg/m^3]
ht2 = h2 + u2^2/2; % Total enthalpy [J/kg]

F_proj_base = P2*(A2-A1); % Force on the projectile from this cell - in
   positive z direction (Eq 2)[N]

end
```

A.4 Baffle Wall Model (baffle_wall_v2.m)

```
function [P2,T2,rho2,u2,h2,R2,M2,s2,cp2,cv2,gamma2,a2,u_lab2,M_lab2,mdot2,
   Tt2,Pt2,rhot2,ht2,F_wall,complex_tcp] = baffle_wall_v2(R1,T1,rho1,u1,P1,
   A1,A2,h1,gas,Y,u_proj,Awf,Awa,M1,Pwf)
%baffle_wall_v2 Models flow across a baffle wall.
%   Solves for the cumulative effect of flow across a baffle wall.

R2 = R1; % Gas constant (no change in this cell) [J/kg*K]
% Assume T2, then solve system and iterate until convergence
kk = 2; % Initialize index for convergence loop
nn = 1; % Initialize increment modifier
nnn = 1; % Initialize increment modifier
complex_tcp = false; % Initialize flag
T_guess = T1; % Guess as the temperature at the previous cell [K]
CoE_residual = 10; % Initialize CoE residual [J/kg]
CoE_conv = 1e-6; % Set CoE convergence criteria [J/kg]
CoE_LHS = 1; % Initialize LHS
% Iterate until CoE converges
while abs(CoE_residual(kk-1)/CoE_LHS)>CoE_conv
    if kk == 2 % If the first iteration
        T_guess(kk) = T_guess(kk-1); % Temperature [K]
        T_up(kk) = false; % Indicates if temp is raised for this iteration

    elseif CoE_residual(kk-1) > 0 % Lower T_guess to reduce residual
        T_up(kk) = false; % Indicates if temp is raised for this iteration
        if T_up(kk-1) % If last temp change was an increase (decrease by a
           smaller increment)
            T_mod(kk) = (1-0.0001*1/nn); % Modifier for T_guess [-]
            T_guess(kk) = T_guess(kk-1)*T_mod(kk); % Temperature [K]
            if nn > 200 % If iterations get high, decrease the step change
               size to speed up convergence
                nn = nn + 20;
            elseif nn > 100
                nn = nn + 10;
            else % Increment normally
                nn = nn + 3; % Increment the increment modifier to produce a
                    smaller step next time
            end
            nnn = 1; % Reset nnn to 1
```

```
    else % If last temp change was a decrease (continue at same change
        size until sign change in residual)
        if nnn > 5 % If the last some# iterations did not change step
            size
            T_mod(kk) = (1-0.0001*1/nn*nnn/3); % Increase the step size
                (temporarily)
        else
            % Normal T_mod
            T_mod(kk) = (1-0.0001*1/nn); % Modifier for T_guess [-]
        end
        T_guess(kk) = T_guess(kk-1)*T_mod(kk); % Temperature [K]
        % Do not increment nn (keep same step size)
        nnn = nnn + 1; % Increment nnn (to track sequential steps at
            same step size
    end

elseif CoE_residual(kk-1) < 0 % Higher T_guess to increase residual
    T_up(kk) = true; % Indicates if temp is raised for this iteration
    if T_up(kk-1) % If last temp change was an increase (continue at
        same change size until sign change in residual)
        if nnn > 5 % If the last some# iterations did not change step
            size
            T_mod(kk) = (1+0.0001*1/nn*nnn/3); % Increase the step size
                (temporarily)
        else
            % Normal T_mod
            T_mod(kk) = (1+0.0001*1/nn); % Modifier for T_guess [-]
        end
        T_guess(kk) = T_guess(kk-1)*T_mod(kk); % Temperature [K]
        % Do not increment nn (keep same step size)
        nnn = nnn + 1; % Increment nnn (to track sequential steps at
            same step size
    else % If last temp change was a decrease (increase by a smaller
        increment)
        T_mod(kk) = (1+0.0001*1/nn); % Modifier for T_guess [-]
        T_guess(kk) = T_guess(kk-1)*T_mod(kk); % Temperature [K]
        if nn > 200 % If iterations get high, decrease the step change
            size to speed up convergence
            nn = nn + 20;
        elseif nn > 100
            nn = nn + 10;
        else % Increment normally
```

```
            nn = nn + 3; % Increment the increment modifier to produce a
                smaller step next time
        end
        nnn = 1; % Reset nnn to 1
    end

end
T2 = T_guess(end); % Set T to the final guess
quad_A = 1; % Coefficient A in quadratic equation
quad_B = -(rho1*u1^2*A1+P1*A1-Pwf*Awf)/(rho1*u1*A1); % Coefficient B in
   quadratic equation
quad_C = (1-Awa/A2)*R2*T2; % Coefficient C in quadratic equation
quad_soln = roots([quad_A quad_B quad_C]); % Solve quadratic equation
   for u2 (eq 8) [m/s]

if isempty(quad_soln) % If no solution to quad eq
    error('No solution to quadratic equation')
end

% Use conditional choice based on current Mach
if M1 >= 1 % If supersonic flow (should remain supersonic - use higher
   velocity solution)
    u2 = max(quad_soln); % Set u to the higer value of the solution [m/s
       ]
    if ~isreal(u2) || u2 < 0 % If the solution is complex or negative,
       it is not valid
        u2 = min(quad_soln); % Try other solution for u [m/s]
        if ~isreal(u2) || u2 < 0 % If both solutions are complex or
           negative
            error('No real/positive solution to quad equation for u2')
        end
    end
else % If subsonic flow (should remain subsonic - or choke)
    u2 = min(quad_soln); % Set u to the lower value of the solution [m/s
       ]
    if ~isreal(u2) || u2 < 0 % If the solution is complex or negative,
       it is not valid
        u2 = max(quad_soln); % Try other solution for u [m/s]
        if ~isreal(u2) || u2 < 0 % If both solutions are complex or
           negative
            % This typically occurs when the shock is placed further
            % back than the true shock location, resulting in a
            % stronger than possible shock, leading to this error.
```

```
                % Will output prior iteration solution with an error
                % indicator to mark end the current shock location
                % simulation with a tcp reached flag.
                T2 = T_guess(end-1); % Set to last temp [K]
                if isequal(kk,2) % If first iteration
                    % Set end state variables to avoid errors
                    P2 = P1;
                    rho2 = rho1;
                    set(gas,'Temperature',T2,'Pressure',P2,'MassFractions',Y
                        );
                    h2 = enthalpy_mass(gas);
                end
                u2 = rho1*u1*A1*R2*T2/(P2*A2); % Set to last u2 (using eq 7)
                    [m/s]
                complex_tcp = true; % Set flag to true (for indicating this
                    error in outside code)
                break % Leave the while loop
            end
        end
    end

    P2 = rho1*u1*A1*R2*T2/(u2*A2); % Pressure (eq 7) [Pa]
    rho2 = P2/(R2*T2); % Density (eq 6) [kg/m^3]

    set(gas,'Temperature',T2,'Pressure',P2,'MassFractions',Y); % Set gas
        state
    h2 = enthalpy_mass(gas); % Enthalpy of gas [J/kg]

    CoE_LHS = h1 + u1^2/2; % LHS of CoE (eq 5) [J/kg]
    if M1 >= 1 % Pre-shock
        CoE_RHS = h2 + u2^2/2 - (abs(P2*Awa-Pwf*Awf)/(rho1*u1*A1))*(u_proj-
            u2); % RHS of CoE (eq 5) [J/kg]
    else % if post shock
        CoE_RHS = h2 + u2^2/2 - (abs(P2*Awa-Pwf*Awf)/(rho1*u1*A1))*(u_proj-
            u2); % RHS of CoE (eq 5) [J/kg]
    end
    CoE_residual(kk) = CoE_RHS-CoE_LHS; % Residual of the CoE equation (eq
        5) [J/kg]
    kk = kk + 1;
end

if u2 < 0 % If u is negative
    error('Negative u') % Display error if u is found to be negative
```

```
end

% Gas state is already set from h calc in the convergence loop
s2 = entropy_mass(gas); % Entropy [J/kg*K]
cp2 = cp_mass(gas); % Specific heat at constant pressure [J/kg*K]
cv2 = cv_mass(gas); % Specific heat at constant volume [J/kg*K]
gamma2 = cp2/cv2; % Specific heat ratio [-]
a2 = soundspeed(gas); % Sound speed [m/s]

M2 = u2/a2; % Mach [-]
u_lab2 = u_proj - u2; % Relative velocity of the fluid w.r.t. the projectile
    /wall [m/s] (fluid velocity in lab frame)
M_lab2 = abs(u_lab2/a2); % Mach # of fluid w.r.t. the projectile/wall [-] (
    fluid mach in lab frame)
mdot2 = rho2*u2*A2; % Mass flow rate (Eq 1)[kg/s]
Tt2 = T2*(1+(gamma2-1)/2*M2^2); % Total temperature [K]
Pt2 = P2*(1+(gamma2-1)/2*M2^2)^(gamma2/(gamma2-1)); % Total pressure in cell
     (isentropic relation)[Pa]
rhot2 = rho2*(1+(gamma2-1)/2*M2^2)^(1/(gamma2-1)); % Total density (
    isentropic relation)[kg/m^3]
ht2 = h2 + u2^2/2; % Total enthalpy [J/kg]

F_wall = P2*Awa-Pwf*Awf; % Net force on the baffle wall (forward and aftward
     faces) (in positive z direction) (eq 2) [N]

end
```

A.5 Ram PFR Convergence Code (ram_solver_v3.m)

```
function [P,T,Y,a,u,M,A1,A2,V,Pt,Tt,rho,rhot,h,ht,Z_tube,AoverAstar,mdot,
    u_lab,M_lab,F_proj,F_wall,F_i,W_dot_i,s,cp,cv,combustion,q,R,gamma,tr,
    dz_tcp,t_avg,p_cell_type,n_tcp,F_tot_baffles,F_tot_proj,I,q_tot,Q,
    F_proj_cum,I_theory,Q_theory,shock_at_baffle_wall_edge] = ram_solver_v3(
    p_cells,p_loc,bore_ID,tube_config,tube_names,tube_length,a_in,num_p_cells
    ,u_in,nsp,R_fill,gamma_fill,mass_fracs_fill,mol_fracs_fill,P_fill,T_fill,
    ss_fill,cp_fill,gas,Ab,n_CH4,n_O2,n_N2,n_C3H8,n_H2,n_N2O,ich4,io2,in2,
    ic3h8,ih2,in2o,beta_th_cmp,CI,n_comb_divs,Proj,WBL)
%ram_solver_v3 Uses the ramFFsolver to solve a TCRA configuration by
%converging upon the proper shock location.
%   Employs a convergence algorithm to determine the proper shock location
%   for a TCRA configuration using the ramFFsolver to provide solutions. v3
%   uses a new convergence algorithm for the BTRA.

% Determine cells that could contain the shock
shock_cell_min = find(p_cells(2,:) == 3,1,'first'); % First tailcone cell
shock_cell_max = find(p_cells(2,:) == 3,1,'last'); % Last tailcone cell
shock_options = p_cells(1,shock_cell_min:shock_cell_max); % List of cell
    numbers that could contain the shock
% Remove cells under baffle walls from shock_options (shock cannot occur
    under baffle wall)
for k = 1:length(shock_options)
    z_tube = (p_cells(3,shock_options(k))+p_cells(4,shock_options(k)))/2 +
        p_loc; % Cell-mid coordinates in tube frame [m]
    [~,section] = Dz_tube(z_tube,tube_config,tube_names,tube_length); %
        Identify section type: 'baffle_chamber', 'baffle_wall', and 'rail'
    if strcmp(section,'baffle_wall') % When cell is under baffle wall
        shock_options(k) = -shock_options(k); % Set to negative for removal
            later
    end
end
shock_options(shock_options < 0) = []; % Remove negative values (eliminates
    cells under a baffle wall)

% Initialize variables
k = 1;
kk = 1;
ap(k) = a_in*9.81; % Projectile acceleration [m/s^2]
```

```
output_flag = []; % Initialize output flag (-1 = comb complete, 1 = tcp
    reached, 0 = domain to short)
shock_guess_range(kk) = length(shock_options); % Number of cells in shock
    guessing range
shock_cell_num_guess(kk) = shock_options(end); % Initial guess for shock
    cell num (last tailcone cell - not under a baffle wall)
shock_bounded = false; % Initialze shock bounded check
bound_guesses = [length(shock_options) floor(0.75*length(shock_options))
    floor(0.50*length(shock_options)) floor(0.25*length(shock_options)) 1]; %
     Shock option index locations for shock bounding guesses
shock_found = false; % Initialize convergence check
fprintf('Solving iteration %d, cell range = %d\n', kk, shock_guess_range(kk)
    )
while shock_found == false
    [comb_complete,temp_P(kk,:),temp_T(kk,:),temp_Y(1+nsp*(kk-1):nsp+nsp*(kk
        -1),:),temp_a(kk,:),temp_u(kk,:),temp_M(kk,:),temp_A1(kk,:),temp_A2(
        kk,:),temp_V(kk,:),temp_Pt(kk,:),temp_Tt(kk,:),temp_rho(kk,:),
        temp_rhot(kk,:),temp_h(kk,:),temp_ht(kk,:),temp_Z_tube(kk,:),
        temp_AoverAstar(kk,:),temp_mdot(kk,:),temp_u_lab(kk,:),temp_M_lab(kk
        ,:),temp_F_proj(kk,:),temp_F_wall(kk,:),temp_F_i(kk,:),temp_W_dot_i(
        kk,:),temp_s(kk,:),temp_cp(kk,:),temp_cv(kk,:),temp_combustion(kk,:),
        temp_q(kk,:),temp_R(kk,:),temp_gamma(kk,:),temp_tr(kk,:),temp_dz_tcp(
        kk,:),temp_t_avg(kk,:),temp_p_cell_type(kk,:),temp_n_tcp(kk,:),
        temp_F_tot_baffles(kk,:),temp_F_tot_proj(kk,:),temp_I(kk,:),
        temp_q_tot(kk,:),temp_Q(kk,:),temp_F_proj_cum(kk,:),temp_I_theory(kk)
        ,temp_Q_theory(kk),temp_shock_at_baffle_wall_edge(kk)] =
        ramFFsolver_v7(p_cells((1+8*(k-1)):(8+8*(k-1)),:),num_p_cells(k),
        p_loc(k),u_in,ap,shock_cell_num_guess(kk),nsp,R_fill,gamma_fill,
        mass_fracs_fill,mol_fracs_fill,P_fill,T_fill,ss_fill,cp_fill,gas,Ab,
        n_CH4,n_O2,n_N2,n_C3H8,n_H2,n_N2O,ich4,io2,in2,ic3h8,ih2,in2o,
        beta_th_cmp,CI,n_comb_divs,Proj,WBL,tube_config,tube_names,
        tube_length,bore_ID);
    M_comb_peak(kk) = max(temp_M(kk,find(temp_combustion(kk,:),1,'last')-10:
        find(temp_combustion(kk,:),1,'last'))); % Peak Mach number in
        combustion zone [-]
    % Generate output flag
    if temp_n_tcp(kk) < length(p_cells) % If the TCP was found
        output_flag(kk) = 1;
    elseif comb_complete == true % If combustion completed before choking
        output_flag(kk) = -1;
    else % Computational domain was too short to complete combustion or
        choke
        output_flag(kk) = 0;
```

```
    error('Domain too short for combustion to complete or choke')
end

% Shock on projectile check
if output_flag(1) ~= 1 % If shock at tailcone end does not cause TCP
    error('Shock is behind the projectile')
end

% Shock bounded check
if output_flag(kk) == -1
    shock_bounded = true; % Shock bounded after first occurance
end

% Restrict shock options by result of previous guess
if output_flag(kk) == 1 % TCP found
    % New upper bound
    shock_options(shock_options-shock_cell_num_guess(kk) > 0) = []; %
       Remove all options behind the prior guess
    shock_guess_range(kk+1) = length(shock_options); % Number of
       possible shock locations
else % If combustion completed before choking
    % New lower bound
    shock_options(shock_options-shock_cell_num_guess(kk) < 0) = []; %
       Remove all options before the prior guess
    shock_guess_range(kk+1) = length(shock_options); % Number of
       possible shock locations
end

% Guess next shock location
if shock_guess_range(kk+1) >= 4 % If 4 or more potential shock locations
    (for kk+1)
    if ~shock_bounded % If shock location hasn't been bounded
        % Procedural guesses until bounded or neck is reached
        shock_cell_num_guess(kk+1) = shock_options(bound_guesses(kk+1));
            % Set next guess
    else % If shock has been bounded
        % Use 'smart' algorithm
        shock_cell_num_guess(kk+1) = shock_options(floor(0.5*
           shock_guess_range(kk+1))); % New shock guess
    end
elseif shock_guess_range(kk+1) == 3 % If exactly 3 options left
    % When there are 3 shock_options left, first and last have been
    % solved (pre- and post-shock, respectively) and only the middle
```

```
        % remains to be solved.
        shock_cell_num_guess(kk+1) = shock_options(2); % Guess middle (2nd)
            option

    else % If exactly 2 options left (pre- and post-shock solutions)
        shock_found = true; % Set flag to true (this will stop the loop)
        if ~shock_bounded % If shock has not been bounded
            warning('Shock on neck or nose (unstart) - solution is
                approximate if unstart is prevented')
        end
    end

    % Iterate and post updates
    kk = kk + 1;
    toc
    if shock_found
        fprintf('Shock found\n')
    else % Post status update
        fprintf('Solving iteration %d, cell range = %d\n', kk,
            shock_guess_range(kk))
    end
end

% The correct solution (first TCP solution) will be at max(shock_options)
% Will save only the correct solution
soln_num = find(shock_cell_num_guess == max(shock_options),1); % Iteration
    number of the correct solution
P = temp_P(soln_num,:);
T = temp_T(soln_num,:);
Y = temp_Y(1+nsp*(soln_num-1):nsp+nsp*(soln_num-1),:);
a = temp_a(soln_num,:);
u = temp_u(soln_num,:);
M = temp_M(soln_num,:);
A1 = temp_A1(soln_num,:);
A2 = temp_A2(soln_num,:);
V = temp_V(soln_num,:);
Pt = temp_Pt(soln_num,:);
Tt = temp_Tt(soln_num,:);
rho = temp_rho(soln_num,:);
rhot = temp_rhot(soln_num,:);
h = temp_h(soln_num,:);
ht = temp_ht(soln_num,:);
Z_tube = temp_Z_tube(soln_num,:);
```

```
AoverAstar = temp_AoverAstar(soln_num,:);
mdot = temp_mdot(soln_num,:);
u_lab = temp_u_lab(soln_num,:);
M_lab = temp_M_lab(soln_num,:);
F_proj = temp_F_proj(soln_num,:);
F_wall = temp_F_wall(soln_num,:);
F_i = temp_F_i(soln_num,:);
W_dot_i = temp_W_dot_i(soln_num,:);
s = temp_s(soln_num,:);
cp = temp_cp(soln_num,:);
cv = temp_cv(soln_num,:);
combustion = temp_combustion(soln_num,:);
q = temp_q(soln_num,:);
R = temp_R(soln_num,:);
gamma = temp_gamma(soln_num,:);
tr = temp_tr(soln_num,:);
dz_tcp = temp_dz_tcp(soln_num,:);
t_avg = temp_t_avg(soln_num,:);
p_cell_type = temp_p_cell_type(soln_num,:);
n_tcp = temp_n_tcp(soln_num,:);
F_tot_baffles = temp_F_tot_baffles(soln_num,:);
F_tot_proj = temp_F_tot_proj(soln_num,:);
I = temp_I(soln_num,:);
q_tot = temp_q_tot(soln_num,:);
Q = temp_Q(soln_num,:);
F_proj_cum = temp_F_proj_cum(soln_num,:);
I_theory = temp_I_theory(soln_num);
Q_theory = temp_Q_theory(soln_num);
shock_at_baffle_wall_edge = temp_shock_at_baffle_wall_edge(soln_num);

end
```